



**MINISTÉRIO DA EDUCAÇÃO**

**Universidade Federal de Alfenas - UNIFAL-MG**  
**Pró-reitora de Pesquisa e Pós-graduação**

Programa de Pós-Graduação em Química



RENATO OLIVEIRA EVANGELISTA

**ALKALINE TANTALUM GERMANATE GLASSES AND  
GLASS-CERAMICS FOR SECOND HARMONIC  
GENERATION**

Poços de Caldas/MG

2021

RENATO OLIVEIRA EVANGELISTA

ALKALINE TANTALUM GERMANATE GLASSES AND  
GLASS-CERAMICS FOR SECOND HARMONIC  
GENERATION

Master thesis presented to the Graduate Program in Chemistry (UNIFAL-MG) as part of the requirements for the Master's degree in Chemistry. Field area: Inorganic Chemistry.

Adviser: Prof. Dr. Gaël Yves Poirier

Poços de Caldas/MG

2021

Dados Internacionais de Catalogação-na-Publicação (CIP)  
Sistema de Bibliotecas da Universidade Federal de Alfenas  
Biblioteca Central – Campus Sede

E92a Evangelista, Renato Oliveira  
Alkaline tantalum germanate glasses and Glass-ceramics for second  
Harmonic Generation / Renato Oliveira Evangelista– Alfenas, MG, 2021.  
109 f.: il. –

Orientador: Gaël Yves Poirier.  
Dissertação (Mestrado em Química) – Universidade Federal de  
Alfenas, 2021.  
Bibliografia.

1. Vidro germanato. 2. Vitrocerâmicas. 3. Óxido de tântalo. 4. Óxidos  
alcalinos. 5. Geração de segundo harmônico. I. Poirier, Gaël Yves.  
II. Título.

CDD- 546

RENATO OLIVEIRA EVANGELISTA

ALKALINE TANTALUM GERMANATE GLASSES AND GLASS-CERAMICS FOR SECOND HARMONIC GENERATION

A Banca examinadora abaixo-assinada aprova a Dissertação apresentada como parte dos requisitos para a obtenção do título de Mestre em Química pela Universidade Federal de Alfenas. Área de concentração: Química Inorgânica.

Aprovado em: 25 de fevereiro de 2021

Prof. Dr. Gael Yves Poirier  
Instituição: Universidade Federal de Alfenas

Prof. Dr. Younes Messaddeq  
Instituição: Université de Laval - Canadá

Prof. Dr. Cleber Renato Mendonça  
Instituição: Universidade de São Paulo



Documento assinado eletronicamente por **Cleber Renato Mendonça, Usuário Externo**, em 25/02/2021, às 16:54, conforme horário oficial de Brasília, com fundamento no art. 6º, § 1º, do [Decreto nº 8.539, de 8 de outubro de 2015](#).



Documento assinado eletronicamente por **Younes Messaddeq, Usuário Externo**, em 25/02/2021, às 16:54, conforme horário oficial de Brasília, com fundamento no art. 6º, § 1º, do [Decreto nº 8.539, de 8 de outubro de 2015](#).



Documento assinado eletronicamente por **Gael Yves Poirier, Professor do Magistério Superior**, em 26/02/2021, às 08:46, conforme horário oficial de Brasília, com fundamento no art. 6º, § 1º, do [Decreto nº 8.539, de 8 de outubro de 2015](#).



A autenticidade deste documento pode ser conferida no site [https://sei.unifal-mg.edu.br/sei/controlador\\_externo.php?acao=documento\\_conferir&id\\_orgao\\_acesso\\_externo=0](https://sei.unifal-mg.edu.br/sei/controlador_externo.php?acao=documento_conferir&id_orgao_acesso_externo=0), informando o código verificador **0470710** e o código CRC **E2E6BB79**.

I devote this work to my family and friends who supported me on this journey, collaborating in the most diverse ways.

## **ACKNOWLEDGMENT**

To my advisor Prof. Dr. Gael Y. Poirier, who provided this incredible experience and for all the support during this journey. I also thank him for all the opportunities offered, teaching, conversations and good company.

To the professors and researchers from other institutions who received me very well, instructing me and enabling this work to be done. In this way, I especially thank Thierry Cardinal, Marc Dussauze, Vincent Rodriguez, Frederic Adamietz and Marcelo Nalin.

To friends and co-workers Lia, Cristiano, Julia, Georges, Florian, Alice, Lara, Dominique and Theo for all help and good moments.

Capes, for the scholarship granted. This work was carried out with the support of the Coordenação de Aperfeiçoamento de Pessoal de Nível Superior – Brazil (CAPES) – Financing Code 001.

Unifal-MG for providing this master's degree.

To the CNRS and LAPHIA programs for the financial support during my research internship in Bordeaux.

To the ICMCB and ISM institutes for receiving and instructing me with excellence, understanding and partnership.

Finally, I am especially grateful for the support of my family and friends, who were essential in this journey, and mainly to God who provided all this.

## RESUMO

Vidros alcalinos de germanato de tântalo de aspecto transparente e homogêneo e de composição molar  $(90-x) \text{GeO}_2\text{-}10\text{M}_2\text{O-xTa}_2\text{O}_5$  com  $x = 15$  e  $20$  e  $\text{M} = \text{Na}, \text{K}$  ou  $\text{Rb}$  foram preparados pela técnica de fusão-quenching. A cor final das amostras foi relacionada com contaminações do cadinho, mas o uso de cadinho de platina puro permitiu a preparação de vidros incolores. O comportamento de cristalização desses vidros foi investigado em detalhes nos vidros de tântalo germanato de sódio e um comportamento de cristalização de múltiplas etapas complexo foi identificado: tratamentos térmicos rápidos (1 h) no início da cristalização induzem precipitação de uma fase cristalina semelhante a bronze de perovskita  $\text{Na}_2\text{Ta}_8\text{O}_{21}$  de um mecanismo de cristalização de volume. Por outro lado, tratamentos térmicos mais longos (pelo menos 18h) na mesma temperatura promovem a formação e o crescimento progressivos de esferulitos superficiais de cerca de 50  $\mu\text{m}$  de diâmetro. Além disso, essas vitrocerâmicas esferulíticas exibem uma forte segunda geração de harmônicos (SHG). As análises elementares apontaram um conteúdo comparativo de tântalo mais alto e baixo de germânio dentro desses esferulitos, enquanto microscopias Raman e SHG correlacionadas foram úteis para determinar que os esferulitos são a fonte dos sinais de SHG e contêm  $\alpha\text{-GeO}_2$  do tipo quartzo. Investigações macroscópicas de SHG também sugerem uma forte dependência da polarização incidente na intensidade de SHG, relacionada com a estrutura cristalina de  $\alpha\text{-GeO}_2$  e orientação de cristalito dentro dos esferulitos.

Palavras-chave: vidro germanato. vitrocerâmicas. óxido de tântalo. óxidos alcalinos.  
geração de segundo harmônico.

## ABSTRACT

Transparent and homogeneous alkaline tantalum germanate glasses of molar composition  $(90-x)\text{GeO}_2-10\text{M}_2\text{O}-x\text{Ta}_2\text{O}_5$  with  $x=15$  and  $20$  and  $\text{M}=\text{Na}, \text{K}$  or  $\text{Rb}$  were prepared by the melt-quenching technique. Final color of the samples were related with contaminations from the crucible but the use of pure platinum crucible allowed to prepare colorless glasses. The crystallization behavior of these glasses was investigated in details in the sodium tantalum germanates glasses and a complex multi-step crystallization behavior was identified: fast heat treatments (1h) at the onset of crystallization induce precipitation of a perovskite bronze-like crystalline phase  $\text{Na}_2\text{Ta}_8\text{O}_{21}$  from a volume crystallization mechanism. On the other hand, longer heat treatments (at least 18h) at the same temperature promote a progressive formation and growth of surface spherulites of about  $50 \mu\text{m}$  in diameter. In addition, these spherulitic glass ceramics exhibit a strong Second Harmonic Generation (SHG). Elemental analyzes pointed out a comparative higher tantalum and lower germanium content inside these spherulites whereas correlated Raman and SHG microscopies were helpful to determine that the spherulites are the source of the SHG signals and contain quartz-like  $\alpha\text{-GeO}_2$ . Macroscopic SHG investigations also suggest a strong dependency of the incident polarization on the SHG intensity, related with the crystal structure of  $\alpha\text{-GeO}_2$  and crystallite orientation inside the spherulites.

Keywords: germanate glass. glass ceramics. tantalum oxide. alkaline oxides.  
second harmonic generation.



## ABBREVIATIONS

<b>AES</b>	- Auger electron spectroscopy
<b>EDS</b>	- Energy-dispersive X-ray spectroscopy
<b>G</b>	- Glass
<b>GC</b>	- Glass ceramic
<b>GM</b>	- Alkaline tantalum germanate glass
<b>H</b>	- Hour
<b>HH</b>	- Horizontal-Horizontal
<b>HV</b>	- Horizontal-Vertical
<b>IR</b>	- Infra red
<b>M</b>	- Metal alkaline
<b>NLO</b>	- Nonlinear Optics
<b>SHG</b>	- Second harmonic generation
<b>T</b>	- Temperature in °C
<b>t</b>	- Time in hours
<b>TTT</b>	- Time-temperature-transformation
<b>UV</b>	- Ultraviolet
<b>VH</b>	- Vertical-Horizontal
<b>VV</b>	- Vertical-Vertical
<b>XRD</b>	- X-ray diffraction

## FIGURES

Figure 1	– Structural differences between crystal and glass.....	20
Figure 2	– Volume change during cooling of a liquid.....	22
Figure 3	Basic germanate structural units .....	24
Figure 4	– Schematic of time-temperature-transformation (TTT) diagram for one thermal history (arrow) .....	26
Figure 5	– Nucleation sketch where in a) shows the rates of nucleation and crystal growth as a function of temperature. The width and temperature range of the curves are different for each individual composition. In b) Two-step heat treatment is used for development of a GC. During the first hold at the nucleation temperature.....	28
Figure 6	– Two incident photons ( $\omega_i$ ) generating another photon of different frequency ( $2\omega_i$ ) .....	34
Figure 7	– SHG without phase matching .....	35
Figure 8	– Glass synthesis sketch .....	38
Figure 9	– Glass ceramic synthesis sketch .....	39
Figure 10	– (a) Experimental setup sketch for linear and non-linear optic measurements for both acquisitions in transmission or reflection while (b) detailed way in transmission mode. For the $\Theta$ -scan the incident angle $\Theta$ is modified at a fixed incident polarization, while for $\psi$ -scans the incident polarization is modified by rotating a half-wave plate ( $\psi$ ) with fixed angle of incidence $\Theta$ .....	44
Figure 11	– Images of a) shattered GNa0 glass obtained under 1 h in thermal treatment, b) GNa1 glass after 9 h under thermal treatment not polished and c) optically polished, all of them with molar rate of $75\text{GeO}_2.15\text{TaO}_2.10\text{Na}_2\text{O}$ made in Pt/Au crucible.....	48

Figure 12 – Images of the GNa2 glass under 1 h in thermal treatment a) unpolished and b) optically polished, with molar rate of $70\text{GeO}_2\cdot 20\text{TaO}_2\cdot 10\text{Na}_2\text{O}$ made in Pt/Au crucible .....	48
Figure 13 – Images of optically polished glasses under 1 h under thermal treatment of a) GNa3 $70\text{GeO}_2\cdot 20\text{TaO}_2\cdot 10$ b) GRb $70\text{GeO}_2\cdot 20\text{TaO}_2\cdot 10\text{Rb}_2\text{O}$ and c) GK $70\text{GeO}_2\cdot 20\text{TaO}_2\cdot 10\text{NK}_2\text{O}$ , being those samples performed in pure Pt crucible .....	49
Figure 14 – DSC curves for GNa glasses .....	50
Figure 15 – DSC curves for GNa3, GK and GRb glasses .....	51
Figure 16 – DSC curves for GNa3, GK and GRb glasses .....	53
Figure 17 – Diffractogram of GNa3 glass .....	54
Figure 18 – In a) refractive index in function on wavelength (nm) for the samples GNa3, GRb and GK fit in Cauchy equation and b) their respective density .....	55
Figure 19 – Spectra of GNa1, Gna2 and Gna3 glasses, showing (a) optical window and (b) absorption in the Uv-visible .....	56
Figure 20 – Spectra of GNa3, GRb and GK glasses, showing (a) optical window and (b) absorption in the Uv-visible .....	57
Figure 21 – Band Gap values of the glasses GNa1, GNa2, GNa3, GK and GRb .....	58
Figure 22 – GCNa0-T-24h glass ceramic bulks with 24 h under thermal treatment at 700, 720, 750, 780 e 800 °C, respectively .....	61
Figure 23 – Microscope images amplified in a) 5x and b) 10x of the glass ceramic GCNa1-800-24, which was obtained from thermal treatment of the glass GCNa1 under 800 °C for 24 h showing that spherulites were not seen in this network .....	62
Figure 24 – GNa3 bulk glass changing progressively in to glass ceramics GNa3-780-t in function of time for a thermal treatment at 780 °C .....	63

Figure 25 – Image of (b) the glass ceramic bulk from GC-Na2-800-18 sample and superficial visualization of the spherulites on it, indicated by the white narrows. The microscopic images had magnification of (a) 5x .....	64
Figure 26 – Image of (e) the glass ceramic bulk from GC-Na3-800-72 sample and superficial visualization of the spherulites on it, indicated by the white narrows. The microscopic images had magnification of (a) 5x, (b) 10x, (c) 10x and (d) 20x .....	65
Figure 27 – DSC curves of glass sample of composition $70\text{GeO}_2\text{-}10\text{Na}_2\text{O-}20\text{Ta}_2\text{O}_5$ and corresponding glass-ceramics after heat-treatment at 800 °C for 1 h, 20 h and 48 h .....	67
Figure 28 – X-ray diffraction patterns of the pristine glass, glass-ceramics after heat treatment for 2, 10, 18, 72 and 624 hours, synthesized $\text{Na}_2\text{Ta}_8\text{O}_{21}$ powder and reference JCPDS 28-1137 of $\text{Na}_2\text{Ta}_8\text{O}_{21}$ .....	68
Figure 29 – (a) Curves showing the (a) spherulite average radius size and density and (b) SHG relative intensity as a function of heat treatment time .....	71
Figure 30 – Glass ceramics optical microscope images a) GC-800C-18h, b) GC-800C-72h and c) GC-800C-624h, showing the spherulites growth .....	73
Figure 31 – Spectra of GNa3 glass and GNa3-800-t glass ceramics, showing (a) optical window and (b) absorption in the UV-visible.....	74
Figure 32 – SEM micrographs on backscattering electrons mode of the samples (a) GC-800C-18h and (b) GC-800C-72h, respectively, where a1 and b1 present the chosen points for EDS elemental analyzes showed in Table 7. Finally, a2 and b2 are showing the line path chosen (in red) where EDS analysis was performed and their intensity profiles for Ta, Ge and Na.....	76
Figure 33 – a1) secondary electron image of a random spherulite in the sample GC-800C-18h, analyzed by AES, where a2,3,4) are elemental mappings for Ta, Ge and O, respectively. b1) secondary electron image of a random spherulite in GC-800C-72h, analyzed by AES, where b2,3,4) are elemental mappings for Ta, Ge and O, respectively .....	78

Figure 34 – Micrographics (a1, b1) and respective $\mu$ -Raman mappings (a2, b2) showing spherulites and glass ceramic regions from the samples a) GC-800C-18h and b) GC-800C-72h, both with polarization VV and taking the Raman peak at $440\text{ cm}^{-1}$ .....	81
Figure 35 – Raman spectra of crystalline references $\text{Na}_2\text{Ta}_8\text{O}_{21}$ , $\alpha\text{-GeO}_2$ , pristine glass and representative Raman spectra collected inside and outside of the spherulites for samples GC-800C-18h and GC-800C-72h (FIGURE 34)....	84
Figure 36 – SHG macro analyses for linear ( $\Theta$ -scan) and nonlinear ( $\psi$ -scan) polarization for the samples (a) GC-800C-18h and (b) GC-800C-72h .....	90
Figure 37 – SHG macro analyses for linear ( $\Theta$ -scan) and nonlinear ( $\psi$ -scan) polarization for the samples GC-800C-18h to 614h .....	91
Figure 38 – Diffractograms for the pastilles PNa, PK, PRb showing the phases $\text{Na}_2\text{Ta}_8\text{O}_{21}$ , $\text{K}_2\text{Ta}_8\text{O}_{21}$ and $\text{Rb}_2\text{Ta}_8\text{O}_{21}$ , respectively .....	92
Figure 39 – Micrograph images from macro crystalline structures in different shapes a) spherulite and b) quadratics for the GCRb-800T-72h glass ceramic .....	93
Figure 40 – Micro-SHG mapping for GCRb800C-72h .....	94
Figure 41 – GCRb-800C-72h SHG signals from $\Theta$ -scan .....	95
Figure 42 – GCRb-800C-72h SHG signals from $\psi$ -scan .....	95

## TABLES

Table 1	–	Examples glass forming materials by quenching method and their classification.....	18
Table 2	–	Basic electro-optical and non-linear effects observed in dielectrics.....	32
Table 3	–	Examples of materials presenting SHG nonlinear susceptibilities.....	33
Table 4	–	Glass sample labels .....	39
Table 5	–	Glass ceramic sample labels .....	40
Table 6	–	GNa3 and glass ceramics GNa3-T-t samples, comparing heat treatments parameters, growing of spherulites and SHG signals .....	71
Table 7	–	EDS quantitative results inside (001) and outside (002) of the spherulite in samples GC-800C-18h and GC-800C-72h. The oxygen concentrations were calculated using the oxide forms Na <sub>2</sub> O, GeO <sub>2</sub> and Ta <sub>2</sub> O <sub>5</sub> .....	76
Table 8	–	SHG and Raman mapping of the spherulite from the sample GC-800C-18h in Figure 34. It shows different incident linear polarization ( $\delta$ ) Vertical-Vertical (VV) and Vertical-Horizontal (VH) and sample counterclockwise rotation (R) of 0° (no rotation) or 90° for the same spherulite area .....	82
Table 9	–	$\mu$ -SHG and $\mu$ -Raman mappings of a spherulite in sample GC-800C-72h under VV linear polarization ( $\delta$ ) .....	83
Table10	–	Attribution of the experimental Raman signals of $\alpha$ -GeO <sub>2</sub> .....	85

## SUMMARY

<b>INTRODUCTION AND MOTIVATIONS</b> .....	14
<b>CHAPTER 1 - LITERATURE REVIEW</b> .....	16
1.1. GLASSES.....	17
1.1.1 Glass definition and main features.....	17
1.1.2 Glass history and production process.....	21
1.2 GERMANATE GLASSES.....	23
1.3 GLASS CERAMICS.....	25
1.4 SECOND HARMONIC GENERATION.....	29
<b>CHAPTER 2 - METHODOLOGY</b> .....	37
2.1 SYNTHESIS OF ALKALINE TANTALUM GERMANATE GLASSES....	38
2.2 SYNTHESIS OF ALKALINE TANTALUM GERMANATE GLASS CERAMICS.....	39
2.3 CHARACTERIZATIONS.....	41
2.3.1 X-ray diffraction.....	41
2.3.2 Thermal analysis.....	42
2.3.3 UV-Vis absorption spectroscopy.....	42
2.3.4 Infrared spectroscopy.....	42
2.3.5 Ellipsometry measurements.....	42
2.3.6 Density measurements.....	43
2.3.7 Energy dispersive X-ray spectroscopy.....	43
2.3.8 Auger electron spectroscopy.....	43
2.3.9 Micro Raman and SHG measurements.....	43
2.3.10 Macro-SHG measurements.....	44
<b>CHAPTER 3 - ALKALINE TANTALUM GERMANATE GLASSES</b> .....	46
3.1 SYNTHESIS PROCESS AND GENERAL ASPECTS.....	47
3.2 THERMAL ASPECTS.....	49

3.3	STRUCTURAL CHARACTERISTICS.....	52
3.3.1	Glass Raman analysis.....	52
3.3.2	Glass x-ray diffraction analysis.....	54
3.4	GENERAL PHYSICAL AND OPTICAL FEATURES.....	54
3.4.1	Density and refractive index.....	54
3.4.2	UV-Vis-IR spectroscopy.....	56
<b>CHAPTER 4 - ALKALINE TANTALUM GERMANATE GLASS CERAMICS...</b>		<b>60</b>
4.1	SODIUM TANTALUM GERMANATE GLASS CERAMICS.....	61
4.1.1	Chronological sequence of obtaining and growing of spherulites.....	61
4.2	DETAILED INVESTIGATIONS IN THE GLASS CERAMICS GCNA3..	66
4.2.1	Thermal properties.....	66
4.2.2	X-ray diffraction analysis.....	67
4.2.3	General features.....	70
4.2.4	UV-Vis-IR absorption spectroscopy.....	74
4.2.5	Elemental analysis by EDS and AES.....	75
4.2.6	Correlated SHG and Raman microscopies.....	79
4.2.7	Macroscopic SHG measurements.....	89
4.3	POTASSIUM AND RUBIDIUM TANTALUM GERMANATE GLASS CERAMICS.....	92
4.3.1	General features.....	92
4.3.2	Macroscopic SHG response.....	94
<b>CONCLUSION.....</b>		<b>97</b>
<b>REFERENCES.....</b>		<b>98</b>



## INTRODUCTION AND MOTIVATIONS

Glasses in our contemporaneous society is part of our lives and they bring not only common uses like dishes, containers, flasks, component of diverse materials and products, in constructions or in aesthetic and decoration purpose, but go further providing innumerable advanced technological applications. Their crystallization process toward a glass ceramic material broadens even more their importance, biding together specific crystals and amorphous materials characteristics. Furthermore, the promising field of photonics, which has changed the traditional way of communication, is one of these important glass technological applications. Nowadays, it is possible to create an ultrafast system by optical signals processing, while decreasing the need of electric signals only by the unique characteristics that glasses could provide.

In this work we prepared oxide glasses in the ternary systems  $\text{GeO}_2\text{-M}_2\text{O-Ta}_2\text{O}_5$  with  $M = \text{Na, K and Rb}$ , by the traditional melt quenching method, and glass ceramics obtained by heat treatments of those synthesized glasses. We also investigated the crystallization mechanisms and crystalline phases obtained in terms of crystallographic description as well as related elemental analyzes. Finally, the efficiency of these glass-ceramics for Second Harmonic Generation (SHG) was also deeply investigated.

In fact the crystallization kinetics and formation of spherulites could be correlated to SHG signals. Such second-order nonlinear behavior is usually not detected in glasses because of their intrinsic centrosymmetry. However, this optical isotropy could be broken by performing structural changes on the glass material. The control of heat treatments on alkaline tantalum germanate glasses showed that these compositions can lead to the crystallization of a  $\text{Na}_2\text{Ta}_8\text{O}_{21}$  sodium tantalate phase, hardly mentioned in the literature and poorly described in terms of crystalline structure. Furthermore, the formation of surface structures identified as spherulites containing agglomerated crystallites was observed after the first crystallization stage. One could notice that the presence of these spherulites is a condition for the observation of SHG. Therefore, it seems essential to prepare glass-ceramics that contain these crystalline structures and proceed with a more detailed study of the crystallization mechanisms occurring in these glassy compositions and detailed

crystallographic characterization of the NLO-active phases. In fact, SHG does not seem to be related to the formation of crystallites in a first crystallization stage, but to the organization of these crystallites in spherical regions (spherulites) in a second crystallization stage. In this way, understanding and controlling these SHG phenomena in glass-ceramics can lead to the development of active optical devices for integrated optics, development of lasers at unconventional wavelengths as well as uses in telecommunications.

The discovery of these spherical structures occurred during the study of germanate and phosphate glasses containing high contents of niobium and tantalum, and they were extensively investigated by our research group at UNIFAL-MG due to the specific optical and thermal properties arising from the modification of the oxide glass network by the  $\text{NbO}_6$  or  $\text{TaO}_6$  units (GUEDES, 2020; MARCONDES, 2018; MARCONDES, 2019; PIETRO, 2019; CUNHA, 2018; CUNHA and MASESTRI, 2018; LIMA and CASSANGES, 2014). Specifically, it was identified that the incorporation of transition metals Nb or Ta considerably increases the glass formation ability, thermal stability against devitrification as well as chemical stability. In addition, several studies have shown an improvement of luminescent properties when doped with rare earth ions. More recent studies developed by our group have also shown the possibility of using these compositions for structuring 1D and 2D optical properties using the thermal polarization technique.

The first chapter of this work brings a review on main important topics in literature to give a base and better understanding of this thesis. The second chapter is focused on the current methodologies employed during this work. In this thesis, glasses and glass ceramics were analyzed by X-ray diffraction, optical microscopy, UV-Vis-NIR absorption spectroscopy, thermal analysis, density and refractive index measurements, elemental analyzes, macroscopic SHG measurements and correlated Raman and SHG microscopies. Finally, the third and fourth chapters present the characterizations and related discussions the glasses and glass ceramics, respectively.

# CHAPTER 1

---

## **LITERATURE REVIEW:**

Review on main topics in literature to give background and better understanding of this thesis.

## 1.1 GLASSES

### 1.1.1 Glass definition and main features

Present in everyday life in the form of utensils, ornaments, containers, electronic and decorative pieces, in civil construction, in industry, in art, advanced materials and in the development of science and modern society, glass has great structural and economic importance with diversified use due to its multifunctional character. In photonics, glasses are also commonly found in flat and filament shape and main component of fibers, lasers and displays. (ANANTHANARAYANAN, 2017; EVSTROPIEV, 1963; SHELBY, 2005, ALVES, 2001; AKERMAN, 2000; RAJARAMAKRISHNA, 2019; MUSGRAVES, 2019). In addition, they have great modern value due their eco-friendly and recyclable importance.

Even though glass is commonly known and extensively used, its definition is still discussed between authors. Some main parameters such as glass transition temperature, states of matter, amorphous and crystalline state, material structure, density, molecular interactions have been extensively discussed in order to explain what is glass. For many years, as reported and organized by Alves (2001) and Rajaramakrishna, (2019), the most popular definitions of glass defined it as a solid, amorphous with complete absence of long-range order and periodicity, showing a glass transition region. Furthermore, any material, inorganic, organic or metal, forming by any technique, which exhibits a glass transition phenomenon is glass. However, those definitions do not consider that some non-crystalline solids obtained by other methodologies such as sol-gel technique (BOGOMOLOVA, 2006; SAKKA, 2017) and chemical vapor deposition (MURUGASEN, 2015) do not exhibit the glass transition phenomenon.

. A current and well accepted general definition given by Zanotto (2019) says that glass is a nonequilibrium, non-crystalline state of matter that appears solid on a short time scale but continuously relaxes towards the liquid state, leading, eventually, to a crystalline state. Therefore, it combines features of both liquids and solids.

The conventional melt-quenching is the most popular technique for making glasses (JIUSTI, 2020; ALVES, 2001, GLASS AND GLASS-CERAMICS, 2017), however, there are more methods such as sol-gel (BOGOMOLOVA, 2006; SAKKA, 2017; ZANOTTO, 2017; ZANOTTO, 2004) and chemical vapor deposition techniques (MURUGASEN, 2015). Glasses can be synthesized by a variety of different elements

and compounds according to its purpose and because of that they could present different structure interactions such as covalent, ionic, molecular, metallic and hydrogen bonded (ALVES, 2001; RAJARAMAKRISHNA, 2019). An interesting feature is given by the coloring agents that can be added to the glass network in order to give the corresponding color in the visible such as  $\text{Cu}^{2+}$  (blue),  $\text{Cr}^{3+}$  (green),  $\text{Cr}^{6+}$  (yellow),  $\text{Mn}^{3+}$  (violet)  $\text{Mn}^{4+}$  (black),  $\text{Au}^0$  (ruby) and CdS and CdSe (orange) (ALVES, 2001; RAJARAMAKRISHNA, 2019). Because of this synthesis formation variety, they are classified according to their precursor materials for a glassy formation. Oxide glasses are usually classified as silicates, borates, phosphates, germanates or tellurites whereas other non-oxide glasses include chalcogenides, fluorides, halides, acetates metallic and organic glasses (ALVES, 2001, RAJARAMAKRISHNA, 2019). However, the list of forming glasses is extent and some further glass class examples are seen in Table 1.

Table 1 – Examples of glass forming materials by quenching method, organized by their general classification.

<b>(to be continued)</b>	
<b>Glass class types</b>	<b>Examples of glass forming material</b>
Elements	S, Se, P.
Oxides	$\text{B}_2\text{O}_3$ , $\text{SiO}_2$ , $\text{GeO}_2$ , $\text{P}_2\text{O}_5$ , $\text{As}_2\text{O}_3$ , $\text{Sb}_2\text{O}_3$ , $\text{In}_2\text{O}_3$ , $\text{Tl}_2\text{O}_3$ , $\text{Sn}_2\text{O}_3$ , $\text{PbO}_2$ , $\text{SeO}_2$ , $\text{TeO}_2$ , $\text{MoO}_2$ , $\text{WO}_3$ , $\text{Bi}_2\text{O}_3$ , $\text{Al}_2\text{O}_3$ , $\text{V}_2\text{O}_5$ , $\text{SO}_3$ .
Sulfides	$\text{As}_2\text{S}_3$ , $\text{Sb}_2\text{S}_3$ and various sulfides of B, Ga, In, Te, Ge, Sn, N, P, Bi, $\text{CS}_2$ , $\text{Li}_2\text{S}$ - $\text{B}_2\text{S}_3$ , $\text{P}_2\text{S}_5$ - $\text{Li}_2\text{S}$ .
Selenides	Selenides of Tl, Sn, Pb, As, Sb, Bi, Si, P
Tellurides	Tellurides of Tl, Sn, Pb, As, Sb, Bi, Si, P
Halides	$\text{BeF}_3$ , $\text{AlF}_3$ , $\text{ZnCl}_2$ , $\text{Ag}(\text{Cl}, \text{Br}, \text{I})$ , $\text{Pb}(\text{Cl}_2, \text{Br}_2, \text{I}_2)$ and multi-component mixtures.
Nitrates	$\text{KNO}_3$ – $\text{Ca}(\text{NO}_3)_2$ and many other binary mixtures containing alkaline and alkaline earth nitrates
Sulphates	$\text{KHSO}_4$ , $\text{K}_2\text{SO}_4$ - $\text{ZnSO}_4$ - $\text{Na}_2\text{SO}_4$ and other binary and ternary mixtures.

Table 1 – Examples of glass forming materials by quenching method, organized by their general classification.

<b>Glass class types</b>	<b>Examples of glass forming material</b>
Carbonates	$K_2CO_3$ - $MgCO_3$
Acetates	$Na(CH_3COO)$ , $Li(CH_3COO)$
Organic compounds	o-terphenyl, toluene, 3-methylhexane, 2,3-dimethyl ketone, ethylene glycol, methyl alcohol, ethyl alcohol, glycerol, ethyl ether, glucose
Metal alloys	$Au_4Si$ , $Pd_4Si$

Reference: DOREMUS (1973) and ALVES (2001)

Oxide glasses can also be classified according to their functions in the vitreous formation. The network formers such as  $SiO_2$ ,  $B_2O_3$ ,  $P_2O_5$ ,  $GeO_2$ ,  $As_3O_3$ ,  $As_2O_5$ ,  $V_2O_5$  form strongly cross-linked macromolecular chains forming the glass network (ANANTHANARAYANAN, 2017; RONG, 1992; RAJARAMAKRISHNA, 2019). The oxide network modifiers such as  $Na_2O$ ,  $K_2O$ ,  $Rb_2O$ ,  $Li_2O$ ,  $CaO$ ,  $BaO$ ,  $MgO$ ,  $SrO$  induces changes in the glass-forming structure and on some properties such as the thermal expansion coefficient, glass transition temperature, refractive index and density. However, they do not participate in the chain network but rather bring the extra bridging and/or non-bridging oxygen (ANANTHANARAYANAN, 2017; JIUSTI, 2020). Finally, the intermediate oxides such as  $Al_2O_3$ ,  $Ta_2O_5$ ,  $PbO$ ,  $ZnO$ ,  $ZrO_2$ , generally, do not form glass networks by themselves but can participate in glass network formation or act as network modifiers depending upon the conditions in the glass network (ANANTHANARAYANAN, 2017; JIUSTI, 2020).

Considering that glasses are amorphous materials with non-stoichiometric proportions of their base components (AKERMAN, 2000; JUSTINO, 2014; ZANOTO, 2004), they show a more disordered structure which can be seen by the arrangement showed by Zachariasen (1932), especially when compared to crystals that are formed by crystalline lattices. The differences between crystals and glasses are seen in Figure 1.

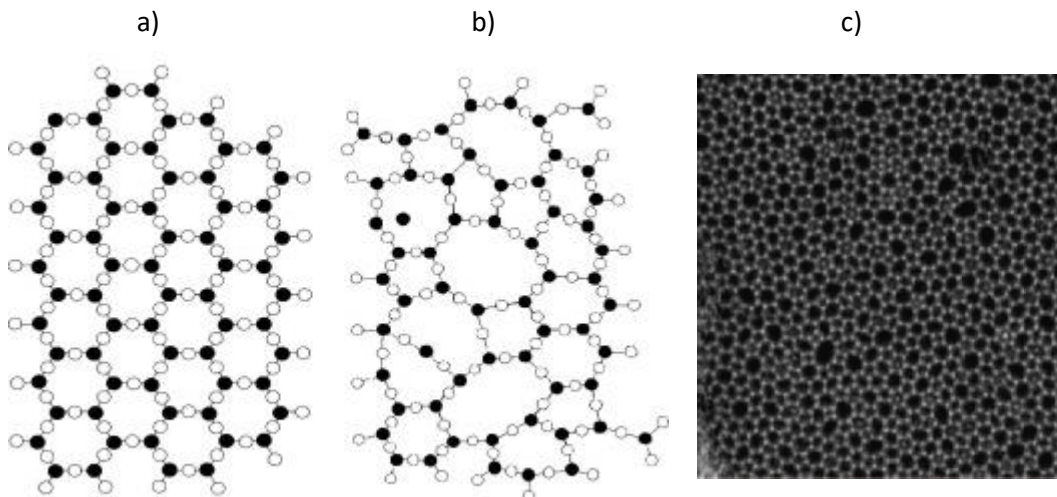


Figure 1 – Structural differences between crystal and glass. In a) a general structural arrangement of a crystal showing the crystal lattice, b) glass general structural arrangement according to Zachariasen and confirmed by the c) high resolution scanning electron microscope (SEM) of glass silica on graphene films.

Reference: Modified from Jiang and Zhang (2014), Huang (2012) and Zachariasen (1932)

One of the striking characteristics of glasses related to their specific glass method formations are their diversified manipulation and structural arrangement, which can be processed in high temperatures (i.e. 1700 °C for silica glass former compounds), acquire a format submitted to the production process, conduct or block light, filter, contain, transmit or resist electromagnetic radiation (AKERMAN, 2000; ARAÚJO, 1997; PANTAZIS, 2010; MUSGRAVES, 2019). Structurally it can contain different elements, be dense or light, porous, impermeable and have mechanical resistance. Furthermore, they can have very low thermal expansion coefficients, allowing to suffer sudden variations in temperature without causing dimensional changes or cracks. Finally, they can be insulators, conductors or electric superconductors or ionic conductors depending on the incorporation of elements in their structure (AKERMAN, 2000; ARAÚJO, 1997; CHOWDARI, 1989; CORNING, 2017; PANTAZIS, 2010; MUSGRAVES, 2019 and ZANOTO, 2004). The synergy between all these specific properties makes glasses unique materials for optical applications as either passive or active media.

The key to understand their multifunctional character and great technological application is to attend to their forming process and network elemental composition. Therefore, it is easy to see that glasses are present in our contemporaneous society not only in ornamentation, art, manufacture of containers or utensils, but extensively found in civil construction, equipment, microscopes, automobiles, aerospace, cell phones, electronics in general, laboratories, hospitals, telecommunications, lasers, display glasses, fibers (ALVES, 2001; AQUINO, 2013; CORBELLA, 2003; CORNING, 2017; MANZANI, 2011; PARAMOND, 2008; SHELBY, 2005; ANANTHANARAYANAN, 2017; EVSTROPIEV, 1963; SHELBY, 2005, ALVES, 2001; AKERMAN, 2000; RAJARAMAKRISHNA, 2019, MUSGRAVES, 2019; VARSHNEYA, 2019, LOIKO, 2017). Specially for fibers, the silica optical fibers are efficient devices for long-distance light transmission with very low attenuation (HAYASHI, 2020). On the other hand, well-designed glass compositions, usually doped with rare earth active ions, are also able to emit specific wavelengths of technological interest and are applied for optical amplification or glass-based laser cavities (HE, 2020, BOETTI, 2017; LUCAS 2015).

### 1.1.2 Glass history and production process

The history of glass and its processing is old, being remote to the 7th century BC with the manipulation of stoves of saltpeter blocks on sand, by the Phoenicians (ALVES, 2001). However, it is known that glasses can be formed naturally by melting rocks, followed by rapid cooling. Its use in the form of opaque and colored glass for adornments, containers and ornaments can be confirmed historically by Syrians, Egyptians and on regions of the Middle East (ZANOTTO and COUTINHO, 2004). However, it was only in the 1st century with the introduction of the blowing technique that its most significant expansion was possible. It became even more popular with the production of transparent glass. However, its basic formula still consisted of the mixture of sand, calcium carbonate and alumina. In the Middle Ages, its use was extended to windows, stained glass and art (ZANOTTO and COUTINHO, 2004). Alchemists looking for greater transparency and shine in glasses and decanters added lead, boron to increase heat resistance and cobalt to generate blue color (MOATTAR, 2010; NEWMAN, 2001; SHEVCHENKO, 2005). In the past decades, silicate glasses doped with germanium allowed to produce 1D optical waveguides,



giving rise to optical fibers. (DEUBENER, 2009; LIN, 2007; PARAMOND, 2008). The increase in resistance from impacts, added to a greater lightness, made the alkali-aluminosilicate glass type become a structural part of cell phones and electronics in general (CORNING, 2017). The various studies, manipulations, increments of elements given by time and, finally, automated production provided a variety of multifunctional and large-scale glasses.

The basic glass production process takes place by fusing starting materials (such as oxides, chalcogenides, halides, metals and organic compounds) and subsequent cooling at rates high enough to avoid crystallization (BRAZ, 2014). The behavior of a liquid under different cooling rates is exemplified through the well-known diagram of volume versus temperature, in Figure 2.

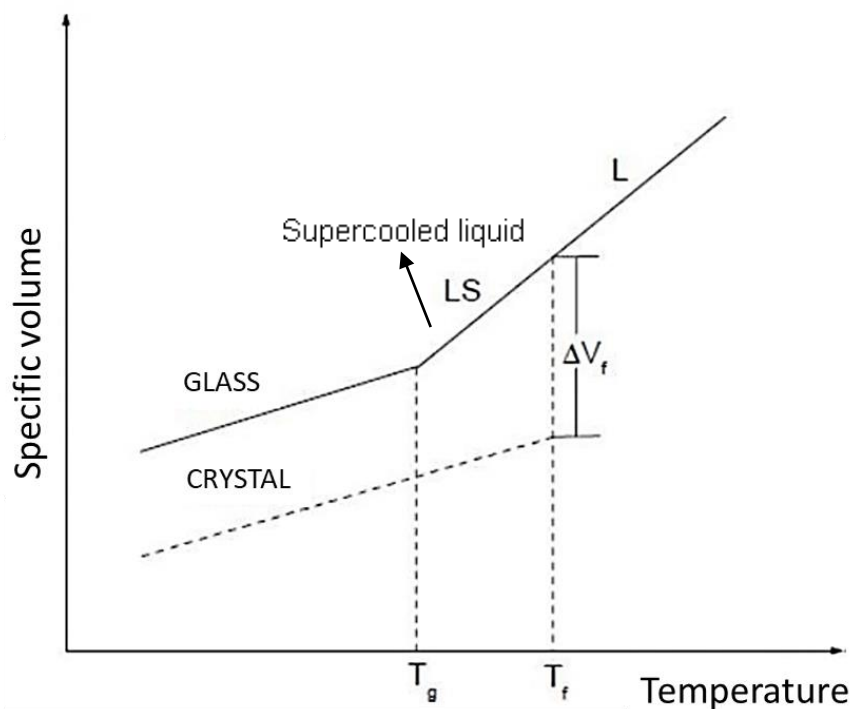


Figure 2 – Volume change during cooling of a liquid.

Reference: Modified from Araújo (1997, p. 327).

Through the way that the cooling of the molten liquid occurs in the metastable equilibrium region, which is the region between the melting temperature ( $T_f$ ) and the glass transition temperature ( $T_g$ ), a glass or a crystalline material can be formed. Having a slower cooling rate there will be enough time for the formation of a crystalline reticule, given by the adequate orientation of the constituent units of the melt, with a significant reduction in volume. However, if the cooling rate is fast enough, these constituent units will not have enough time to organize themselves in order to form crystalline lattices, that is, crystallization does not occur, obtaining a non-crystalline material. In this case, the liquid does not solidify under the melting temperature, maintaining the liquid behavior even at low temperatures. When the liquid follows the glass formation, the specific volume experiments a continuous decrease in a temperature region known as supercooled liquid. However, in a lower temperature range known as glass transition temperature, the slope of temperature variation decreases. Therefore, glasses prepared by the quenching method present this characteristic glass transition interval (ALVES, 2001; JIUSTI, 2020, ZANOTTO, 2017).

## 1. 2 GERMANATE GLASSES

The  $\text{GeO}_2$  glass former became popular due to its structural similarity to silicon oxide compounds (presence of Q4 Ge-O tetrahedral units). According to SHELBY (2005), the germanium-oxygen bond length is around 0.173 nm and with an O-Ge-O connection angle smaller than that observed in O-Si-O. It also presents some interesting properties for glass production such as high thermal stability and lower melting point and viscosity (POLUKHIN and URUSOVSKAYA, 1977; POLUKHIN and BURDINA, 1977; POLUKHIN, 1974).

Addition of modifiers or intermediates such as alkaline or alkaline earth oxides makes the viscosity decrease whereas intermediaries such as transition metals usually increase the glass connectivity and viscosity (SHELBY, 2005). Furthermore, according to Shelby (2005), the addition of the alkaline metals (M) Na, K and Rb with an average of 17 mol% of  $\text{M}_2\text{O}$ , the viscosity decreases in the order  $\text{Na} > \text{K} > \text{Rb}$ .

In addition, some studies support the idea that if the addition of modifiers occurs in the range between 0-15%  $\text{GeO}_6$  octahedrons are formed preferentially, while in the

range above 15% are seen, preferentially, the tetrahedra  $\text{GeO}_4$ . This change, which can be visualized on a density curve for these materials, is known as the “germanate anomaly” (ALDERMAN, 2017; EVSTROPIEV, 1963; MURTHY, 1964).

However, recent studies by KOROLEVA, (2019), report that for a pure germanate ( $\text{GeO}_2$  glass former) glass could present in its network the structure units  $\text{GeO}_4$  ( $Q^n$  - tetrahedra),  $\text{GeO}_5$  (trigonal bipyramids) and/or  $\text{GeO}_6$  (octahedra), as shown in Figure 3. In those units, the central atom is germanium in which is surrounded by oxygens atoms.

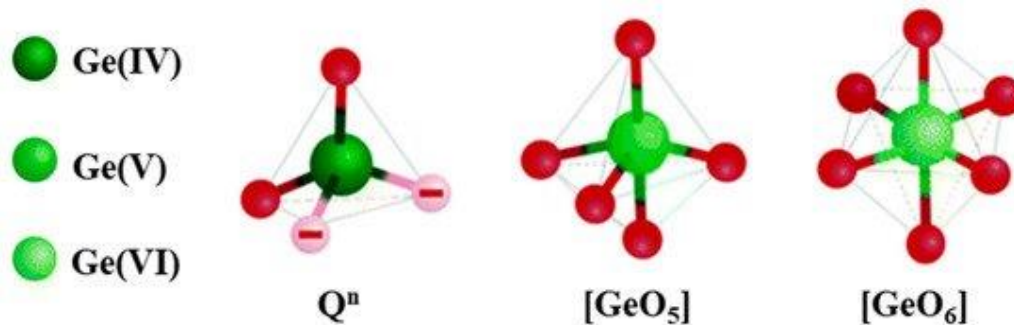


Figure 3 – Basic germanate structural units.

Reference: Modified from Hongisto (2020)

In order to value those studies, also a recent report by ZHANG (2017) shows that the alkaline glass system  $\text{K}_2\text{O}-\text{GeO}_2$  present those 3 basic structures units if the alkaline modifier  $\text{K}_2\text{O}$  is between 11 to 20 mol%. However, if the addition of the modifier is larger than 20 mol%, only  $\text{GeO}_4$  and  $\text{GeO}_6$  are observed. Considering this typical behavior, a glass network with the  $\text{GeO}_2$  could be better understood taking the molar ratio as parameter from the glass former and modifier.

In general, glasses based on germanium oxide (glass former) exhibit broad optical transparency window from 0.35 to 5.5  $\mu\text{m}$ , together with lower processing temperatures when compared with classical silicate glasses (DEUBENER, 2018; HOLLAND, 2012). Optical interests on germanate glasses also include lower phonon energy and dispersion constant as well as higher refractive index (NAGANO, 1991;

MARCONDES, 2017, POLUKHIN and URUSOVSKAYA, 1977; POLUKHIN and BURDINA, 1977).

Finally, the addition of oxides such as  $Ta_2O_5$  control their thermal stability (GUEDES, 2020; CUNHA, 2018; PIETRO, 2015) and since germanate glasses can present high chemical resistance in different environments, simple synthesis and a good optical quality, they could be applied for linear and nonlinear optical (NLO) purposes. In fact, some studies already investigated these materials as rare earth hosts and NLO media (GUEDES, 2020; POIRER, 2019). However, germanate glasses typically exhibit certain content of hydroxyl (OH) groups showed by the absorption band found at around 3-4  $\mu m$  when they are melted in an ambient atmosphere (air). This could lead to a decrease in IR transparency, glass transition temperature and refractive index (LIN, 2011; JIANG, 2009).

### 1.3 GLASS CERAMICS

Glass ceramics are materials formed from a glass precursor, combining unique properties from their glassy and crystalline components. Therefore, they generally exhibit superior chemical durability and mechanical strength comparing to their precursor. They could take different shapes and differently from general ceramics, they allow the possibility of zero or nearly zero porosity for hermetic sealing (ANANTHANARAYANAN, 2008; RAWLINGS, 2006; TUMMALA, 1991), Glass ceramics could be described as crystalline phases contained in a vitreous phase in which undergoes a process of devitrification, commonly called crystallization (STRNAD, 1986). In other words, they can be understood as polycrystalline solids in a residual glassy matrix. The term "glass ceramic" was created in the 1960s (MCMILLAN, 1964) and since then this material have been studied and developed for diverse applications.

Generally, they are made by any glass synthesis method as the first step and then undergoes a crystallization-controlled step (ANANTHANARAYANAN, 2008; TUMMALA, 1991; ZANOTTO, 2017). This is only possible due the thermodynamically metastable state of the glass. On the other hand, glass viscosity makes this process more favorable by heating once at room temperature this would take long periods of time for a structural rearrangement in order to start nucleation process and then the growth of crystals.

However, if we consider that the structure of the glass is similar from its super-cooled liquids, in function of time it will relax spontaneously in a crystallization process (ZANOTTO, 2017). Nevertheless, if such process can theoretically occur at room temperature, it would take extremely long periods of time, since the very high viscosity disturbs the structural rearrangement for the nucleation and growth of the crystals (FOKIN, 2006). Therefore, suitable heat treatment is the key to enable a favorable separation of the crystalline phase (tiny crystals) from the glassy material and then those tiny crystals gather and start the process of growth. All of these steps can be controlled by heat treatment (HOLLAND, 2012, LEWIS, 1989). The temperature and time under heat treatment are defined specifically according to the glass composition, based mainly on the thermal glass transition. If the glass is heated above  $T_g$ , its viscosity decreases allowing such mobility of atoms and ions migration for a possible structural rearrangement with thermodynamic equilibrium (KOMATSU, 2017; ZANOTTO, 2017).

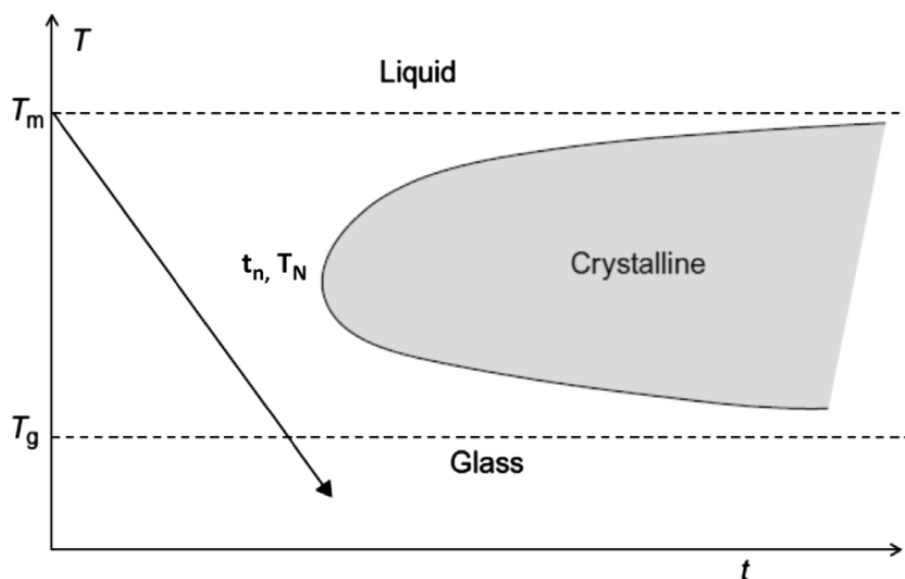


Figure 4 – Schematic of time-temperature-transformation (TTT) diagram for one thermal history (arrow).

Reference: Modified from Rupp (2010)

Crystallization process can be visualized in the Figure 4 by the TTT diagram (time temperature-transformation). Here is shown a temperature set ( $T$ ) in function of time ( $t$ ) required for crystallization. One material is in its liquid form if the temperature is at or above its specific melting temperature ( $T_m$ ). Therefore, only for temperatures under  $T_m$  the time for the crystallization starts to decrease until  $t_n$  and, only then, it could be expected to form a crystalline material. However, as much of this temperature decreases, inversely, the viscosity increases and as consequence the time for crystallization start to increase again for temperatures under  $T_N$ . One can notice that the gray area represents then the region where crystallization could occur in a material. Finally, TTT diagram can be also used to set the critical cooling (lowest cooling rate for glass formation) for a material glass in order to avoid crystallization and it could be expressed by correlating these parameters as:

$$\frac{dT}{dt_c} = \frac{T_m - T_n}{t_n}$$

Glass crystallization is an exothermic event seen on thermal analysis such as differential scanning calorimetry (DSC) differential thermal analysis (DTA). Basically, the crystallization process involves two main steps (KARPUKHINA, 2014; KOTHIYAL, 2012; ANANTHANARAYANAN, 2017; CASASOLA, 2012; THIEME, 2014). The first step is the nucleation where small nuclei of the crystalline phase (often on a nanoscale) or of an initiator phase are formed in the glass and, finally, the growth step where the crystalline phase grows on or from this nucleus. The rates of nucleation and crystal growth are shown in Figure 5.

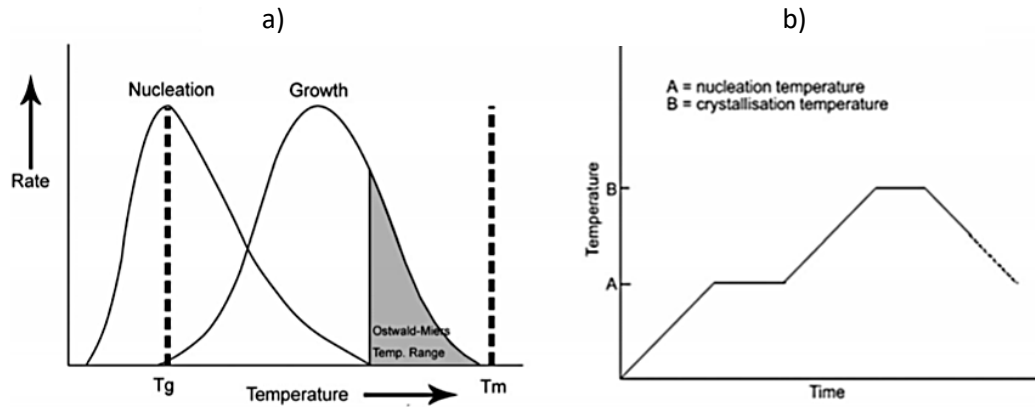


Figure 5 – Nucleation sketch where in a) shows the rates of nucleation and crystal growth as a function of temperature. The width and temperature range of the curves are different for each individual composition. In b) Two-step heat treatment is used for development of a GC. During the first hold at the nucleation temperature.

Reference: Modified from Karpukhina (2014)

A nucleus can be understood as a different phase in an unstable equilibrium with the surrounding glassy phase. In other words, a submicroscopic cluster of the new crystalline phase (ANANTHANARAYANAN, 2017; KARPUKHINA, 2014), Nucleation generally occurs at temperatures at or just above  $T_g$ . On the other hand, crystal growth rate is usually at higher temperatures, shown by Figure 5. However, for high temperatures near the melting glass temperature, known as the metastable supercooling or the Ostwald–Miers range (FIGURE 5), there are no new nuclei formation. Therefore, heat treatments in this region range would not lead to crystallization due to the absence of nucleation (ANANTHANARAYANAN, 2017).

In order to form nuclei, a new surface by atoms aggregation is created and with that energy is necessary that generally comes from the phase transition to crystal. Another important requirement is the overcome of diffusion barriers by these atoms. Only then this particle could grow into a crystallite form. The nucleation rate that is in function of thermodynamic and kinetic barriers could be expressed as:

$$I = I_0 \exp\left(-\frac{W^* + \Delta G_D}{k_B T}\right)$$

where  $I_0$  is the pre-exponential term,  $k_B$  the Boltzmann constant, and  $T$  the absolute temperature. The  $\Delta G_D$  is the activation energy for transfer of a species through the melt/ nucleus interface and is the kinetic contribution to the nucleation rate. The  $W^*$ , which is a thermodynamic barrier for nucleus formation, is the free energy change due to the formation of a new nucleus of critical size  $r^*$ . Below the critical size  $r^*$  the small atomic clusters or embryos are not stable and can dissolve in the original glass without producing a nucleus.

Nucleation is divided in homogeneous and heterogeneous mechanisms. The first one is spontaneous, where the formation of nuclei occur in the absence of any phase inhomogeneity, surface borders or interfacial boundaries. On the other hand, heterogeneous mechanism starts at the interface boundaries and surfaces and is catalyzed by the presence of foreign impurities and nucleating agents (ANANTHANARAYANAN, 2017).

Finally, after the nucleation process starts, crystalline structures are formed and give rise to the crystal growth. Now, atoms diffusion takes place between the interface of the glass and crystalline regions. The growing rate is controlled basically by the temperature and surrounding viscosity, in other words, the equilibrium between thermodynamic and kinetic factors. That is the reason that heat treatment parameters are the key in order to control the crystallization process to create specific glass ceramics according to their features and applications. Precisely because glass ceramics combine the properties of both glasses and crystalline phase, nowadays, there are abroad researches and applications.

#### 1.4 SECOND HARMONIC GENERATION

When studying the phenomena of light propagating in a medium, two main classes are approached: linear optics and non-linear optics. Linear optics refers to a light propagation of low intensity in which waves do not interact with the medium while passing through it or even with themselves, that is, the optical properties of the material are not altered by the incident light (SUTHERLAND, 2003; BOYD, 2008; GUENTHER, 2015) In this class, polarization in the dielectric material is linearly proportional to the applied electric field (BOYD, 2008, SUTHERLAND, 2003). Some of the main generated phenomena are important for characterizing materials such as refraction, reflection, absorption, interference, luminescence, scattering



(SCHNEIDER, 2004; WALKER, 2014; SIMMONS, 2000). However, if the light has a sufficiently high intensity, the waves can interact with the environment where they are propagating and with each other while in the mean, generating phenomena of non-linear optics such as the generation of second harmonic, third harmonic, Kerr effect, among others. For NLO, optical properties of the medium are modified by the presence of light and this interaction occurs in a non-linear way (SUTHERLAND, 2003; SCHNEIDER, 2004).

However, it was only in the 60s, together with the creation of lasers that nonlinear optical phenomena began to be observed since they provided an intense coherent light source (ARMSTRONG, 1962; BOYD, 2008). Since then, studies of the interactions of light in a mean has expressively grown and nowadays there has been a great development of technological applications with optoelectronic and photonic devices. This branch of science focuses on the study of light, the development of devices and equipment that generate, process, collect and detect optical signals generated at a higher speed than electronics. Among the main applications are optical communication, computing, sensors and image processing. (LEPICARD, 2016).

The basis for understanding how these linear and non-linear optical behaviors occur in a medium is based on the principle of understanding what light is and how it interacts with a specific medium. Light is an electromagnetic wave that propagates perpendicularly to the terms that describe it: electric (E) and magnetic (B) fields (WALKER, 2014; SIMMONS, 2000). Considering its propagation in a dielectric material, where the magnetic field can be disregarded, and applying Maxwell's equations for wave propagation, the electric field can then be described as (BOYD, 2008; MUSGRAVES, 2016).

$$E(r, t) = E_0 \left( e^{(ikr - i\omega t)} \right),$$

where  $\omega$  is the pulse of the electromagnetic field that is  $2\pi\nu$  ( $\nu$  is frequency),  $\omega.t$  a time-dependent phase term and  $k.r$  a space-dependent phase term. The direction of

light propagation is indicated by the wave vector  $k$  ( $2\pi n/\lambda$ ,  $n$  is the refractive index and  $\lambda$  the wavelength).

This interaction of the electric field of light with matter, which is considered to be a dipole and thus having its own specific dipole moment, generates microscopic dipole moments. The sum of these moments creates the macroscopic polarization of the medium. This macro polarization as a function of time and space can be expressed in terms of a series of field power (BOYD, RW (2008), MUSGRAVES, & CALVEZ (2016)). In addition, based on the implications and considerations of polarizations in micro and macroscopic scale (homogeneity, time invariance, locality and causality), the nonlinear response of this interaction is presented as a function of multiple wavelengths and is time-dependent. Therefore, for a laser incidence in a medium, its wavelength and pulse duration influence the material's optical response (BOYD, 2008; MUSGRAVES, 2016). Precisely for this reason, femtosecond lasers are commonly used to obtain a non-linear response of certain materials since these lasers have extremely fast pulses of the order of femtoseconds ( $10^{-15}$  seconds), providing a high peak intensity enough for the phenomena of optical non-linearities to occur.

The simplification of material polarization on a macroscopic scale can be given by the following power series (Taylor series):

$$P = \epsilon_0[\chi^{(1)}E + \chi^{(2)}EE + \chi^{(3)}EEE + \dots],$$

where  $\epsilon_0$  is the vacuum permittivity,  $E$  the electric field,  $\chi^1$  the linear susceptibility,  $\chi^2$  the second order susceptibility and  $\chi^3$  the third order susceptibility.

Some non-linear effects are shown in Table 2. The type of symmetry of the materials is described by these susceptibilities. For centimeter-symmetric materials such as glasses, the  $\chi^2$  tensors are null and precisely for this reason second order non-linear effects are not observed in these (BOYD, 2008; MUSGRAVES, 2016).

However, operations breaking the centrosymmetry can be performed in order to enable this non-linear phenomenon in glass, among these operations highlight optical poling, corona poling, thermal poling and glass thermal treatments (LEPICARD, 2016).

Table 2 – Basic electro-optical and non-linear effects observed in dielectrics.

(to be continued)

Order	Tensor	Effect	Description of the effect
2	$\chi^{(2)}(-\omega, \omega, 0)$	Linear electro optical effect (Pockel's effect)	Under the action of an electric field, there is a change of refractive index of the NLO medium. It is observed only in non-centrosymmetrical crystals.
2	$\chi^{(2)}(0, \omega, -\omega)$	Optical detecting	The electric field appears in the NLO medium at illumination.
2	$\chi^{(2)}(-2\omega, \omega, \omega)$	Generation of the second Harmonic of laser emission	The emission of light with a double frequency happens at illumination of the NLO medium.
2	$\chi^{(2)}(-\omega_3, \pm\omega_2, \omega_1)$	Generation of light with total frequency equal to the sum or the difference of frequencies of incident emissions	It is observed at illumination of the NLO medium by two light sources with different frequency (wave length). The emission with the frequency equal to a sum or difference of frequencies of submitting emissions is observed.
3	$\chi^{(3)}(-\omega, \omega, 0,0)$	Quadratic electro optical effect (Kerr's effect)	Because of the action of an electric field there is a change of the medium's refractive index. The medium's refractive index changes in dependence on emission's intensity according to the
3	$\chi^{(3)}(-\omega_2, \omega_1, -\omega_1, \omega_2)$	Nonlinear refractive index	formula: $n=n_0+n_2I$ , where $n_2=6\chi^{(3)}/4\epsilon_0n_0^2c$ . The self-focusing and self-defocusing of the laser beam are the special cases.
3	$\chi^{(3)}(-3\omega, \omega, \omega, \omega)$	Generation of the third harmonic	There is an emission of light with the threefold frequency at illumination of the medium.

Table 2 – Basic electro-optical and non-linear effects observed in dielectrics.

Order	Tensor	Effect	Description of the effect	(conclusion)
3	$\chi^{(3)}(-\omega_4, \omega_1, \omega_2, \omega_3)$	Multiwave mixing	At illumination of the medium by three light sources with different frequencies there is a generation of light with the frequency equal to the sum of the frequencies of incident emissions.	

Reference: Adapted from Musgraves and Calvez (2016).

Among these non-linear effects, Second Harmonic Generation (SHG) is a coherent optical process of radiation of dipoles in non-centrosymmetric materials that depends on the second term of the expansion of polarization ( $\chi^2$ ) (LEPICARD, 2016; BOYD, 2008; MUSGRAVES, 2016; GUENTHER, 2015; SUTHERLAND, 2003). Some examples of materials that present SHG nonlinear susceptibilities are shown in Table 3.

Table 3 – Examples of materials presenting SHG nonlinear susceptibilities.

Material	Class	Element	$\chi^{(2)}(10^{-12} \text{ m/V})$	$\lambda(\mu\text{m})$
Te	32	111	$1.0 \times 10^4$	10.6
LiNbO3	3m	222	6.14	1.06
		322	-11.6	
BaTiO3	4mm	131	-34.4	1.06
		311	-36	
		333	-13.2	
KDP	$\bar{4}2m$	123	0.98	1.06
		312	0.94	
LiIO3	6	331	-11.2	1.06
		333	-8.4	
CdSe	6mm	131	62	10.6
		311	57	
GaAs	$\bar{4}3m$	333	109	10.6
		123	377	

Reference: Modified from Guenther (2015)

This phenomenon was first observed by Franken in 1960 (FRANKEN, 1961) by an experiment in which a 694.30 nm ruby laser was focused on a quartz crystal, passing through it generating, in addition to the refracted beam at 694.30 nm, a signal at 347.15 nm (FRANKEN, 1961). A simplification of second harmonic generation can be seen in Figure 6 in which two photons of the same frequency  $\omega_i$  combine to produce a new and single photon with double the frequency  $2\omega_i$  (double energy), considering that this is a light of high intensity and with conservation of energy and momentum during this process. SHG could be described as a phenomenon with a quadratically filed strength result from part of atomic interaction that, consequently, produces the square of the intensity of the incident light. However, as it was seen that macroscopic polarization in a medium behaves according to a series of power, linear responses are also expected.

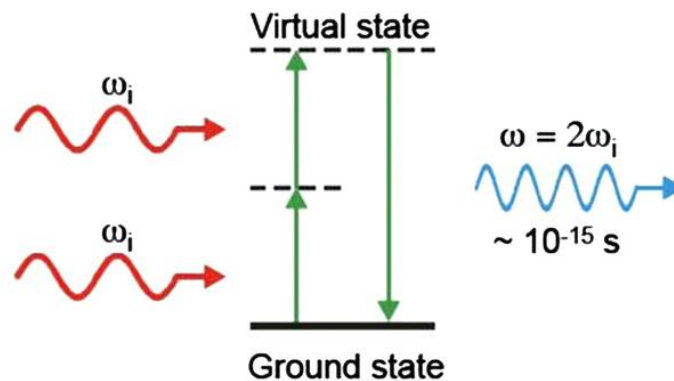


Figure 6 – Two incident photons ( $\omega_i$ ) generating another photon of different frequency ( $2\omega_i$ ).

Reference: Modified from Pantazis (2010)

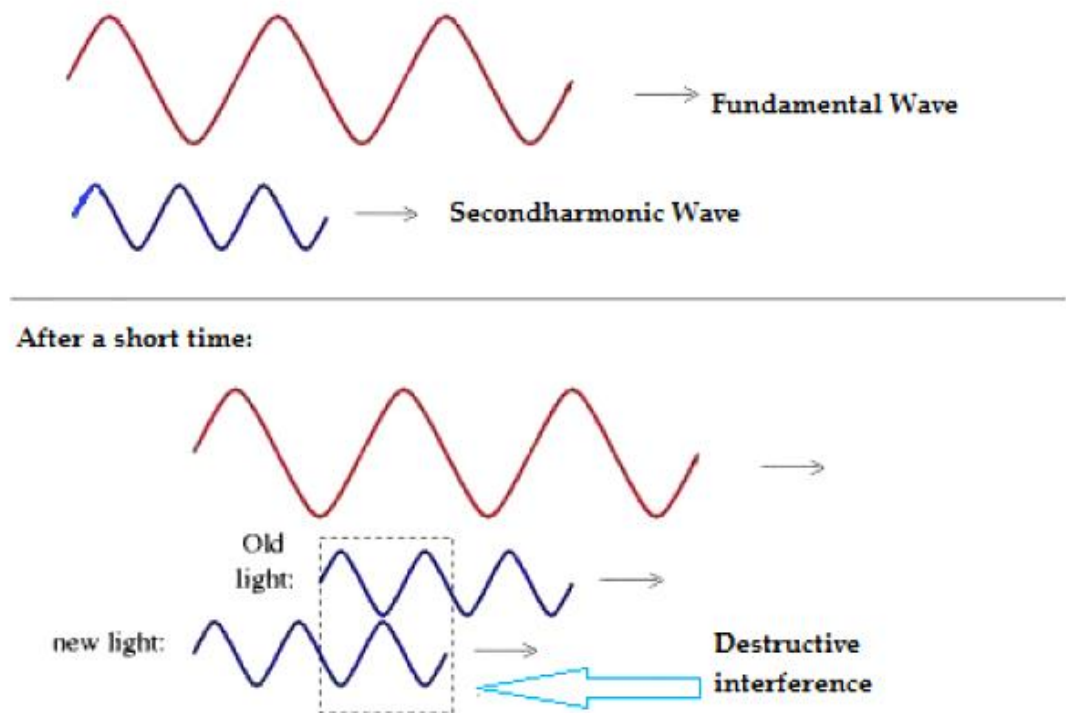


Figure 7 – SHG without phase matching.

Reference: Modified from March (2001)

An explanation of the mechanism for this phenomenon, according to the quantum mechanical theory of radiation, would occur when a molecule in the middle leaves the ground state at an intermediate level during the destruction of two photons coming from the initial light waves and then returns to the state initial emitting second harmonic radiation (FIGURE 7). Since there are conservation of energy and momentum, the two radiated electric field  $\omega_i$  and  $2\omega_i$ , as result, are in matching phases, in which their refractive indices in the medium are the same, that is, these waves propagate with the same speed and are consistent. However, if there are dispersions in the medium the phase matching does not occur. Therefore, the refractive index of the medium at the fundamental and second harmonic wavelengths will be different and then a destruction interaction of the SHG waves takes place, decreasing SHG signals. (FIGURE 7). Some common techniques could be applied in order to obtain phase matching such as playing with the birefringence of the crystals

to eliminate phase mismatch and periodically poled, generally used for glass materials, which corrects the wave phase at regular intervals.

Recently, there has been a huge application for electro-photonic and photonic materials and gradually they are substituting electric materials (LEPICARD, 2016). Specifically, from SHG effect there are many uses in communication, radio, optical fibers, computing, microelectronics, sensors, building up equipment and materials and on biological imaging materials once it doesn't photodamage (there are no energy levels excitation in this process) the biological cells (KATO, 2019; LEPICARD, 2006; TRAN, 2017; JIANG, 2020; WALLIS, 1969; ABEYSINGHE, 2001; ABEYSINGHE, 2002; SIMON, 2015; PANTAZIS, 2010; PRUNERI, 1999; MARGULIS, 2009; HUANG, 2015; STAVROULA, 2019; YOU, 2019). Therefore, it is a non-invasive technique with also the advantage of non-demand of the use of dyes, therefore it brings important biological applications, including SHG microscopy (KATO, 2019; NIKOLENKO, 2003; TRAN, 2017; JIANG, 2020). In addition, SHG applications are seen also on characterization of nanocrystals due to their polarization sensitivity and specific material symmetries (PANTAZIS, 2010; SIMON, 2015). Finally, SHG application enables better understand and study of properties of thin films and materials with few atomic layers (YING, 2019; YOU, 2019; STAVROULA, 2019; GIELIS, 2008, JIANG, 2020)

## CHAPTER 2

---

### **METHODOLOGY:**

This chapter introduces the instruments and experimental procedure and techniques used in this work.



## 2.1 SYNTHESIS OF ALKALINE TANTALUM GERMANATE GLASSES

Alkaline tantalum germanate glasses (GM) were prepared by the traditional melt-annealing method (MARCONDES, 2017; PIETRO, 2015; ZERLIM, 2008) with molar composition of  $(100-x)\text{GeO}_2-10\text{M}_2\text{O}-x\text{Ta}_2\text{O}_5$  being  $x = 15$  or  $20$  mol % and alkaline metal  $M = \text{Na}, \text{K}$  or  $\text{Rb}$ . Each component ( $\text{GeO}_2$ ,  $\text{Ta}_2\text{O}_5$  and  $\text{M}_2\text{CO}_3$ ) has a high analytical purity reagent grade, being 99.9 % for  $\text{GeO}_2$  and  $\text{Ta}_2\text{O}_5$  (from Sigma-Aldrich Corp.) and 99.95-100.05% for  $\text{M}_2\text{CO}_3$  (from Alfa Aesar GmbH & Co KG). The glass synthesis sketch is showed in Figure 8. Reactants were weighting according with the molar composition proposed, mixed in an agate mortar and heated for 1 hour at 400 °C and then another 1h or 9h at 1500 °C in crucibles of Pt/Au or pure Pt, according to Table 4. The crucible bottom, with the resulting melting liquid in it, was fast cooled in a tank filled with room temperature water until the inside liquid became a glassy material. Annealing process was performed at 550 °C for 6 h and then cooling down to room temperature at  $1\text{ }^\circ\text{C}\cdot\text{min}^{-1}$ . The alkaline tantalum germanate glass samples (GM) were optically polished up to around 2 mm and named as GNa1, GNa2, GNa3, GK and GRb according to their molar compositions, melting time and crucible type as shown in Table 4.



Figure 8 – Glass synthesis sketch.

Reference: Author

Table 4 – Glass sample labels.

GM glasses						
Metal	Molar rate			Crucible	Melting time (h)	Glass samples/GM
	GeO <sub>2</sub> (%)	M (%)	Ta <sub>2</sub> O <sub>5</sub> (%)			
Na	75	10	15	Pt/Au	1	GNa0
	75	10	15	Pt/Au	9	GNa1
	70	10	20	Pt/Au	1	GNa2
K	70	10	20	Pt	1	GNa3
	70	10	20	Pt	1	GK
Rb	70	10	20	Pt	1	GRb

Reference: Author

## 2.2 SYNTHESIS OF ALKALINE TANTALUM GERMANATE GLASS CERAMICS

Alkaline tantalum germanate glass ceramics (GCM) were obtained from the GM glass samples under different thermal treatments (1 h up to 624 h) and temperatures (750 up to 850 °C) in oven, under air atmosphere. Glass ceramic synthesis sketch is shown in Figure 9. They were labeled according to their specific temperatures and times set during thermal treatments: GCM-T-t, where M is the alkaline metal (Na, K or Rb) from the precursor glass, T in °C is the temperature and t is the time in hours as shown in Table 5.



Figure 9 - Glass ceramic synthesis sketch.

Reference: Author.

Table 5 – Glass ceramic sample labels.

(to be continued)

<b>Glass Ceramics (GC)</b>				
Glass samples	Heating temperature/T (°C)	Treatment time/t (h)	Samples/GCM-T-t	Glass ceramic group
GNa0	700	24	GNa0-700C-24h	GCNa
	720	24	GNa0-720C-24h	
	750	24	GNa0-750C-24h	
	780	24	GNa0-780C-24h	
	800	24	GNa0-800C-24h	
GNa1	700	24	GNa1-700C-24h	
	720	24	GNa1-720C-24h	
	750	24	GNa1-750C-24h	
	780	24	GNa1-780C-24h	
	800	24	GNa1-800C-24h	
GNa2	700	24	GNa2-700C-24h	
	720	24	GNa2-720C-24h	
	750	24	GNa2-750C-24h	
	780	24	GNa2-780C-24h	
	800	24	GNa2-800C-24h	
GNa3	700	24	GNa3-700C-24h	
	720	24	GNa3-720C-24h	
	750	24	GNa3-750C-24h	
	780	0.17	GNa3-780C-0.17h	
	780	0.33	GNa3-780C-0.33h	
	780	0.5	GNa3-780C-0.5h	
	780	0.67	GNa3-780C-0.67h	
	780	1	GNa3-780C-1h	
	780	1.5	GNa3-780C-1.5h	
	780	2	GNa3-780C-2h	
	780	2.5	GNa3-780C-2.5h	
	780	3	GNa3-780C-3h	
	780	3.5	GNa3-780C-3.5h	
	780	4	GNa3-780C-4h	
	780	4.5	GNa3-780C-4.5h	
	780	5	GNa3-780C-5h	
	780	6	GNa3-780C-6h	
780	24	GNa3-780C-24h		
800	1	GNa3-800C-1h		

Table 5 – Glass ceramic sample labels.

				(conclusion)
<b>Glass Ceramics (GC)</b>				
Glass samples	Heating temperature/T (°C)	Treatment time/t (h)	Samples/GCM-T-t	Glass ceramic group
	800	2	GCNa3-800C-2h	
	800	10	GCNa3-800C-10h	
	800	18	GCNa3-800C-18h	
	800	20	GCNa3-800C-20h	
	800	48	GCNa3-800C-48h	
	800	72	GCNa3-800C-72h	
	800	96	GCNa3-800C-96h	
	800	164	GCNa3-800C-164h	
	800	256	GCNa3-800C-256h	
	800	624	GCNa3-800C-624h	
	850	1	GCNa3-850C-1h	
GK	800	72	GCK-800C-72h	GCK
GRb	800	72	GCRb-800C-22h	GCRb

Reference: Author

## 2.3 CHARACTERIZATIONS

### 2.3.1 X-ray diffraction measurements

X-ray diffraction (XRD) analysis were performed using two different equipment. X-ray diffraction patterns of the glass ceramic GC-800-624h and the powder  $\text{Na}_2\text{Ta}_8\text{O}_{21}$  were collected at room temperature, by the diffractometer PANalytical X'pert PRO with a secondary monochromator and X'Celerator multi-strip detector. The monochrome  $\text{Cu-K}\alpha_1$  radiation was generated at 45 kV tension, 40 mA current. For the starting glasses and glass-ceramics, a diffractometer Philips X'Pert Pro, equipped with high temperature camera Anton Paar HTK16 (1600°C) in air and with scintillation detector, was used to collect data from the pristine glass at room temperature and X-ray patterns were collected inside the chamber after different heat treatment times at 800C (2, 10, 18, 72 and 624 hours). For this set, the  $\text{Cu-K}\alpha_1$  radiation was generated at 50 kV tension, 40 mA current.

### 2.3.2 Thermal analysis

DSC characterizations were performed on a Netzsch STA 449 F3 Jupiter calorimeter. The samples were processed in glassy form in monoliths and in powder form, for comparison, with mass between 30 and 45 mg, in a Pt / Rh crucible, capped and in an N<sub>2</sub> atmosphere, with a crucible of the same type and empty as reference. The scans were performed from 200 to 1200 °C, with a heating rate of 10 °C / min. Finally, a crystallization study was carried out at rates of 5, 15 and 20 °C / min; as well as a study of crystallization as a function of time.

### 2.3.3 UV-Vis absorption spectroscopy

The absorption measurements in the UV-Vis region, from 300 to 700 nm, were performed on a Cary 7000 Agilent spectrophotometer. The measurements were performed on polished bulk samples, with thickness measured with the aid of a digital caliper.

### 2.3.4 Infrared spectroscopy

The absorption measurements in the near infrared range, 700 to 2500 nm, were performed in a Cary 7000 Agilent spectrophotometer. In the 2500 to 4000 nm region, a Cary 630 FTIR spectrophotometer. Measurements were performed in bulk pieces, optically polished and presenting thickness measured by a digital caliper.

### 2.3.5 Ellipsometry measurements

Ellipsometry measurements were performed using an imaging null-ellipsometer EP3 (Nanofilm). The instrument was used in total internal reflection mode and both the intensity and the phase changes of the reflected light were monitored and converted into the ellipsometric angles  $\Psi$  and  $\Delta$ . Spectroscopic ellipsometry data were recorded in air at constant angle of incidence (AOI = 70°) and different wavelengths ( $\lambda$  = 400 - 906 nm). The measurements were systematically performed for each step of the assembly build-up on several regions of interest from each

sample. The data were acquired and evaluated by EP3View V235 Software (Nanofilm). For modeling, EP4Model 1.0.1 software (Nanofilm) was used.

### 2.3.6 Density measurements

Density was measured by the method buoyancy, Archimedes Principle, 5 times for each sample. Having silica dioxide as reference and density working between 2.2202 to 2.205 g.cm<sup>-3</sup>. Diethyl phthalate density were considerate at each measurement according to each momentum temperature. The expression used was  $\rho = \frac{m_a}{m_a - m_d} \rho_d$ , where  $\rho$  = sample density,  $m_a$  = sample weight in air,  $m_d$  = sample weight in diethyl phthalate and  $\rho_d$  = diethyl phthalate density adjusted at each temperature.

### 2.3.7 Energy dispersive X-ray spectroscopy

Energy-Dispersive X-ray Spectroscopy (EDS) analysis it was used a JEOL SEM (JSM 6360A) with an EDS detector (Si-Li). It was used voltage of 15 kV, Probe Current of 1.00000 nA and working distance of 10 mm. Finally, it was performed as correction the ZAF method standardless for quantitative analysis.

### 2.3.8 Auger electron spectroscopy

Auger Electron Spectroscopy (AES) was performed using the PHI 710 Scanning Auger Nanoprobe. This equipment is set with a field emission source (FEG) as electron gun, coaxial cylindrical micro analyzer and secondary electron detector for imaging. Samples were metallized with Au (3 - 5 nm) and finally the sample holder tilt at 30° plus tilt 45° for image compensation. It was used voltage of 5.000 kV, acquisition of 3 pts, resolution of 128 and time per step of 10 ms.

### 2.3.9 Micro Raman and SHG measurements

Correlative micro-Raman and micro-SHG measurements were recorded in backscattering mode on a modified microRaman spectrometer HR800 (Horiba/Jobin Yvon) at room temperature. A continuous wave laser operating at 532 nm is used for

Raman and a picosecond pulsed laser at 1064 nm is used for micro-SHG measurements. Typical resolution used for Raman is  $2.5 \text{ cm}^{-1}$ . The objective used was a 100× long working distance with a numerical aperture of 0.5 from Mitutoyo, allowing for a resolution in the X–Y plane of  $0.8 \text{ }\mu\text{m}$  for Raman and SHG micro measurements.

### 2.3.10 Macro SHG measurements

For macro-SHG measurements, the laser source was a 10 ns OPO intracavity (Photonics Industry) operating at 1550 nm at a repetition rate of 30 Hz with a maximum pulse energy of  $100 \text{ }\mu\text{J}$  during a 20 ns pulse and fundamental unfocused (collimated) beam with a diameter of  $\sim 3200 \text{ }\mu\text{m}$ . The experimental sketch is shown in Figure 10 (RODRIGUEZ, 2008). For both scans, the incident laser beam and SHG signal are detected in transmission mode. Finally, all SHG intensities were corrected from the setup conditions (photomultiplier sensitivity) and incident laser intensity ( $I_{2\omega}/I_{\omega}^2$ ).

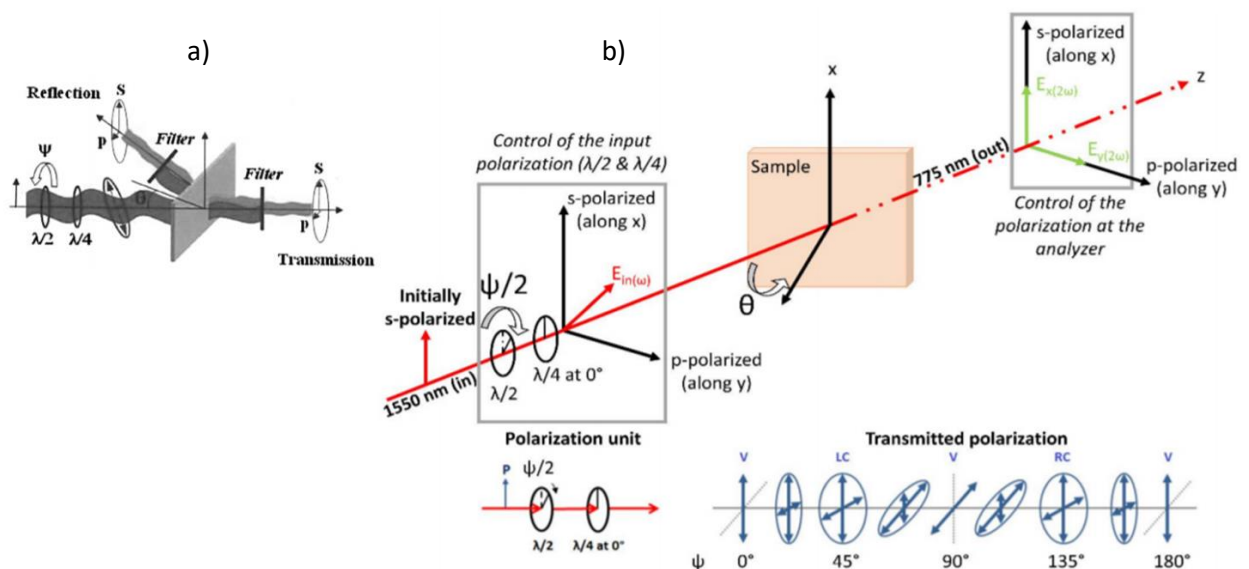


Figure 10 – (a) Experimental setup sketch for linear and non-linear optic measurements for both acquisitions in transmission or reflection while (b) detailed way in transmission mode. For the  $\theta$ -scan the incident angle  $\theta$  is modified at a fixed incident polarization, while for  $\psi$ -scans the incident polarization is modified by rotating a half-wave plate ( $\psi$ ) with fixed angle of incidence  $\theta$ .

Reference: Modified from Rodriguez (2008) and Lepicard (2018).

Two types of scan are measured in transmission mode with this set-up. The first one is known as a  $\theta$ -scan as the measurement is made as a function of incident angle ( $\theta$ ) with fixed incident and harmonic polarization p (horizontally) or s (vertically). The second type of scan is a  $\psi$ -scan where the incident angle is fixed and so is the polarization at the analyzer (s or p). The measurement is done as a function of the polarization state of the incident beam (linear, circular or elliptical).



## CHAPTER 3

---

### **ALKALINE TANTALUM GERMANATE GLASSES:**

This chapter shows the experimental characterizations and discussion for the alkaline tantalum germanate glass samples synthesized according to the methodology section in Chapter 2.

### 3.1 SYNTHESIS PROCESS AND GENERAL ASPECTS

The glass samples GNa0, GNa1, GNa2, GNa3, GK and GRb were prepared by the traditional melt-quenching method with molar composition  $(1-x)\text{GeO}_2 \cdot (x)\text{Ta}_2\text{O}_5 \cdot 10\text{M}_2\text{O}$  presented as a glassy material aspect after the fast cooling to the room temperature. Those glassy materials are presented in the Figures 11-13.

10 g of the GNa0 composition was synthesized with 15 % mol of  $\text{Ta}_2\text{O}_5$  in Pt/Au crucibles under 2 h at 1500 °C and due to their small thickness, one could not obtain large pieces, but rather shattered of around 1.6 mm. They appear transparent to visible light, however, with light yellow color aspect (FIGURE 11a). Whole pieces were only obtained from 20 g of material, giving at around 2.6 mm ( $\pm 0,02$  mm) for GNa1, after polishing. On making glasses, thickness plays an important role. Too fast cooling for thick material could favor crystallization process once their interior could suffer slower decrease in temperature relating to external areas. However, thin materials could be more sensible to mechanical distress leading to cracks, even with long times such as 24 h under annealing. This annealing process is important once it reduces internal tension in the glasses by creating a long cooling process time (generally decreasing of 1 °C per minute) from a high temperature (set generally before the glass  $T_g$ ) to a room temperature. Therefore, this thickness control is important in order to obtain whole glass pieces and this parameter is related to the contribution of each glass material component.

GNa1 samples were prepared with melting time of 9 h, showing a glass with golden color aspect to the visible light as shown in (FIGURE 11b-c). These yellow/golden aspects are likely to be related to some contamination during melting time process, rather than evaporation since both gave a mass loss of about 5 % after melting. Higher the melting time at 1500 °C, stronger the yellow golden aspect.

GNa2 glass was synthesized with 20 g in total mass in Pt/Au crucibles under 1 h at 1500 °C, however with 20 % of  $\text{Ta}_2\text{O}_5$  and it was obtained whole and stable glass pieces after annealing of 9 h as shown in Figure 12. The given thicknesses were around 1.94 mm ( $\pm 0,002$  mm) and still presenting light golden color aspect.

In order to avoid possible contamination from Pt/Au crucibles, GNa3 glasses were prepared in pure Pt crucible, under the same experimental conditions as sample GNa2 and presented a thickness around 2.7 mm ( $\pm 0,002$  mm) after

polishing. For those glasses the yellow/golden color aspect decreased considerably as shown in Figure 13a. Therefore, one can suggest that the contamination from non-pure Pt crucibles generate a yellow color that may be related to gold or even platinum in the glass matrix. Finally, the glass samples GRb and GK, in Figure 13b-c, were synthesized using the same conditions as for GNa3, and it is possible to notice that GK is showing a higher transparency (FIGURE 13).

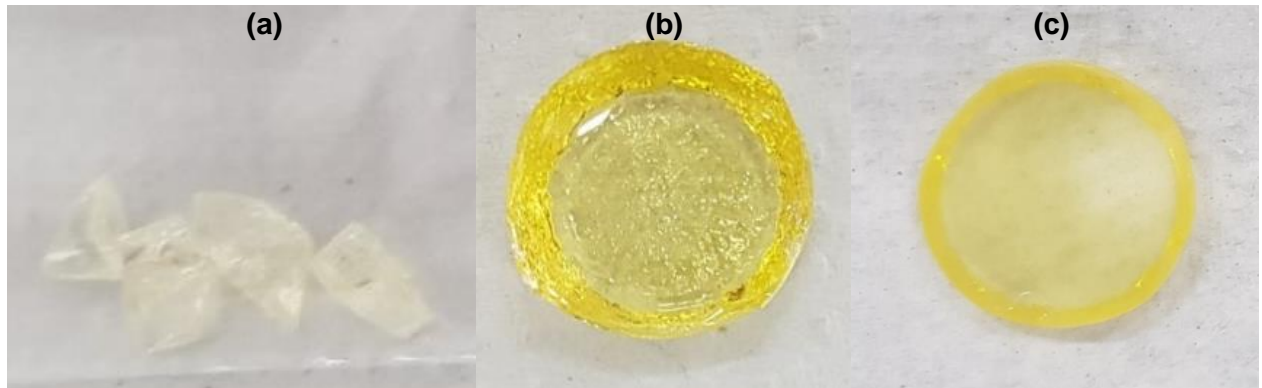


Figure 11 – Images of a) shattered GNa0 glass obtained under 1 h in thermal treatment, b) GNa1 glass after 9 h under thermal treatment not polished and c) optically polished, all of them with molar rate of  $75\text{GeO}_2.15\text{Ta}_2\text{O}_5.10\text{Na}_2\text{O}$  made in Pt/Au crucible.

Reference: Author.

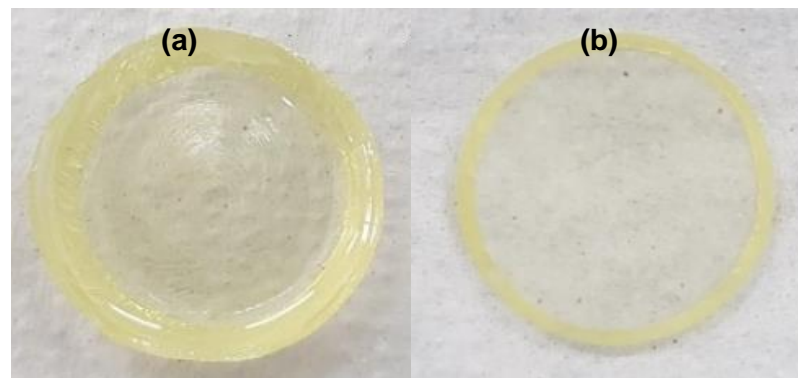


Figure 12 – Images of the GNa2 glass under 1 h in thermal treatment a) unpolished and b) optically polished, with molar rate of  $70\text{GeO}_2.20\text{Ta}_2\text{O}_5.10\text{Na}_2\text{O}$  made in Pt/Au crucible.

Reference: Author.

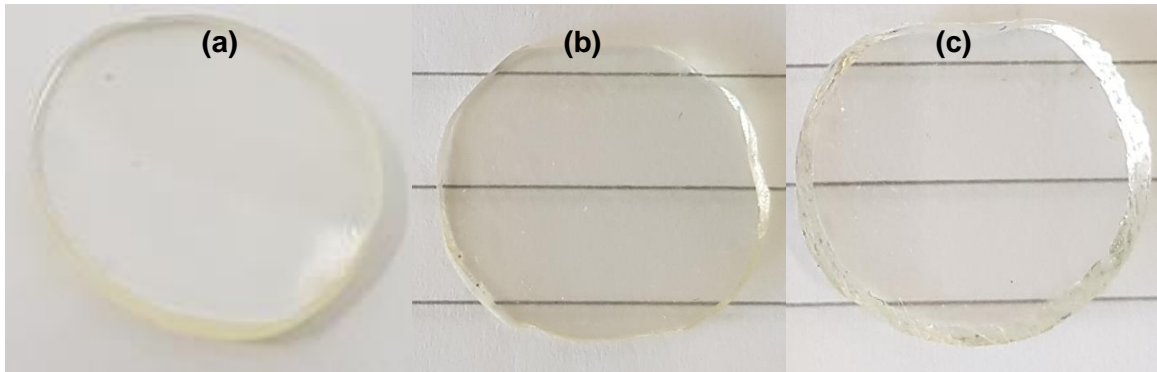


Figure 13 – Images of optically polished glasses under 1 h under thermal treatment of a) GNa3  $70\text{GeO}_2.20\text{TaO}_2.10$  b) GRb  $70\text{GeO}_2.20 \text{ Ta}_2\text{O}_5.10\text{Rb}_2\text{O}$  and c) GK  $70\text{GeO}_2.20\text{TaO}_2.10\text{NK}_2\text{O}$ , being those samples performed in pure Pt crucible.

Reference: Author.

### 3.2 THERMAL ASPECTS

Thermal measurements give important information about glass stability and structural changes in the material such as the crystallization process, among others (HOFSTETTER, 1997; SANDITOV, 2007; GUEDES, 2020; MARCONDES, 2019; CARTER, 2007). The DSC curves for GNa glass samples in Figure 14 show similar profiles, presenting a glass transition ( $T_g$ ), an onset of the first crystallization event ( $T_{x1}$ ), a complete first crystallization temperature ( $T_{c1}$ ), with an intense crystallization peak, and another weak exothermic event ( $T_{c2}$ ). When the temperature approaches  $T_x$  it is seen the onset for crystals precipitation with its maximum peak of crystallization at  $T_c$ , which means maximum speed of crystallization for this exothermic event (HOFSTETTER, 1997).

One can notice that with the molar increase of  $\text{Ta}_2\text{O}_5$ , the crystallization events shift to the left, that is, to lower temperatures. The values of  $T_g$ ,  $T_{c1}$ ,  $T_{x1}$  and  $T_{c2}$  for GNa1 (15%  $\text{Ta}_2\text{O}_5$ ) are at around 692, 843, 860 and 890 °C, respectively. While GNa2 and GNa3 (20%  $\text{Ta}_2\text{O}_5$ ) show similar profiles and temperature for exothermic events at around 709, 800, 814 and 865 °C, respectively. The interval between  $T_g$  and  $T_x$ , shows possible temperatures where viscosity allows such mobility that is essential for glass forming and stabilization against crystallization

(HOFSTETTER, 1997; SANDITOV, 2007; CARTER, 2007). As short is this interval, less stable will be to form glass once is greater its tendency towards crystallization.

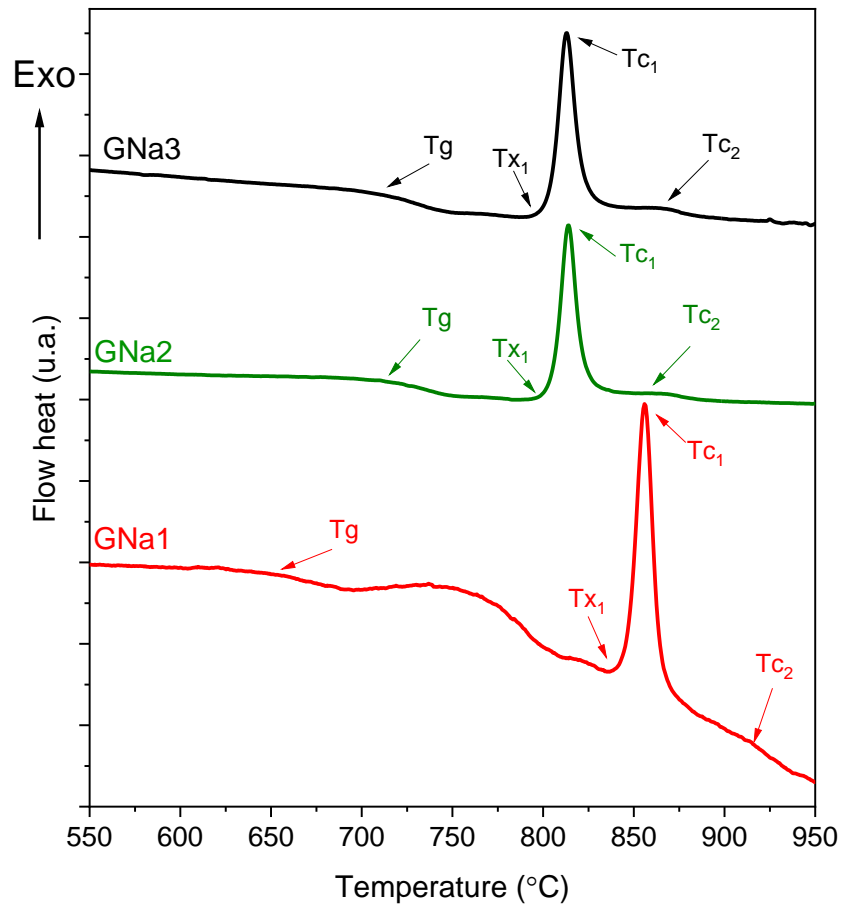


Figure 14 – DSC curves for GNa glasses.

Reference: Author.

From general analyses, these GNa glasses are relatively stable against devitrification showing the temperature interval  $T_{x1}-T_g$  at around 183 °C for GNa1 and 91 °C for GNa2 and GNa3. Therefore, the thermal stability is greater for samples with 15% molar ratio of  $Ta_2O_5$  since they presented this larger thermal range, showing a greater tendency to form glass. This assumption was also visualized during the experimental procedure, since glasses containing 20%  $Ta_2O_5$  (thermal range of 91 °C) crystallized easily during the glass formation process, making necessary a faster thermal shock. However, this behavior is expected since there is a decrease in the

GeO<sub>2</sub> glass former and an incorporation of the intermediate Ta<sub>2</sub>O<sub>5</sub>. Finally, even though intervals were found to be around 100 °C or shorter, they are suitable enough to form stable glasses (CUNHA, 2018; POIRIER, 2019) and possible fibers.

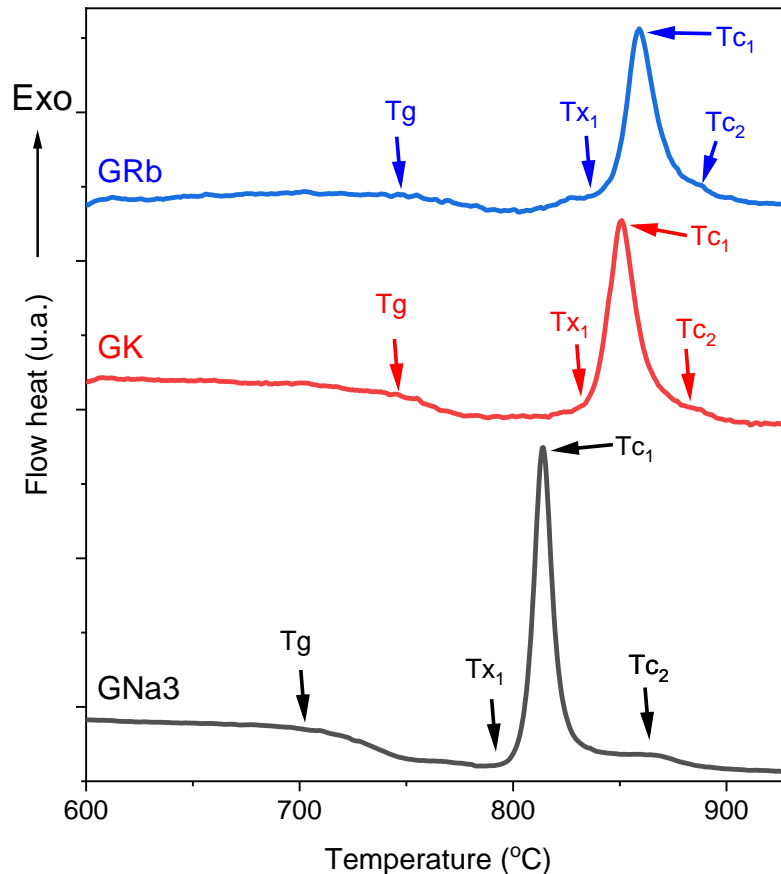


Figure 15 – DSC curves for GNa3, GK and GRb glasses.

Reference: Author.

As for the GRb and GK glasses, DSC analyses in Figure 15 also showed similar curves comparing to GNa glasses. However, exothermic events presenting temperatures for T<sub>g</sub>, T<sub>c1</sub>, T<sub>x1</sub> and T<sub>c2</sub> at around 747, 831, 850 and 884 °C, respectively, for the GK sample while for GRb, these same event points are at around 750, 835, 859 and 889 °C, respectively. The thermal stability seems to be similar for these glasses comparing with GNa3. Therefore, they are also suitable enough to form glass and possible fibers synthesis which requires such minimum interval values of thermal stability during its forming process similar to those

presented by these samples. Finally, GNa glass had its  $T_c$  at around 814 °C, much lower comparing to GK and GRb glasses with their  $T_c$  at around 850 and 859 °C, respectively. Such behavior could be related to the alkaline metal electronegativity of Na, K and Rb that could lead a stronger interaction bonding in the glass matrix, that grows from Na to Rb.

### 3.3 STRUCTURAL CHARACTERISTICS

#### 3.3.1 Glass Raman analysis

Raman spectroscopy is an important key to identify and validate materials structures and compounds once it shows specific band shifts. In this study, setting the alkaline metals Na, K and Rb, at same content, Raman spectra curves are very similar to each other, indicating that these glasses have also similar network composition. These Raman curves as seen in Figure 16, along with GeO<sub>2</sub> glass (CHIASERA, 2013), GeO<sub>2</sub> crystalline trigonal (CHIASERA, 2013; TSUTOMU, 1998; GIRI, 2012; TRUKHIN, 2005; MERNAGH, 1997; MADON, 1991; MICOULAUT, 2006) and Ta<sub>2</sub>O<sub>5</sub> amorphous (JOSEPH, 2012) curves for comparison.

From general analyses, taking the amorphous nature of GeO<sub>2</sub> in these samples and the most intense band showed at around 480 cm<sup>-1</sup> (due Ge-O-Ge bending modes [53, 55, 58, 60]), the glass network should present four-membered rings of GeO<sub>4</sub> and three-membered rings of GeO<sub>4</sub>. Specifically, 390-430 cm<sup>-1</sup> to symmetrical stretching of Ge-O bonds in rings of 4 GeO<sub>4</sub> tetrahedrons and 480-510 to symmetrical stretching of Ge-O bonds in rings of 3 GeO<sub>4</sub> tetrahedrons (HENDERSON, 1991). The proportion of these rings are related to the alkaline modifier incorporated in the glass network, as shown for the germanate anomaly (ALDERMAN, 2017; EVSTROPIEV, 1963; MURTHY, 1964; KOROLEVA, 2019; ZHANG, 2017). Since in these samples the ratio of Na, K and Rb were the same, they are expected to present similar Raman curves. Furthermore, considering the most intense band at around 480 cm<sup>-1</sup>, in these glass samples, the rings are built mainly from GeO<sub>4</sub> tetrahedrons. In fact, the bands at around 780-862 cm<sup>-1</sup> and 900-920 cm<sup>-1</sup> are related to tetrahedrons, due symmetrical stretching of the Ge-O terminal connections in Q<sup>2</sup> tetrahedrons and to antisymmetric stretching of the Ge-O terminal connections in Q<sup>2</sup> tetrahedrons, respectively (HENDERSON, 2010). This may also

suggest that the  $\text{GeO}_4$  tetrahedrons have 2 terminal  $\text{Ge-O}^-$  connections and 2 connections  $\text{Ge-O}$  ( $\text{Ge-O-Ge}$ ) that could be formed due the incorporation of the alkaline modifier ( $\text{Na}_2\text{O}$ ,  $\text{K}_2\text{O}$  and  $\text{Rb}_2\text{O}$ ), in which may break the covalent network. Finally, the band at around  $590\text{-}610\text{ cm}^{-1}$  is related to stretching of  $\text{Ge-O}$  connections in  $\text{GeO}_6$  octahedra (HENDERSON, 1991; MONTEIRO, 2011) and, finally,

As for Ta compounds, the abroad band between  $250\text{-}300\text{ cm}^{-1}$  is related to deformations of  $\text{O-Ta-O}$  bonds in  $\text{TaO}_6$  octahedra (JOSEPH, 2012) and  $680\text{-}700$  to stretching of  $\text{Ge-O-Ta}$  connections (CHOWDARI, 1989; HENDERSON, 2010), therefore, It may be expected the formation of  $\text{Ge-O-Ta}$  by  $\text{TaO}_6$  units. Hence, it may suggest that tantalum oxide is a network intermediary and not a modifier. Therefore, it does not break the covalent germanate network, but it is probably incorporated in this network (HENDERSON, 1991, PIETRO, 2015). These results may be the reason why Raman analyses are showing mostly bands for the glass former  $\text{GeO}_2$ .

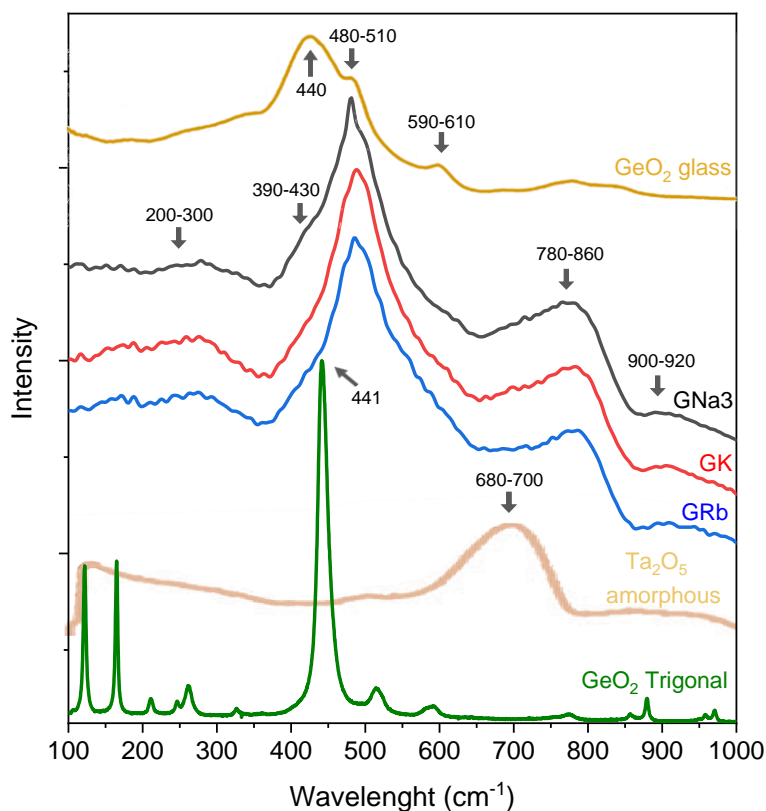


Figure 16 – DSC curves for GNa3, GK and GRb glasses.

Reference: Author.



### 3.3.2 Glass x-ray diffraction analysis

The DRX technique provides important information regarding the composition of a material and its crystalline phases presented. The diffractograms show that the synthesized samples are glasses since they do not have crystallinity peaks, but rather profiles of amorphous materials, with a halo characteristic. All of the glass samples showed similar halo profile such those in Figure 17. This analysis is important in order to evaluate that after the quenching process the obtained materials are indeed amorphous, in other words, indicates glassy materials.

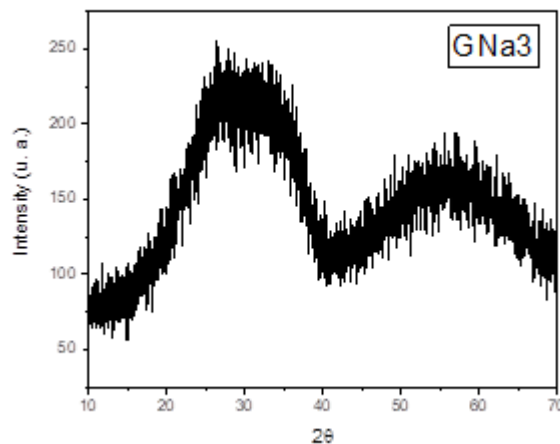


Figure 17 – Diffractogram of GNa3 glass

Reference: Author.

## 3.4 GENERAL PHYSICAL AND OPTICAL FEATURES

### 3.4.1 Density and refractive analysis

The glass samples GNa3, GRb and GK were investigated by the method buoyancy, giving the correlation presented in the inset of Figure 18. The densities of these glasses were respective 5.230, 5.048 and 5.039 g.cm<sup>-3</sup>. Since the alkaline Na has its atomic radius smaller than K and Rb, the glass GNa3 was expected to have a

higher density comparing to the others ones for same molar composition, occupying less volume per mol in the structure. It was also performed ellipsometry measurements on the surface of the same glasses in order to verify any changes in the refractive index and the results were fit with the Cauchy equation (GOOCH, 2007) as shown in Figure 18. The GNa3, GK an GRb bulk glasses had thickness between 0.5 to 0.6 mm. The refractive index values had good fitting according to the root square of Cauchy equation, which is used for UV and Visible region. They also directly decreased according to the atomic radius, having higher values for Na, then K and finally Rb glasses.

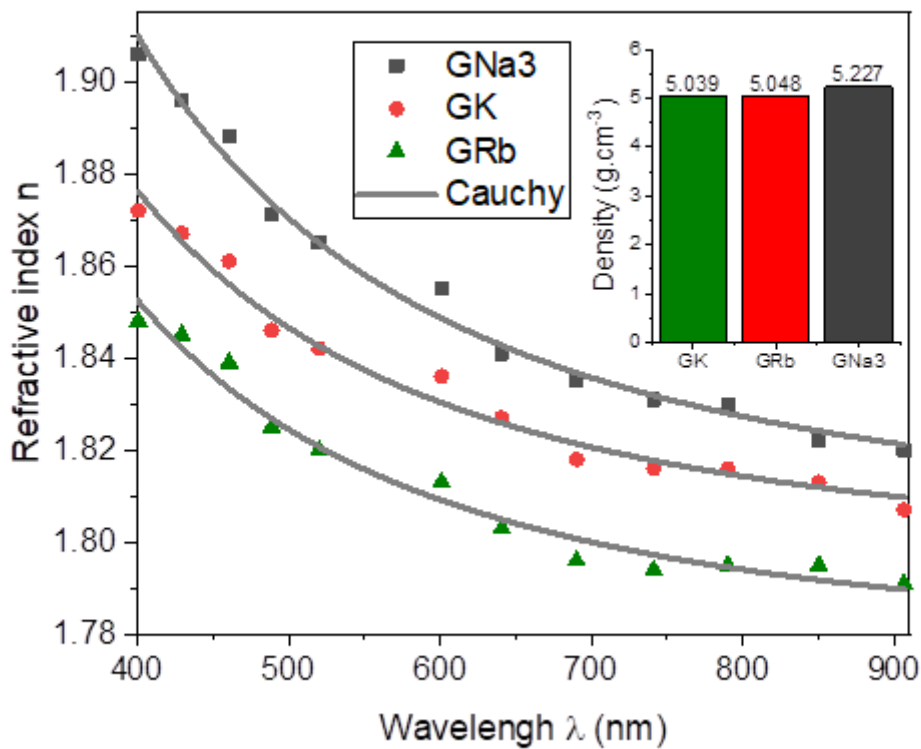


Figure 18 – In a) refractive index in function on wavelength (nm) for the samples GNa3, GRb and GK fit in Cauchy equation and b) their respective density.

Reference: Author.

### 3.4.2 UV-Vis-IR spectroscopy

Using the UV-Vis and NIR absorption data, it was possible to obtain the materials transparency window and their respective band gap values in Figure 19. The transparency window of a material provides the region of the electromagnetic spectrum where the glass matrix absorbed or transmit light. For the calculations, the absorption coefficient given by the Beer-Lambert Law (HARRIS, 2012) was considered, according to the specific thickness of each sample.

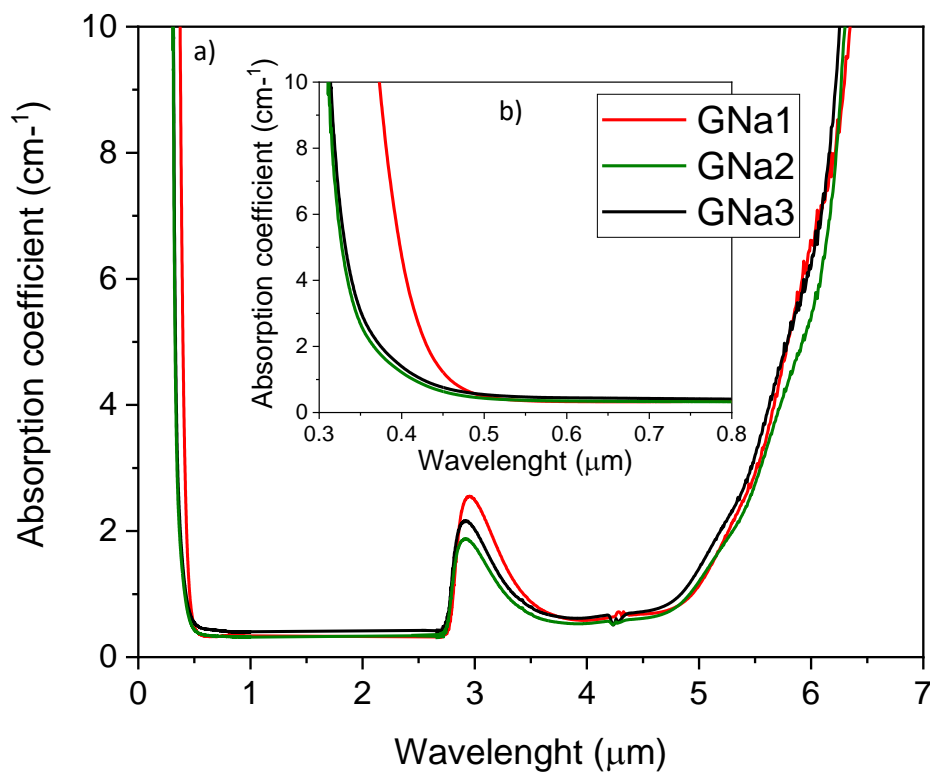


Figure 19 – Spectra of GNa1, GNa2 and GNa3 glasses, showing (a) optical window and (b) absorption in the UV-visible

Reference: Author.

The synthesized GNa glasses have a transparency window in the range of 0.5 to 5.5  $\mu\text{m}$ , presenting similar profiles. The region around 0.4 and 0.7  $\mu\text{m}$  is highlighted in the inset of Figure 19 and defines the color given by a material if there is an absorption light process in this range. Above 5  $\mu\text{m}$ , multiphonon absorption processes related with the germanate vibrational modes are responsible for the

absorption. Finally, the band visualized in all samples at around 2.7  $\mu\text{m}$  represents the absorption of light by the -OH connection from water or O-H terminal connections in the vitreous network (HARRIS, 2012). It is possible to visualize that this band decreases with the molar increase of  $\text{Ta}_2\text{O}_5$ , thus higher concentrations of  $\text{Ta}_2\text{O}_5$  favors the obtaining of materials with greater transparency, suggesting that in these the water retention in the vitreous network was lower.

Comparing GNa3 with GRb and GK glasses it is also possible to see similar profiles (FIGURE 20), however, the transparency broadens. Approximately, GRb optical window range goes from 0.5 to 5.7  $\mu\text{m}$ , while GK from 0.4 to 6.2  $\mu\text{m}$ . In addition, GK presented a decrease in the band at 2.7  $\mu\text{m}$  that could indicate less hydroxyl retention.

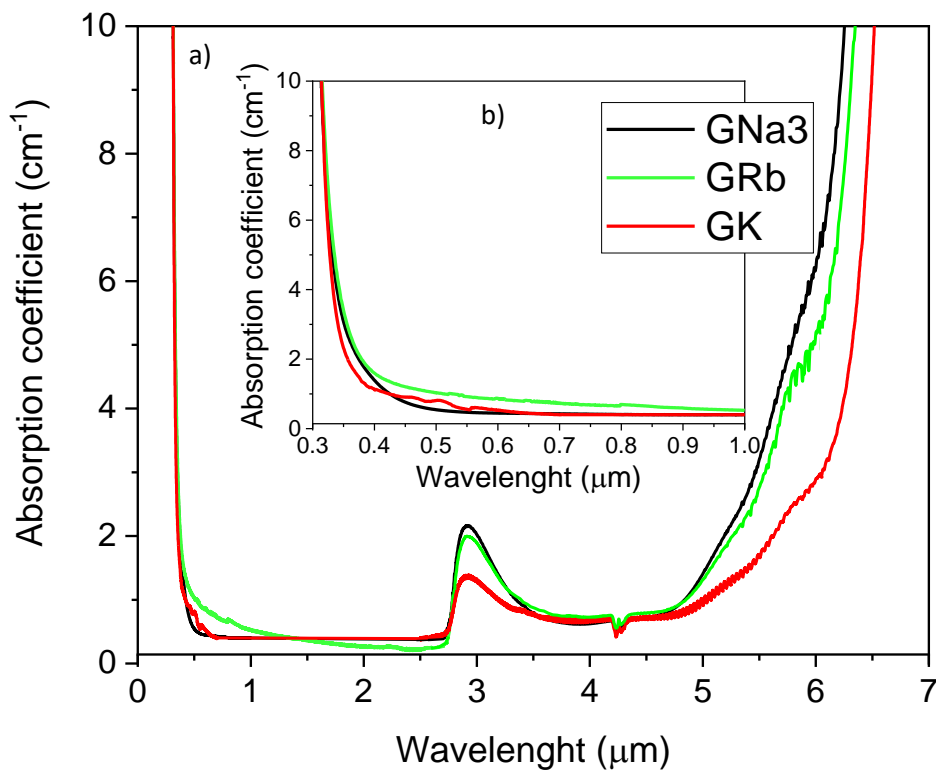


Figure 20 – Spectra of GNa3, GRb and GK glasses, showing (a) optical window and (b) absorption in the UV-visible.

Reference: Author.

Another way to quantify transparency in the UV-Vis range is by calculating band gap energy. The Band Theory for solids (SHRIVER, D. F. ATKINS, P. W. 2008), describes the overlapping of molecular orbitals forming bands. In their fundamental state, electrons are located in the valence band and when excited, they occupy an energetically larger region called the conduction band. The energy difference between these two bands is called the band gap ( $E_g$ ). Taking the UV-vis values collected and using the Tauc method (TAUC, 1966), for allowed direct transition that correlates the absorption coefficient with energy (wavelength), band gap values can be obtained. These energy values correspond to the intersection of the tangent drawn from the absorption region with linear behavior with the abscise of the graph.

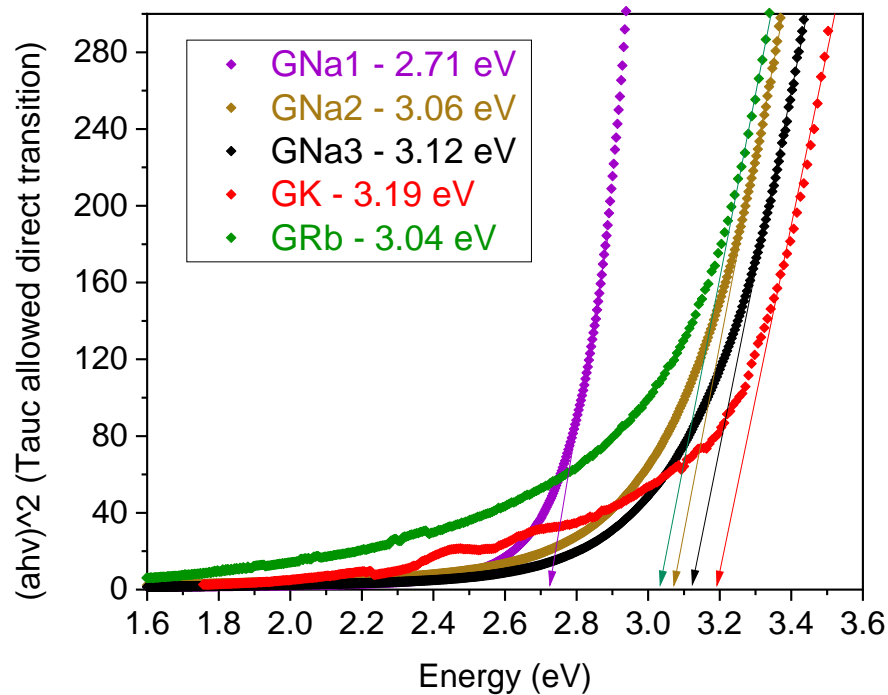


Figure 21 – Band Gap values of the glasses GNa1, GNa2, GNa3, GK and GRb.

Reference: Author.

From the absorption spectra shown in Figure 21, it appears that glass composition with 15%  $Ta_2O_5$  (GNa1) presents a smaller band gap of 2.71 eV while the others samples GNa2 and GNa3 (20%  $Ta_2O_5$ ) exhibit energy values of around 3.33 and 3.41 eV, respectively. GNa2 and GNa3 glasses seem to present similar  $E_g$

values. Commonly, in semiconductor materials, the yellow color is associated with a gap around 2.6 eV. On the other hand,  $E_g$  values higher than 3 eV correspond to colorless materials. In fact, they do not absorb light in the visible since the energy gap between the valence and conduction bands is high enough to avoid electronic transitions triggered by visible photons. Thus, any visible photon is either transmitted or reflected and not absorbed. Furthermore,  $\text{GeO}_2$  has  $E_g = 5.35$  eV (LIN, 2010), while  $\text{Ta}_2\text{O}_5$  has  $E_g = 4.0$  eV (YANG, 2014) and if these oxides are considered part of the glass matrix it is expected a transparent material for any possible molar proportion, even though, in general the  $\text{Ta}_2\text{O}_5$  addition in the glass matrix could contribute to a decrease in the value of  $E_g$  of the glass. In addition,  $\text{Ta}_2\text{O}_5$  could generate greater polarizability in the matrix (CUNHA, 2018). Therefore, considering the previous discussion, one could notice that this yellow color, one more time, could only be related to some kind of contamination once these oxides may not lead to a such reduction in energy  $E_g$  that could generate into a colorful glass material. In fact, for isolators such a glass material, the color is often associated to impurities. Those impurities could lead in a such decay for the excited electrons to achieve states within the band gap with emission of photons with lesser energy than the material band gap. Those materials appeared, then, colored depending on the incident light wavelength (CALLISTER, 2001).

Comparing the alkaline glasses GNa3, GK and GRb they seem to present close band gap values: 3.41, 3.44 and 3.30 eV, respectively. This slight difference in band gap between them does not bring much information but only confirms transparency for these materials.

## CHAPTER 4

---

### **ALKALINE TANTALUM GERMANATE GLASS CERAMICS:**

This chapter presents the experimental results and discussion about the alkaline tantalum germanate glass-ceramics obtained from the precursor glasses by heat treatments.

## 4.1 SODIUM TANTALUM GERMANATE GLASS CERAMICS

### 4.1.1 Chronological sequence of obtaining and growing of spherulites

Even though all GNa glass samples after heat treatment above  $T_g$  suffer visible changes in their aspect and transparency, in function of time and temperature, only some samples presented micrometric spherical structures at the surface observed by optical microscopy. Those glass-ceramics with spherulites were obtained after several tests, varying different settings such as molar composition and thermal treatment parameters.

In a previous investigation of our research group, such spherulites were observed after heat treatment of a glass of composition  $70\text{GeO}_2\text{-}20\text{Ta}_2\text{O}_5\text{-}10\text{Na}_2\text{O}$ . However, the glass GNa0 ( $75\text{GeO}_2\text{-}15\text{Ta}_2\text{O}_5\text{-}10\text{Na}_2\text{O}$ ) was chosen for the first crystallization tests because of its higher thermal stability and similar crystallization behavior. First heat-treatment tests were performed based on DSC curves. GNa0 bulk glasses, shown in Figure 22, were submitted to heat treatments for 24 h at 700, 720, 750, 780 and 800 °C, obtaining the glass ceramics GCNa0-T-24, where T is the temperature in °C.

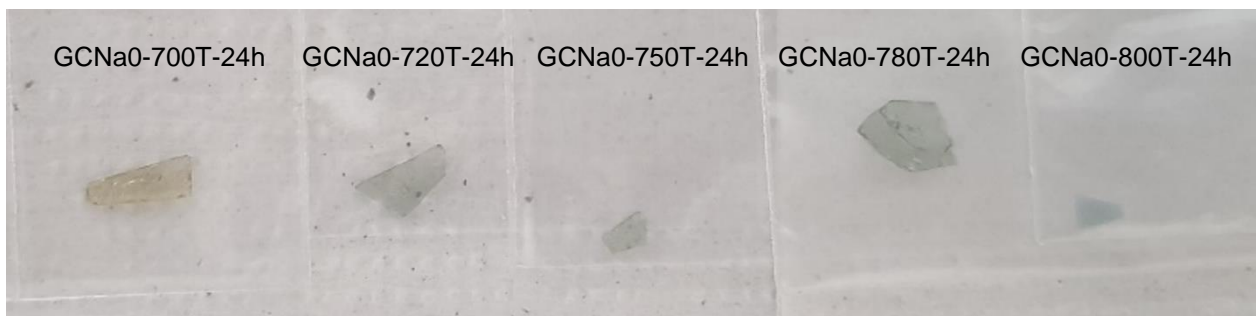


Figure 22 – GCNa0-T-24h glass ceramic bulks with 24 h under thermal treatment at 700, 720, 750 780 e 800 °C, respectively.

Reference: Author.

At 780 °C and mainly at 800 °C, after 24 h, the obtained glass ceramics exhibit an apparent crystallization process, including decrease in transparency in the visible while turning into gray/white materials. At 800 °C, the glass ceramic is completely opaque under visible light. In addition, for these samples, spherulites were not seen.



However, even if the thermal treatment on these samples were performed with a further increasing in time or temperature in order to favor any appearance of spherulites, this would not be interesting for optical applications because of the opaque character already showed.

Bulk glasses of GNa1 ( $75\text{GeO}_2\text{-}15\text{Ta}_2\text{O}_5\text{-}10\text{Na}_2\text{O}$ ) were also heat treated for 24 h at 700, 720, 750, 780 and 800 °C for glass ceramics preparation. For these, similar results as those from GNa0 were obtained but for GNa1 glasses and GCNa1 glass ceramics the yellow aspect is stronger. However, likewise GCNa0, they appeared gradually gray/white in function of the crystallization until they achieve full opaque aspect. These similar results were already expected once the only difference between the glasses GNa0 and GNa1 is the melting time at 1500 °C (TABLE 4). Finally, Figure 23 is showing the microscopy image of the glass ceramic GCNa1-800-24. Even though this sample is highly crystallized and opaque material, it did not show any sign of spherulites or any macro crystalline structure. Therefore, it is possible to suggest that spherulites formation is not favored in glasses with the molar composition  $75\text{Ge-}15\text{Ta}_2\text{O}_5\text{-}10\text{Na}_2\text{O}$ , even for highly crystallized samples.

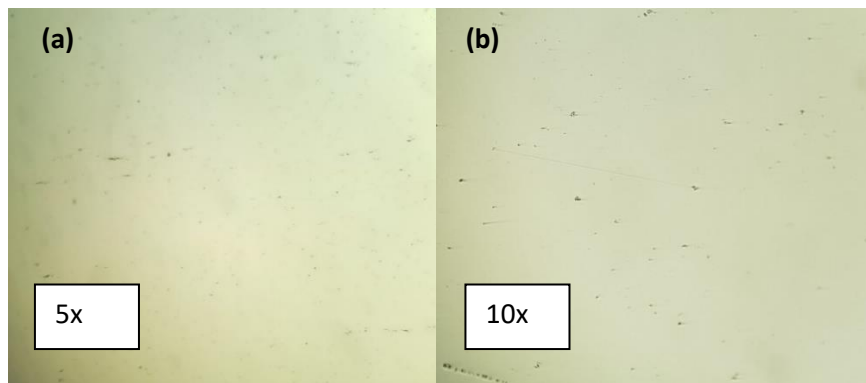


Figure 23 – Microscope images amplified in a) 5x and b) 10x of the glass ceramic 1GCNa1-800-24, which was obtained from thermal treatment of the glass GCNa1 under 800 °C for 24 h showing that spherulites were not seen in this network.

Reference: Author.

Same preliminary tests of heat treatments for 24 h at 700, 720, 750, 780 and 800 °C were performed in bulk samples GNa2 and GNa3 ( $70\text{GeO}_2\text{-}20\text{Ta}_2\text{O}_5\text{-}10\text{Na}_2\text{O}$ ). For these glass ceramics, the temperatures from 700 to 780 °C did not result in any evidence of spherulites. Figure 24 presents the visible aspect of glass sample GNa3 thermal treatment at 780 °C for different times. The transparency of the bulk progressively decreases and becomes whitish and translucent in function of time (10 min to 24 h) due to progressive crystallization of the material.

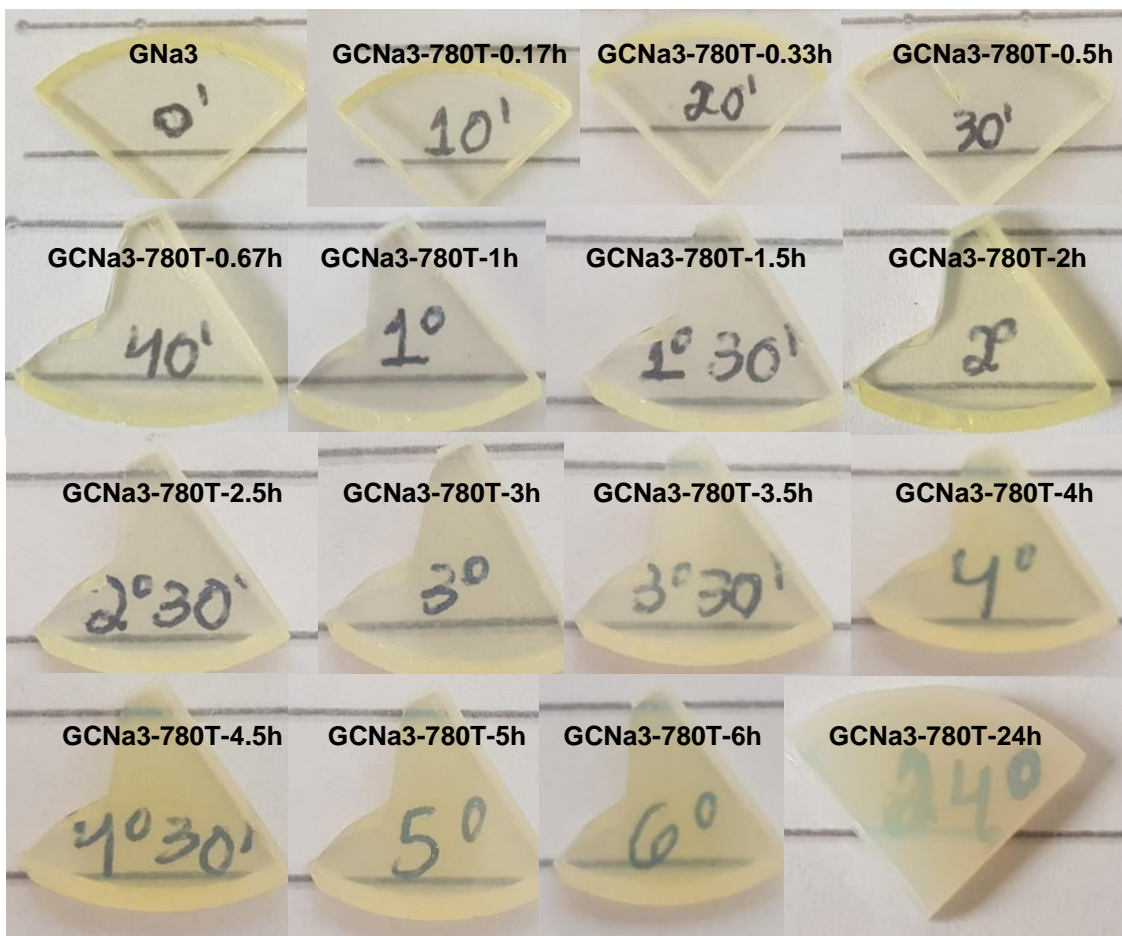


Figure 24 – GNa3 bulk glass changing progressively in to glass ceramics GNa3-780-t in function of time for a thermal treatment at 780 °C.

Reference: Author.

Finally, for both GNa2 and GNa3 glasses, having the heat treatment temperature set at 800 ° C, surface spherulites began to appear from 18 h as shown in Figure 25. Heat treatment also promote a color change of the sample when compared to precursor glasses GNa0, GNa1 and GNa3 (Figure 25b): the glass ceramic bulk present a grayish brown color aspect instead of whitish. This change in color indicates contamination probably from the crucible Pt/Au, since it was the only experimental difference during synthesis between GNa2 and GNa3. However, it seems that this contamination does not affect the evolution of spherulites.

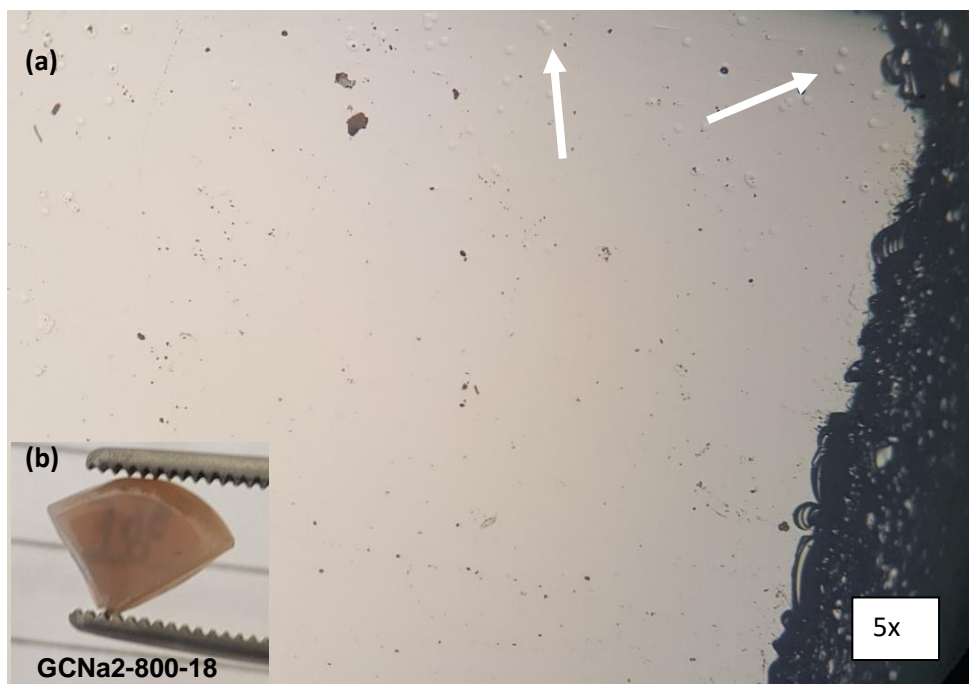


Figure 25 – Image of (b) the glass ceramic bulk from GC0.Na2-800C-18h sample and superficial visualization of the spherulites on it, indicated by the white narrows. The microscopic images had magnification of (a) 5x.

Reference: Author.

From those preliminary tests, one can notice that the best set parameter in order to form spherulites and avoid contamination is by making tantalum germanate sodium glasses with molar rate of  $70\text{GeO}_2\text{-}20\text{Ta}_2\text{O}_5\text{-}10\text{Na}_2\text{O}$  in a pure platinum crucible and with a melting time of 1 h at 1500 °C. After the glass formation, the heat treatments should start at 800 °C with a minimum of 18 h. However, those glass ceramics are showing bigger and well distributed spherulites after around 72 h as

shown by Figure 26. Precisely for this reason, this thesis frequently compares and characterizes glass ceramics at these two heat treatment conditions in most of the following studies.

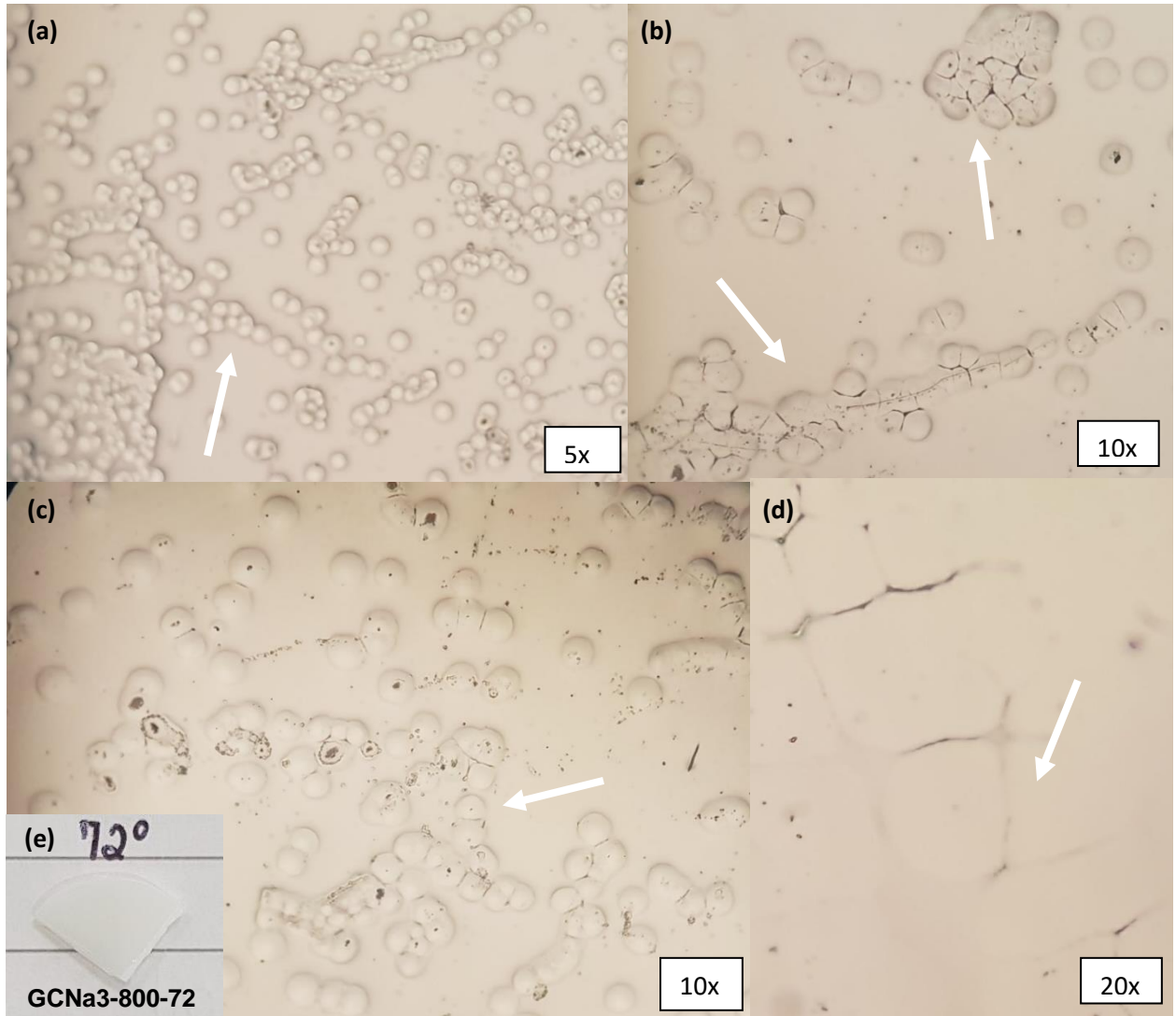


Figure 26 – Image of (e) the glass ceramic bulk from GC-Na3-800-72 sample and superficial visualization of the spherulites on it, indicated by the white arrows. The microscopic images had magnification of (a) 5x, (b) 10x, (c) 10x and (d) 20x

Reference: Author.

## 4.2 Detailed investigations in the glass ceramics GCNa3

These surface spherulites are interesting and also unexpected feature detected in some of these GCNa3 glass ceramics. Therefore, a more detailed analysis of these glass ceramic materials and investigation of their optical properties were performed as shown on the following discussions.

### 4.2.1 Thermal properties

From a general analysis of these results, one can deduce that this glass  $70\text{GeO}_2\text{-}20\text{Ta}_2\text{O}_5\text{-}10\text{Na}_2\text{O}$  is relatively stable against devitrification ( $T_{x1} - T_g = 92\text{ }^\circ\text{C}$ ), which is in agreement with glass formation obtained under relatively slow quenching conditions, but several crystalline phases can be precipitated by heat treatment above  $800\text{ }^\circ\text{C}$ . Since previous works pointed out that the increasing  $\text{Ta}_2\text{O}_5$  contents in alkaline germanate glasses promote higher crystallization tendencies (PIETRO, 2015), one could note that the low temperature crystalline phase formed by phase separation is related with a tantalum-containing compound. Since spherulite formation was not observed below  $800\text{ }^\circ\text{C}$ , increasing times ranging from 1 to 624 h at  $800\text{ }^\circ\text{C}$  were used for production of glass-ceramics as shown for some representative glass-ceramics in Table 6.

DSC curves of GNa3 glass after heat-treatments for 1, 20 and 48 hours are also resumed in Figure 27 and give a first insight of the crystallization mechanism: in fact, it appears that the low temperature phase crystallizes within the first hour since the associated exothermic signal is not clearly detected in the glass-ceramic GCNa3-800C-1h. On the other hand, the crystallization kinetics of the high temperature phase seems to be slower since the corresponding exothermic event is still present after 20 hours and apparently disappears after 48 hours. In addition, the visible and progressive loss of transparency under heat treatment (FIGURES 25-26) is suggested to be related with both progressive crystallization of the high temperature phase as well as aggregation of the low temperature phase crystallites promoted by a lower viscosity at  $800\text{ }^\circ\text{C}$  and increasing light scattering.

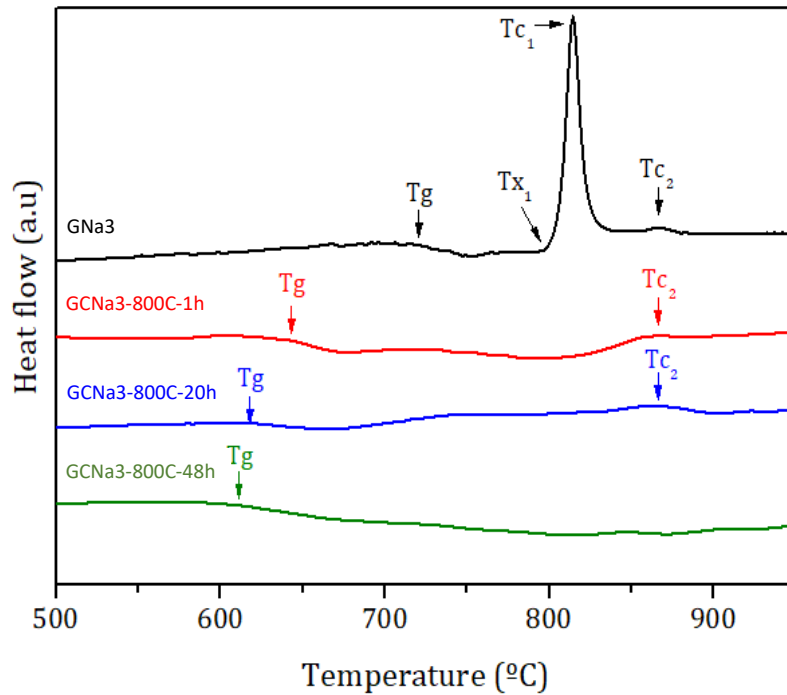


Figure 27 – DSC curves of glass sample of composition  $70\text{GeO}_2\text{-}10\text{Na}_2\text{O-}20\text{Ta}_2\text{O}_5$  and corresponding glass-ceramics after heat-treatment at 800 °C for 1 h, 20 h and 48 h.

Reference: Author

#### 4.2.2 X-ray diffraction analysis

For identification of the crystalline phases and a better understanding of the overall crystallization mechanism, X-ray diffraction measurements were performed on the pristine glass (GNa3) and glass-ceramics (GCNa3) after heat treatment times ranging from 1 hour to 624 hours as presented in Figure 28. The low temperature crystalline phase is attributed to sodium tantalate perovskite of tungsten bronze-like structure  $\text{Na}_2\text{Ta}_8\text{O}_{21}$  in agreement with the database reference JCPDS 28-1137. However, this crystallographic reference which is related with a study devoted to sodium tantalates and oxyfluorotantalates (CHAMINADE, 1972) only indexed the diffraction peaks from  $10^\circ$  to  $40^\circ$  but the diffraction positions for higher angles were not reported.

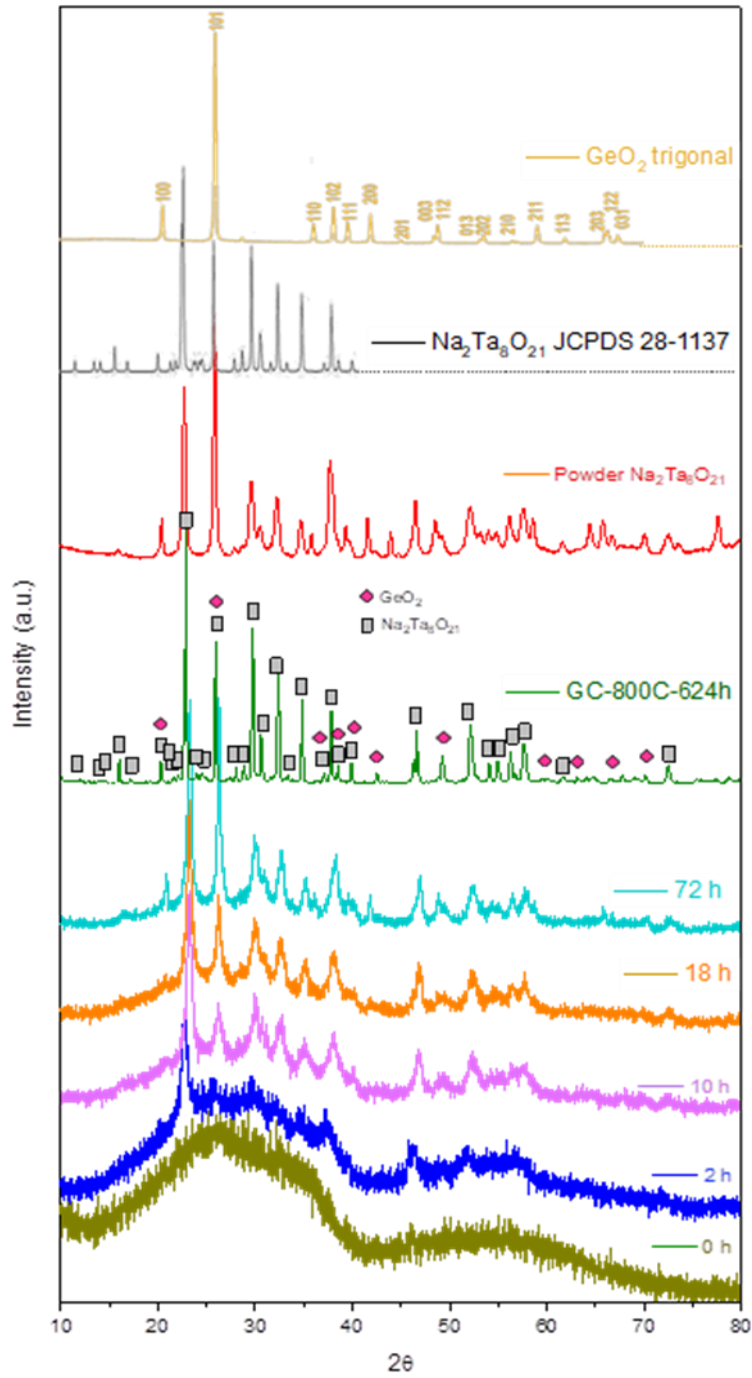


Figure 28 – X-ray diffraction patterns of the pristine glass, glass-ceramics after heat treatment for 2, 10, 18, 72 and 624 hours, synthesized  $\text{Na}_2\text{Ta}_8\text{O}_{21}$  powder and references JCPDS 28-1137 of  $\text{Na}_2\text{Ta}_8\text{O}_{21}$  and  $\text{GeO}_2$  trigonal.

Reference: Author.

In order to use a more accurate comparative diffraction pattern, crystalline powder  $\text{Na}_2\text{Ta}_8\text{O}_{21}$  was synthesized by solid state reaction of a 4:1 mixture of  $\text{Ta}_2\text{O}_5$  and  $\text{Na}_2\text{CO}_3$  grinded in an agate mortar, compacted in a tablet using a hydraulic press, heated at 800 °C in order to eliminate organic compounds and gases slowly for 9 h and then finally heat treated at 1400 °C for 24 h. As shown in Figure 28, this powder sample exhibits all the diffraction peaks of reference JCPDS 28-1137 between 10 and 40° together with other diffraction signals above 40° attributed to the same crystalline phase  $\text{Na}_2\text{Ta}_8\text{O}_{21}$ .

. The diffractograms 2 to 72 h of the Figure 28 are from the same sample powder (around 40 mg) of the glass sample GNa3, and the XRD data collected inside the equipment set at 800 °C and heating rate of 10°C.min<sup>-1</sup>. These XRD data display patterns of the orthorhombic phase  $\text{Na}_2\text{Ta}_8\text{O}_{21}$  after 2 h of heat treatment. However, since it took around 1.3 h to achieve 800 °C, the real time at such temperature is actually 40 min. Furthermore, same crystallites are expected to form for thermal treatment at around 800 °C in function of a longer period of time. In order to confirm that point, a long thermal treatment of 624 h (26 days) at 800 °C was performed and the obtained diffractogram shows similar pattern from those obtained after 2 h of thermal treatment, even more similar to 72 h, but with much higher intensity due the higher crystallinity degree, but still related to the phase  $\text{Na}_2\text{Ta}_8\text{O}_{21}$ .

Only with 2 h of thermal treatment the pattern starts to match with the file JCPDS 28-1137 and already at 5 h it matches almost perfectly. In the first moment, it is suggested that thermal treatment from those glasses GNa3 leads only to the formation of the phase  $\text{Na}_2\text{Ta}_8\text{O}_{21}$ . However, it is important to considerate that some oxide species and tantalates (SEBASTIAN, 2015; RUIZ, 2019) could show similar intervals of Bragg angles and because of that some reflections are overlapped. Therefore, it may not be possible to affirm that  $\text{Na}_2\text{Ta}_8\text{O}_{21}$  is the only phase present in these glass ceramics. Considering diffraction peaks overlap, the presence of  $\text{GeO}_2$  is also possible, having main peaks at  $2\theta = 21, 26$  and  $49^\circ$ . In fact, Raman analysis on those glass ceramic samples suggest the presence of crystalline  $\text{GeO}_2$  inside of spherulites regions (FIGURE 35) and this phase is perfectly matching to the XRD peaks at  $2\theta = 21, 22$  and  $26^\circ$  (GIRI, 2008; ZHAO, 2015; XIE, 2020) in Figure 28 and, therefore, these peaks may be coincident to the phase  $\text{Na}_2\text{Ta}_8\text{O}_{21}$ . One should note that crystallization of quartz-like  $\alpha\text{-GeO}_2$  can be nor excluded neither confirmed at this stage in these glass-ceramics because of the angle position match with sodium



tantalate. However, since DSC data also pointed out the coexistence of at least two crystalline phases for long heat-treatments, no other oxide crystalline phase containing germanium and/or sodium and/or tantalum could be identified from the X-ray diffraction patterns.


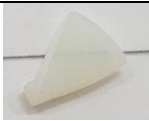


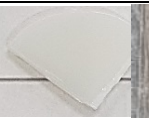


Finally, longer heat treatment times which promote a sharpening of the diffraction peaks are in agreement with the formation of nanoscale crystallites progressively growing during heat treatments (ROSS, 2019; SUN, 2002). Other studies performed on similar glass compositions where sodium was substituted by potassium detected precipitated crystallites of about 6 nm (CUNHA, 2018).

#### 4.2.3 General features

Some GCNa3 glass ceramics (made from the glass sample GNa3 - 20% Ta<sub>2</sub>O<sub>5</sub>, melting at 1500°C for 1h in pure Pt crucible) representatives are shown in Table 6, along with their respective heat treatments parameters, growing of spherulites and relative SHG intensities for comparison. In addition, for these samples further analyzes such as density, refractive index, micro and macro-Raman spectroscopy, elemental analysis with EDS and EAS and macro-SHG measurements were performed.

These glass-ceramics and their detailed spherulitic crystallization mechanisms displayed a strong interest after the evidence of second harmonic generation whose intensity depends on the crystallization conditions as resumed in Table 6 and Figure 29b for representative samples. In fact, no SHG signals could be detected in the pristine glass nor glass-ceramics until 18 h of heat treatment using the Maker fringes technique. At this point, a weak SHG response was collected in sample GC-800C-18h, which is also the sample with the lowest heat treatment time presenting surface spherulites. Other SHG measurements recorded on a sample with well-formed spherulites (GC-800C-72h) identified stronger SHG signals with order of magnitude about 10<sup>2</sup>. For the sample treated during 624 h, the SHG signal is about 10<sup>6</sup> stronger under our measurement conditions. These data highlight a need for a detailed spherulite characterization and a coherent correlation with the SHG signals.

Table 6 – GNa3 and glass ceramics GNa3-T-t samples, comparing heat treatments parameters, growing of spherulites and SHG signals.

Sample	GNa3	GNa3-790C-72h	GNa3-800C-8h	GNa3-800C-18h	GNa3-800C-72h	GNa3-800C-624h	GNa3-850C-1h
Thermal treatment (°C)	-	790	800	800	800	800	850
Heating time (h)	-	72	8	18	72	624	1
Spherulite average radius size (µm)	-	-	-	9	40	50	-
SHG relative intensity	-	-	-	Very weak (10 <sup>-5</sup> )	Weak (10 <sup>-3</sup> )	Strong (10)	-
Aspect							

Reference: Author.

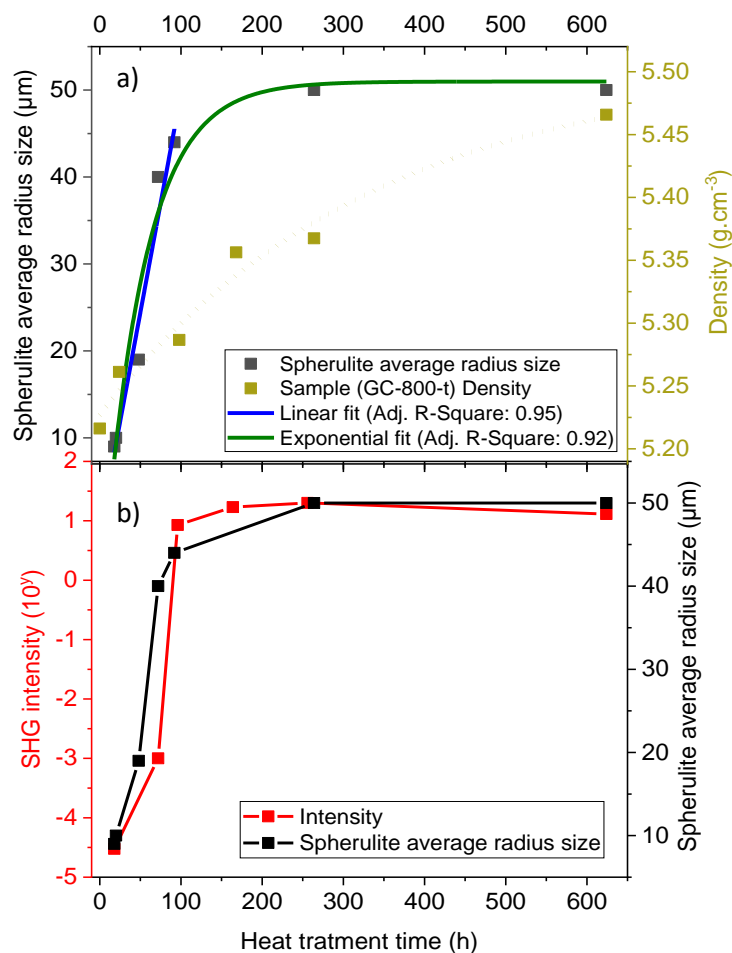


Figure 29 – Curves showing the (a) spherulite average radius size and density and (b) SHG relative intensity as a function of heat treatment time.

Reference: Author.

Overall, these samples became whiter and less transparent to visible light with the increase in heat treatment time and temperature (TABLE 6). Furthermore, density also increased (Fig. 29a). Changes in color and density are related to crystallites precipitations from the glass matrix and consequently lead a different molecular disposition and when these changes occur, those materials become glass ceramics (GUEDES, 2020, MARCONDES, 2019; ZANOTO, 2004; MUSGRAVES, 2019). Depending on glass density and composition, atoms and ions mobility occurs resulting in crystallization governed by the first step known as nucleation and the second step being growth from the nuclei (KARPUKHINA, 2014; G.P. KOTHIYAL, A. ANANTHANARAYANAN, 2017; R. CASASOLA, 2012; K. THIEME, C. RUSSEL, 2014; ZANOTO, 2004; MUSGRAVES, 2019) However, only some samples, as seen for Table 6 and Figure 29b, are showing the further spherulitic organization under heat treatment, leading to SHG signals.

Based on several heat treatment tests, one could deduce that spherulitic structures could not be obtained under 790 °C for at least 72 h of thermal treatment, independently of the crystallization of sodium tantalate  $\text{Na}_2\text{Ta}_8\text{O}_{21}$  (TABLE 6). On the other hand, higher temperatures as 850 °C promotes a fast crystallization of the material already after 1 h of heat treatment, however, without the appearance of any spherulites but with high opacity (TABLE 6). This result collaborates with the proposal that the phase formed by phase separation which leads to spherulites formation is related with a tantalum-containing compound at low temperature, given by long heat treatments as shown in the DSC curves in Figure 27, once  $\text{Ta}_2\text{O}_5$  promotes higher crystallization tendencies. Therefore, temperatures above  $T_c$  create a fast crystallite precipitation and growing which do not favor the mechanism in which the gathering of the crystals create spherulites.

Initially, the spherulites appear at the corners (FIGURE 30a1, b1) and defects (FIGURE 30a2, b2). However, with the time they spread all over the surface, along with a spherulite radius increase (FIGURE 30a3, b3, c1-c3). Spherulites are seen after 18 h under heat treatment at 800 °C with 9  $\mu\text{m}$  of average radius size and they keep growing linearly rather than exponentially as showing by the fit curves in Figure 28a and then stabilize at around 50  $\mu\text{m}$ . Indeed, spherulites features, usually, present a linear radius grow for constant temperatures (VARGA, 1992) until their growth is stopped by impingement with neighboring spherulites with formation of polyhedral structures as highlighted in Figure 30c1, c3 (LIU, 2001)

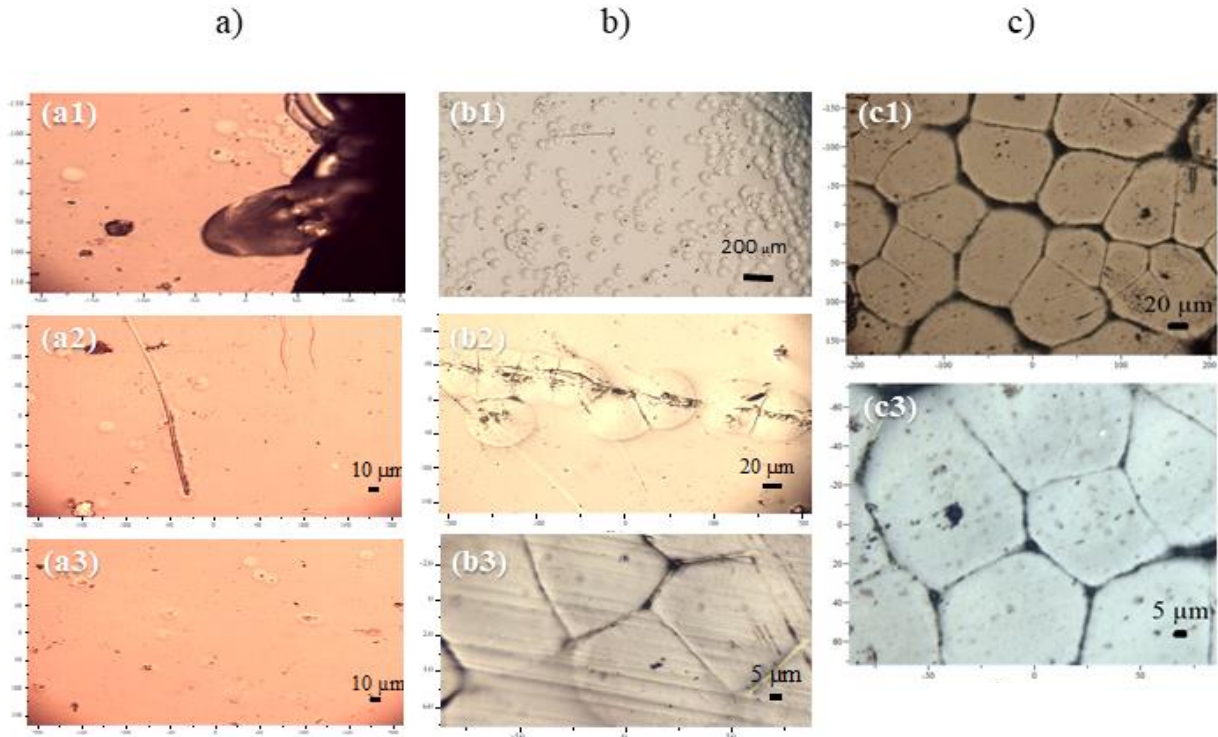


Figure 30 – Optical microscope images of the glass ceramics a) GC-800C-18h, b) GC-800C-72h and c) GC-800C-624h, showing the spherulites growth.

Reference: Author.

It is also suggested that they are originated by fibrillar crystals in the center, where the “nucleation” was started, and its shape gives the lowest surface energy compared with equivalent planar figures, justifying then they appearing and growth (VARGA, 1992). Therefore, spherulites with the same radius size seems to nucleated simultaneously (VARGA, 1992; RAIMO, 2015; KARASAWA, 1998). Finally, one can notice that the spherical growth occurs until spherulites come into contact after which a coalescence process with well-defined boundaries is observed according to the Figure 29b, c. Furthermore, while they keep growing even after 264 h of heat treatment its linear radius growth could be affected by the surroundings and precisely because of that it may coexist different spherulites size and shape in the same sample (RAIMO, 2015; KARASAWA, 1998).

Furthermore, GNa3 glass and GNa3-800-t glass ceramics were investigated by the method buoyancy, giving the correlation of the Figure 28a in function of heat treatment. Overall, density of the samples increases with heat time (FIGURE 29a). The glass presents a high density of  $5.21 \text{ g/cm}^3$ , in agreement with the relatively high

atomic mass of the main element Ta and Ge. The density increases until 624 h and gives a value of  $5.46 \text{ g/cm}^3$ . This density growth is foreseen and related to the better atomic arrangement due to crystallization (MUSGRAVES, 2019; MARCONDES, 2019). For the same composition, it is expected that the stable crystalline phase has a lower free energy and then higher density than a metastable glassy phase (KARAMANOY, 1999).

#### 4.2.4 UV-Vis-IR absorption spectroscopy

Absorption spectroscopy in the UV-Vis show that the glass ceramics presented a progressive transparence loss with the heat treatment as shown in Figure 31. For the samples GNa3-800T-18h, GNa3-800T-48h, GNa3-800T-72h the optical windows ranges between  $0.65$  and  $5.5 \mu\text{m}$ ,  $0.70$  and  $6 \mu\text{m}$  and  $0.78$  and  $6 \mu\text{m}$ , respectively, while GNa3 glass sample from  $0.5$  and  $5.5 \mu\text{m}$ .

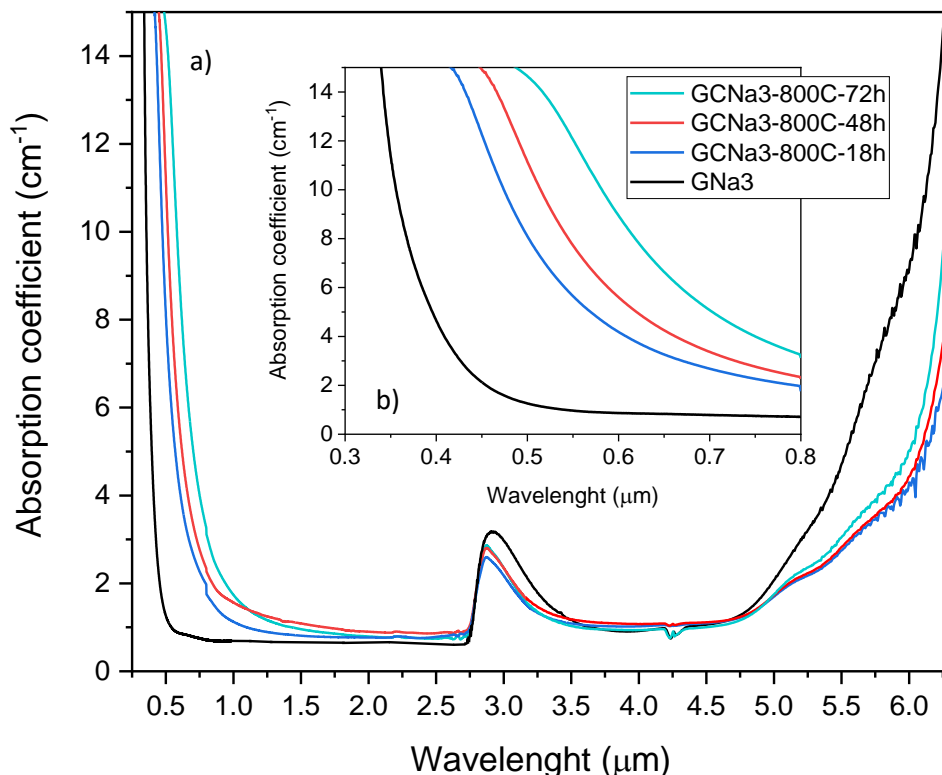


Figure 31 – Spectra of GNa3 glass and GNa3-800-t glass ceramics, showing (a) optical window and (b) absorption in the UV-visible.

Reference: Author.

This behavior is expected once with the crystallization and growth of crystalline structures such as spherulites the light dispersion increases considerably, turning the samples into opaque material. On the other hand, the infrared region shows a slight transparency gain. Since crystallization process produces modifications of the glass matrix structure, a change of vibrational modes of the material is expected.

#### 4.2.5 Elemental analysis by EDS and AES

For a better understanding of the spherulite formation, structure and composition, elemental analyzes were also performed by EDS (Energy Dispersive X-ray Spectroscopy) and AES (Auger electron Spectroscopy) in the samples GC-800C-18h and GC-800C-72h. For both EDS and AES analysis (TABLES 7 and 8 and FIGURES 32 and 33), characterizations were performed on a slight polished surface in order to eliminate any glass boundaries and also to enable these equipment during running time to achieve spherulites center areas. Therefore, these analyzes are expected to present accurate elementary results of composition inside and outside of the spherulites. Results obtained on sample GC-800C-18h are related with spherulites in their early formation stage whereas sample GC-800C-72h contains well-formed and grown spherulites.

EDS points out that the relative Ta content increases inside the spherulites and, on the other hand, Ge decreases (TABLE 7 and FIGURE 32). In other words, it is pointed out that spherulite formation is spatially correlated with a higher tantalum and lower germanium content than the surrounding (outside area). This observation is even more evident for bigger spherulites as shown in GC-800C-72 h for which inside areas contains around is found around 26 atom. % of Ta against 18 % from outside areas while Ge content varies from 3% to 10%.

Table 7 – EDS quantitative results inside (001) and outside (002) of the spherulite in samples GC-800C-18h and GC-800C-72h. The oxygen concentrations were calculated using the oxide forms  $\text{Na}_2\text{O}$ ,  $\text{GeO}_2$  and  $\text{Ta}_2\text{O}_5$ .

Sample	GC-800C-18h (FIGURE 31a)		GC-800C-72h (FIGURE 31b)		
	Error $\pm 1\%$ atom.		Error $\pm 1\%$ atom.		
Point	001	002	001	002	
Element	Na (% atom.)	1.5	0.8	0.6	1.2
	Ge (% atom.)	7.6	10.2	3.2	10.3
	Ta (% atom.)	21.4	19.2	26.3	18.6
	O (% atom.)	69.5	68.7	72.5	67.8

Reference: Author.

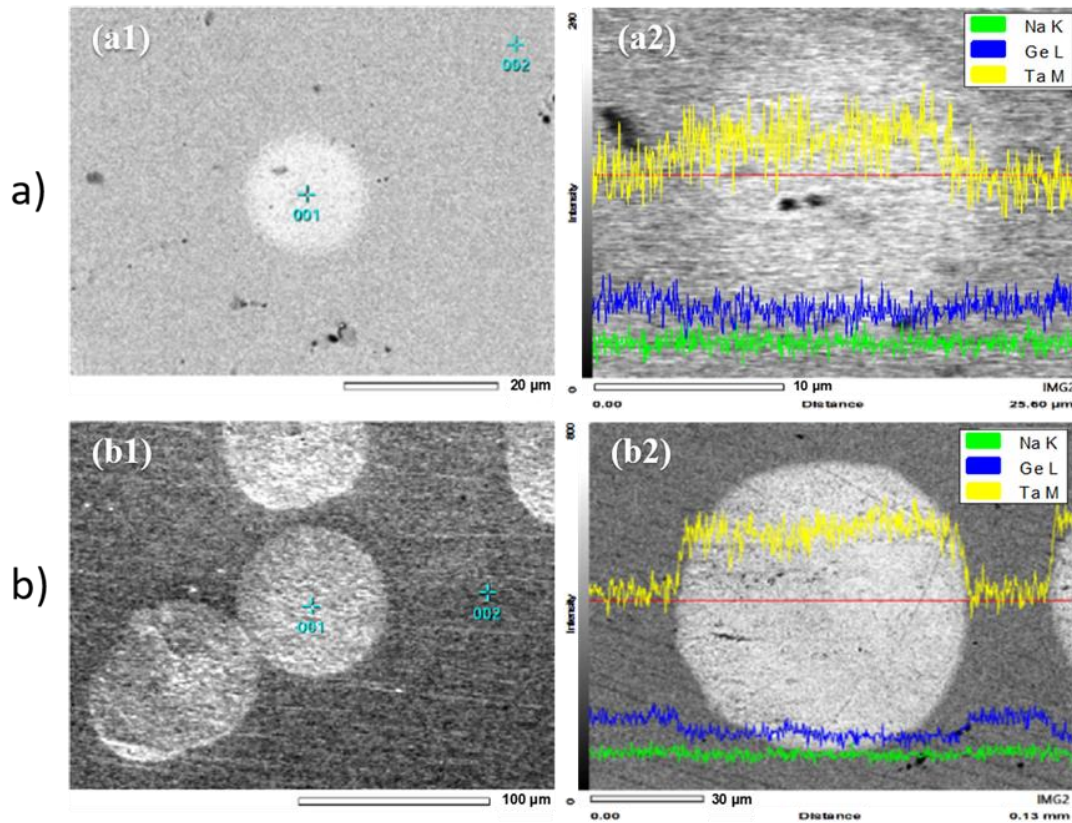


Figure 32 – SEM micrographs on backscattering electrons mode of the samples (a) GC-800C-18h and (b) GC-800C-72h, respectively, where a1 and b1 present the chosen points for EDS elemental analyzes showed in Table 7. Finally, a2 and b2 are showing the line path chosen (in red) where EDS analysis was performed and their intensity profiles for Ta, Ge and Na.

Reference: Author.

Quantitative data concerning sodium were considered constant along the whole surface within the experimental error. These quantitative analyzes are a first indication that spherulite formation is in some extent related with a phase separation between a tantalum-rich and germanium-rich phase. Another important point concerning spherulite droplet-like formation is related with their crystalline and/or amorphous nature. Whereas several reports attributed spherulites to monocrystals, other works identified that spherulitic structures are only partially crystalline and formed from fibrillar crystals grown from a nucleus embedded in a glassy-like phase (FREIMAN, 1971; CARPENTER, 1986). Some works even attributed the structure of spherulites to “anti-glass” networks (BERTRAND, 2015). In our case, the spherulites cannot be attributed to single crystals of sodium tantalate because of the still high germanium content detected by EDS (spatial resolution of 1  $\mu\text{m}^3$ ). At this stage of the discussion, it seems that germanium oxide in the spherulites can be present both as a glassy phase (probably still containing sodium modifiers and tantalum intermediates) or as a crystalline phase  $\alpha\text{-GeO}_2$ .

Even though EDS analysis could not present any oxygen measurement, it gives important information about Ge and Ta tendencies as shown in the micrographs of the Figure 32a2, b2. Overlaid on these micrographs are also shown the red lines chosen path along whose EDS measurements were performed giving its elemental content curves of Ta, Ge and Na overlaid on the images as well.

Once EDS could not bring further information about oxygen tendency, AES analyzes were also performed on both GC-800C-18h and GC-800C-72h samples to probe relative elemental analysis of both Ta, Ge and O as detailed in Figure 33, which is showing these respective micrographs along with overlaid intensities mappings for these elements. One can notice once again and with an even better contrast higher amount of Ta and lower contents of Ge in areas that correspond to the spherulites. For GC-800C-18h, this inside amount of Ge is not much different from outside areas, only Ta increases considerably while O seems to have higher intensity for outside areas. On the other hand, sample GC-800C-72h exhibits much stronger variations in elemental relative contents for Ta and Ge as already detected by EDS. For oxygen mapping, the slightly higher content outside of the spherulites apparently remains.



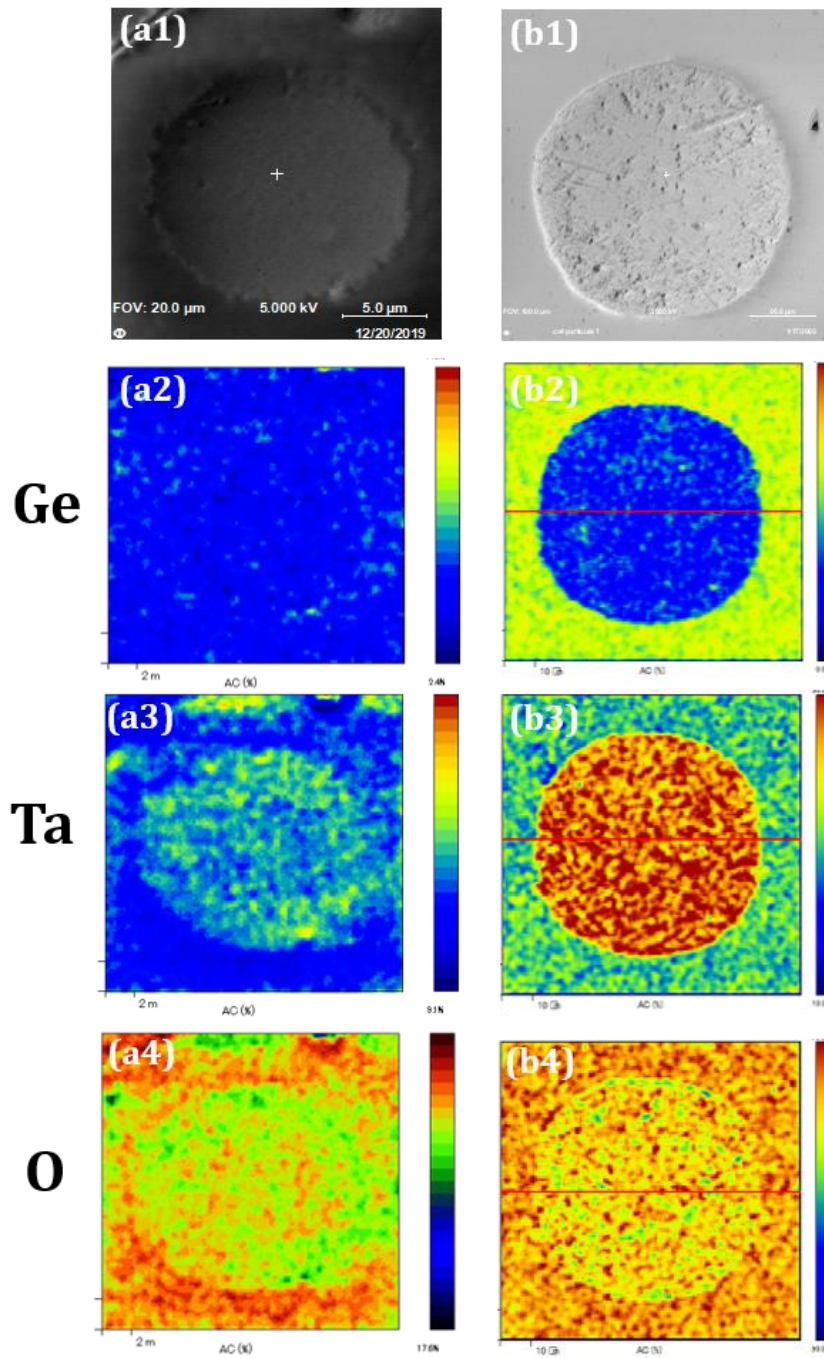


Figure 33 – a1) secondary electron image of a random spherulite in the sample GC-800C-18h, analyzed by AES, where a2,3,4) are elemental mappings for Ta, Ge and O, respectively. b1) secondary electron image of a random spherulite in GC-800C-72h, analyzed by AES, where b2,3,4) are elemental mappings for Ta, Ge and O, respectively.

Reference: Author.

Quantitative results for Ta and Ge are in agreement with EDS data concerning a progressive higher tantalum and lower germanium content inside the spherulites when compared to the outside surrounding area. This behavior is in agreement with a phase separation mechanism with spherulites formed from richer tantalum and poorer germanium contents. In other words, the spherulite formation can be understood by a microscale migration of tantalum in spherical areas whereas germanium follows an opposite trend. However, one should note that a classical amorphous phase separation cannot fully describe the spherulite formation since this event is taking place in an already formed glass-ceramic containing  $\text{Na}_2\text{Ta}_8\text{O}_{21}$  crystallites. On the other hand, relative oxygen quantification follows a quite unexpected trend since the oxygen seems to be slightly lower in the spherulites. Another correlated information is that germanium contrast is not detected during the formation of spherulites (FIGURE 33a2) but only for longer heat treatments (FIGURE 33b2).

Based on these elemental analyses, one could infer that long heat treatments above the glass transition temperature promote the diffusion of tantalum species (from crystalline  $\text{Na}_2\text{Ta}_8\text{O}_{21}$  and/or from the remaining glassy phase) and their concentration in localized spherical areas (spherulites). This tantalum diffusion induces in a second step the opposite diffusion of germanate species out of these spherulites.

#### 4.2.6 Correlated SHG and Raman microscopies

Correlative Raman and SHG microscopies were performed on the samples GC-800C-18h and GC-800C-72h. The micrographs of the Figure 33a1, b1 show the spherulites where these analyses were performed for these both samples, respectively. In addition, detailed resulting mappings for these samples are shown in Tables 8 and 9. These mappings were created by the summing of each spectrum or SHG intensity obtained for areas of  $1\ \mu\text{m} \times 1\ \mu\text{m}$ . For Raman measurements the incident laser operating was 532 nm with VV or VH polarizations, alongside with sample rotations and setting the objective lens at 100x. Using the LabSpec software, it was possible to perform a detailed survey on the whole Raman spectrum from 50 to  $1750\ \text{cm}^{-1}$  in order to find any patterns. For GC-800C-18h, only 3 new sharp Raman signals at 120, 165 and  $440\ \text{cm}^{-1}$  gave pattern profiles and these are appearing only

inside the spherulites and their respective Raman mappings are detailed in Table 8. For GC-800C-72h, 6 new sharp Raman modes are identified at 120, 165, 250, 440, 513 and 880  $\text{cm}^{-1}$  and their respective Raman mappings presented in Table 9. On the other hand, micro-SHG analyses were performed with a picosecond pulsed laser at 1064 nm also with VV and VH polarizations, sample rotations and setting the objective lens at 100x. Their mapping profiles are compared with Raman mappings also in the Tables 8 and 9.

The spherulites in the micrographs of the Figure 34a1,b1 are correlated to  $\mu$ -Raman mappings in Figure 34a2-b2, both with integrated polarization VV (parallel) and taking the Raman peak at 440  $\text{cm}^{-1}$  (the most intense Raman band). From general analyses, one should notice that for small spherulites as those in GC-800C-18h, the higher Raman mode intensity at 440  $\text{cm}^{-1}$  is concentrated in center regions and according to its growth under longer heat treatments, these peaks spread over the border areas, resulting in a map with a certain symmetry aspect as shown in Figure 33b2. By comparing the evolution of the spherulites in these samples one should notice that crystals modes active in Raman are expanding toward the borders while spherulites keep growing. This mapping arrangement, for better visualization, was divided in 3 main regions as seen in Figure 34a2,b2. The region 1 is showing areas in yellow corresponding the highest signal intensities at 440  $\text{cm}^{-1}$ , which means a higher concentration of crystallites responsible of these sharp Raman signals and/or specific local orientation. As for the region 2, areas in red indicate that this Raman signal is present but with lower average intensity. Region 3 represents the outside area of the spherulites where these Raman signals at 440  $\text{cm}^{-1}$  are not detected.

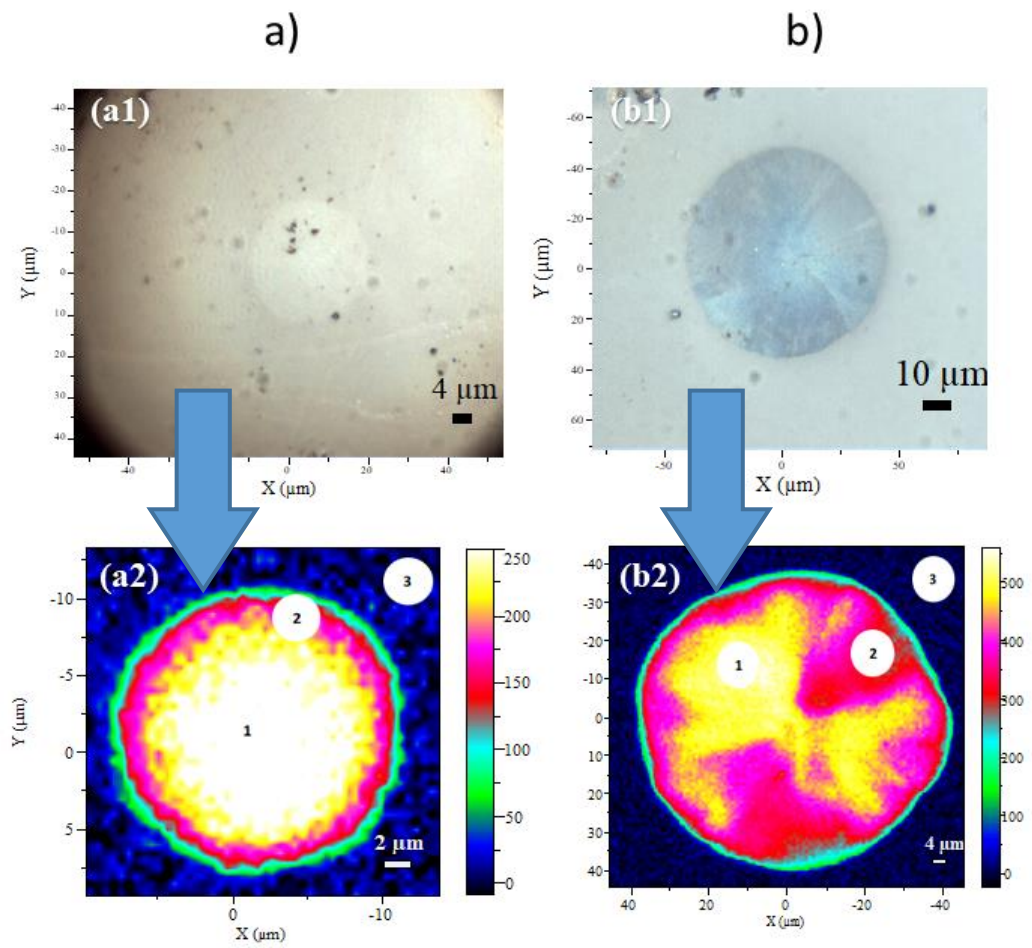
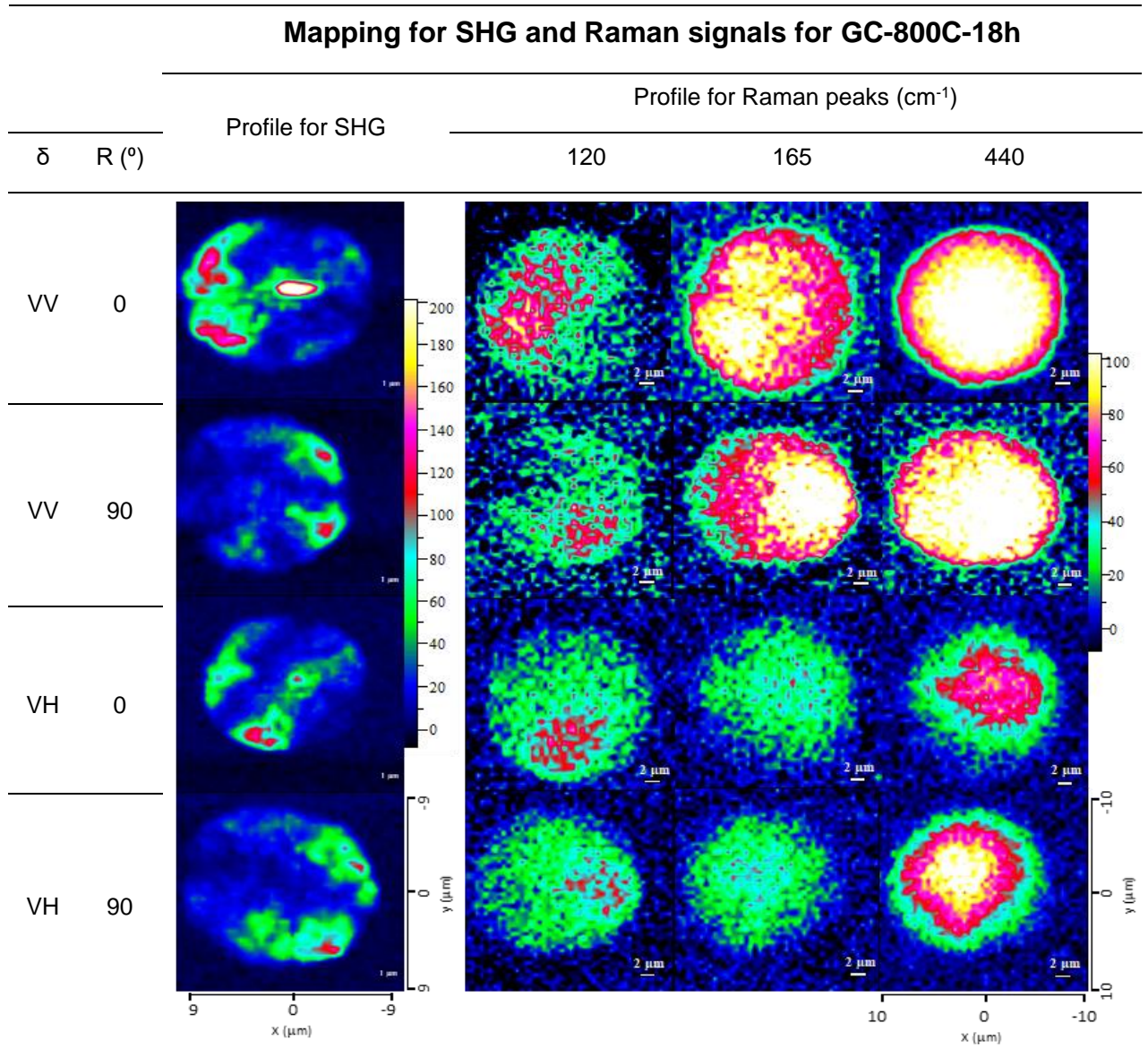


Figure 34 – Micrographics (a1, b1) and respective  $\mu$ -Raman mappings (a2, b2) showing spherulites and glass ceramic regions from the samples a) GC-800C-18h and b) GC-800C-72h, both with polarization VV and taking the Raman peak at  $440\text{ cm}^{-1}$

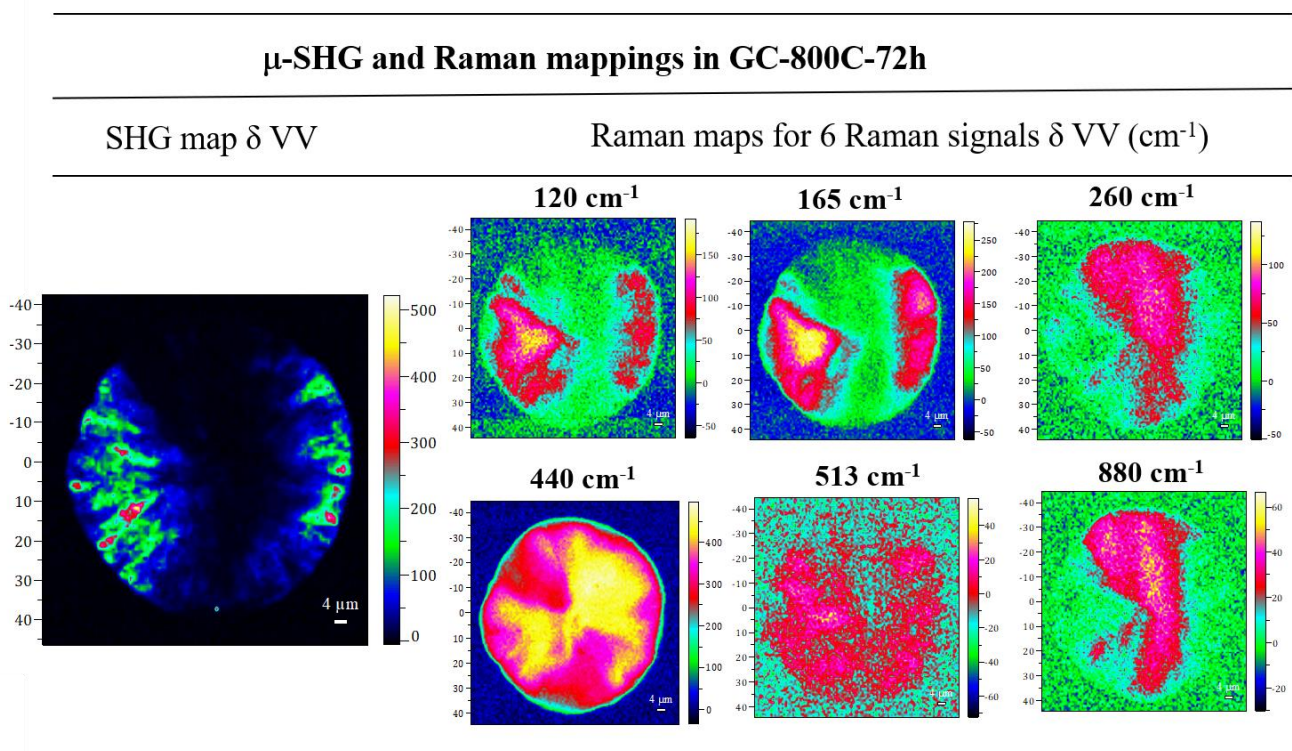
Reference: Author.

Table 8 – SHG and Raman mapping of the spherulite from the sample GC-800C-18h in Figure 34. It shows different incident linear polarization ( $\delta$ ) Vertical-Vertical (VV) and Vertical-Horizontal (VH) and sample counterclockwise rotation (R) of  $0^\circ$  (no rotation) or  $90^\circ$  for the same spherulite area.



Reference: Author.

Table 9 –  $\mu$ -SHG and  $\mu$ -Raman mappings of a spherulite in sample GC-800C-72h under VV linear polarization ( $\delta$ ).



Reference: Author.

A detailed description of Raman spectra extracted from 2D Raman mappings inside and outside of the spherulites for both samples are shown in Figure 34 and compared with quartz-like  $\alpha$ - $\text{GeO}_2$  and crystalline  $\text{Na}_2\text{Ta}_8\text{O}_{21}$ . For quartz-like  $\text{GeO}_2$ , Raman bands attribution is well-known showing main active modes are at around 120, 165, 210, 262, 320, 444 and 880  $\text{cm}^{-1}$  (TSUTOMU, 1998; GIRI, 2012; TRUKHIN, 2005; MERNAGH, 1997; MADON, 1991; MICOULAUT, 2006). The intense mode at 444  $\text{cm}^{-1}$  is attributed to bond rocking of Ge–O–Ge in bridging bonds in  $\text{GeO}_4$  tetrahedra. One can notice that in comparison with the regions 1 and 2 in the Figure 34, the main active Raman crystalline phase found inside of the spherulites is due quartz-like  $\alpha$ - $\text{GeO}_2$ . Therefore, this progressive concentration and/or orientation, in function of heat treatment, from central to peripheral areas is related to  $\alpha$ - $\text{GeO}_2$  crystals. Furthermore, this peak at 444  $\text{cm}^{-1}$  is commonly associated to those at around 85, 121, 165, 210 and 262  $\text{cm}^{-1}$ , mainly related to the translation and rotation of  $\text{GeO}_4$  tetrahedra (TRUKHIN, 2005; MERNAGH, 1997; YANG, 2007; ATUCHIN, 2009; HENDERSON, 1991; CHIASERA, 2013). However, the slightly shift in the literature band from 441 (showed for the  $\text{GeO}_2$  trigonal reference) to 444  $\text{cm}^{-1}$  is due

to the symmetric Ge-O-Ge stretching (ATUCHIN, 2009; HENDERSON, 1991; CHIASERA, 2013). Finally, the mode at  $882\text{ cm}^{-1}$  is also associated to Ge-O stretching motion with units of tetrahedral  $\text{GeO}_4$ , with 3 bridging oxygens and 1 non bridging (ATUCHIN, 2009; HENDERSON, 1991). For this structure, the germanium atoms are located at the center of corner-shared  $\text{GeO}_4$  tetrahedra, resulting in the following irreducible representation of optical vibrations:  $G=4A_1+4A_2+8E$  with  $A_1$  modes being Raman active,  $A_2$  modes IR active and E modes both Raman and IR active. Hence, degenerated E modes may also split in TO and LO modes (MERNAGH, 1997). Table 10 gives a detailed attribution of the detected Raman bands of  $\alpha\text{-GeO}_2$ .

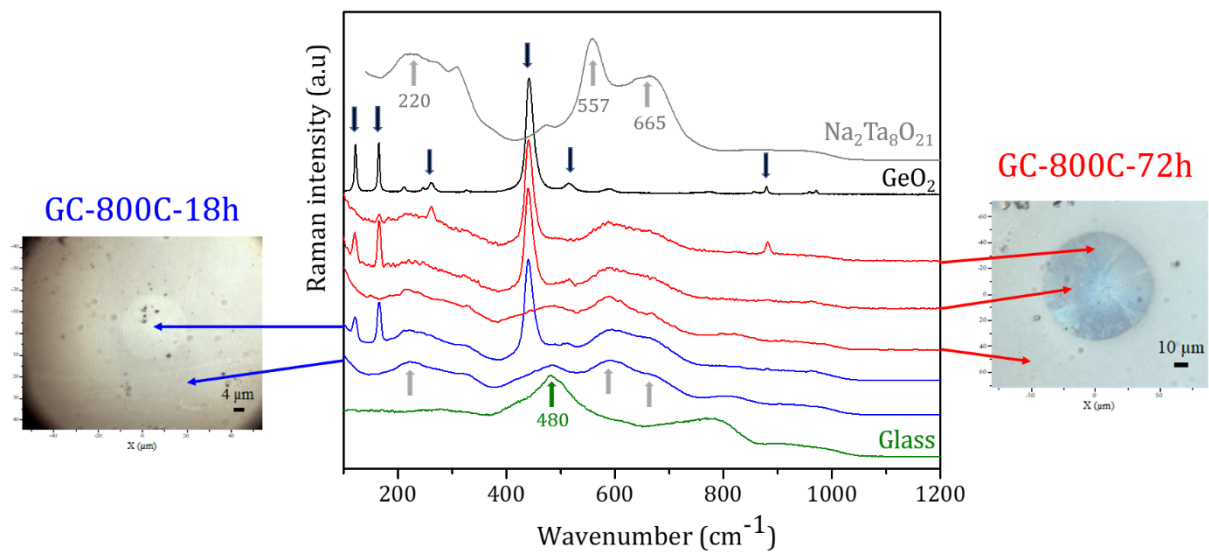


Figure 35 – Raman spectra of crystalline references  $\text{Na}_2\text{Ta}_8\text{O}_{21}$ ,  $\alpha\text{-GeO}_2$ , pristine glass and representative Raman spectra collected inside and outside of the spherulites for the samples GC-800C-18h and GC-800C-72h (FIGURE 34).

Reference: Author.

Table 10 – Attribution of the experimental Raman signals of  $\alpha$ -GeO<sub>2</sub>.

Raman signal	Representation	Attribution
123 cm <sup>-1</sup>	E (TO+LO)	Translations and rotations of GeO <sub>4</sub>
166 cm <sup>-1</sup>	E (TO+LO)	Translations and rotations of GeO <sub>4</sub>
263 cm <sup>-1</sup>	A <sub>1</sub>	Ge-O bending modes
444 cm <sup>-1</sup>	A <sub>1</sub>	Symmetric Ge-O-Ge stretching mode
516 cm <sup>-1</sup>	E (LO)	Ge—Ge stretching motions
881 cm <sup>-1</sup>	A <sub>1</sub>	Ge-O stretching motions in GeO <sub>4</sub>

Reference: Author.

A careful analysis of the Raman spectrum for Na<sub>2</sub>Ta<sub>8</sub>O<sub>21</sub> is also needed for a better understanding of the glass-ceramics structural behavior. This Raman spectrum has never been reported for this sodium tantalate phase but XRD studies elucidated structural peculiarities of this perovskite phase (CHAMINADE, 1972). Its crystalline structure is similar to tetragonal tungsten bronze K<sub>0.6</sub>WO<sub>3</sub> but additional weak diffraction peaks are in agreement with the existence of a superstructure and tripling of parameter *b*. The crystalline network is built from corner-shared TaO<sub>6</sub> octahedra in a way that free-space cavities are also formed between this octahedral framework being larger cavities labeled A<sub>1</sub> and A<sub>2</sub> of coordination 12 and 15 and smaller B cavities of coordination 9. A<sub>1</sub> and A<sub>2</sub> cavities are located one above the other along the *c* axis forming tunnels where large cations like sodium or potassium can be accommodated. According to tungsten bronzes structures, the general compound formula should be (A<sub>1</sub>)<sub>2</sub>(A<sub>2</sub>)<sub>4</sub>B<sub>4</sub>M<sub>10</sub>O<sub>30</sub> but the tripling of parameter *b* implies a corrected formula being (A<sub>1</sub>)<sub>6</sub>(A<sub>2</sub>)<sub>12</sub>B<sub>12</sub>M<sub>30</sub>O<sub>90</sub>. However, density measurements of 7.56±0.03 give for the orthorhombic cell the statistical formula: Na<sub>9</sub>Ta<sub>36</sub>O<sub>94.5</sub>, justifying the hypothesis that 6 sodium are found in A<sub>1</sub> cavities and the exceeding 3 sodium, 6 tantalum and 4.5 oxygens atoms in the A<sub>2</sub> cavities where Ta and O form linear (Ta<sub>4</sub>O<sub>3</sub>)<sub>n</sub> chains inserted inside the A<sub>2</sub> tunnels along the *c* axis (CHAMINADE, 1972). Thus, the overall formula can be represented by: Na<sub>6</sub>[Na<sub>3</sub>(Ta<sub>4</sub>O<sub>3</sub>)<sub>3/2</sub>]Ta<sub>30</sub>O<sub>90</sub>. As a consequence, two completely different Ta-O bonds are identified in Na<sub>2</sub>Ta<sub>8</sub>O<sub>21</sub>: Ta-O bonds from the corner-shared TaO<sub>6</sub> framework and Ta-O bonds from the linear chains Ta<sub>4</sub>O<sub>3</sub> inside the A<sub>2</sub> tunnels. Based on these considerations, it is suggested that the Raman signal at lower frequency (557 cm<sup>-1</sup>) is related with Ta-O-Ta stretching from the TaO<sub>6</sub> skeleton whereas the high frequency signal at 665 cm<sup>-1</sup> is



due to Ta-O-Ta stretching of the linear chains in  $A_2$  tunnels (grey arrows in Figure 35). For the glass-ceramics, intense and sharp Raman modes are progressively identified inside the spherulites as detailed in Figure 35 by the black arrows. Although only three modes centered at 120, 165 and 440  $\text{cm}^{-1}$  are detected in sample GC-800C-18h, other Raman modes are also identified at 260, 513 and 880  $\text{cm}^{-1}$  in sample GC800C-72h. Two Raman spectra of the inside zone are presented for this last sample since it has been observed that some modes are excludent i.e. modes at 120 and 165  $\text{cm}^{-1}$  are only observed in spherulite internal areas where complementary modes at 260 and 880  $\text{cm}^{-1}$  are not present. This behavior is better seen in Tables 8 and 9 where the Raman mappings of these four modes clearly fill complementary areas inside the spherulite. By comparing these spherulite sharp Raman modes with crystalline references, all these signals are undoubtedly related with trigonal (hexagonal) quartz-like  $\alpha\text{-GeO}_2$  as previously suspected by XRD analysis (MADON, 1991; MERNAGH, 1997).

Based on these results, it also appears that crystalline  $\alpha\text{-GeO}_2$  is formed only inside the spherulites for longer heat-treatments (at least 18 hours) and as a consequence, is suspected to be at the origin of the SHG signals. In fact, high distortion of the intratetrahedral O-Ge-O angle gives rise to piezoelectric and electro-optic effects much stronger than in  $\alpha\text{-SiO}_2$  as well as second order non-linear properties (KAWAMURA, 2014).

Futhermore, a detailed analysis of Raman spectra in Figure 35 for the pristine glass and glass-ceramics inside and outside the spherulites also bring a reasonable overview the overall crystallization mechanisms and spherulite formation: the main Raman feature at 480  $\text{cm}^{-1}$  (green arrow in Figure 35) in the untreated glass and related to symmetric stretchings of Ge-O-Ge bridging bonds in three-member rings is still observed in the glass ceramics out of the spherulites but with lower comparative intensity since stronger Raman signals appear at 580 and 665  $\text{cm}^{-1}$ . These bands are ascribed to the Raman signatures of  $\text{Na}_2\text{Ta}_8\text{O}_{21}$  with the frequency shift of Ta-O stretchings in  $\text{TaO}_6$  from 557  $\text{cm}^{-1}$  in pure  $\text{Na}_2\text{Ta}_8\text{O}_{21}$  to 580  $\text{cm}^{-1}$  in the glass-ceramics being related with the germanate neighborhood of these tantalate structures. The other signal is not affected by the germanate surrounding since the  $\text{Ta}_4\text{O}_3$  chains are shielded inside the  $A_2$  tunnels. Anyway, both these sodium tantalate signals are detected inside and outside of the spherulites, suggesting that

both areas contain  $\text{Na}_2\text{Ta}_8\text{O}_{21}$  crystallites. In addition, since the  $480\text{ cm}^{-1}$  signal ascribed to vitreous germanate network is detected only out of the spherulites, one could infer that the vitreous germanate network has been disrupted inside the spherulites. In this model, it is suggested that the glass-ceramic material out of the spherulites is constituted of a glassy sodium tantalum-germanate phase with embedded  $\text{Na}_2\text{Ta}_8\text{O}_{21}$  nanocrystals whereas the spherulites are mainly constituted of a comparatively higher content of  $\text{Na}_2\text{Ta}_8\text{O}_{21}$  crystallites together with crystals of quartz-like  $\alpha\text{-GeO}_2$ .

In addition, identification of broad Raman signals in the ranges  $150\text{-}360\text{ cm}^{-1}$  and  $500\text{-}850\text{ cm}^{-1}$  also suggest a residual glassy phase, even if our data are not fully conclusive for such statement. Since tantalum content is higher and germanium content lower in the spherulite when compared to the surrounding, a first reliable hypothesis is that sodium and tantalum which were initially homogeneously distributed throughout the glass volume migrate toward specific areas next to the surface and aggregate to larger crystallites. In these regions, such progressive growth of sodium tantalate crystallites partially depolymerizes the germanate covalent network and promote short germanate chains which are the basic units for growth of fibrillar  $\alpha\text{-GeO}_2$  crystals forming the spherulites. Such model is consistent with the long heat-treatment times required for spherulites formation triggered by low atomic diffusion rates in such high viscosity conditions.

Another interesting analysis that could be extracted from these Tables 8 and 9 is that the  $A_1$  Raman mode at  $440\text{ cm}^{-1}$  is detected in all the spherulite area in both samples whereas degenerated E modes at  $120$  and  $165\text{ cm}^{-1}$  spread to border areas for longer heat treatments. Hence, as better seen in sample GC-800C-72h (Table 9), SHG signals seem to be spatially correlated with areas where E Raman modes are detected with higher intensity. Those modes are observed for perpendicular electric fields to the trigonal c axis (MERNAGH, 1997). All these results are in good agreement for a simple correlation between SHG signals and  $\alpha\text{-GeO}_2$  crystals inside the spherulites. It is already known that quartz-like  $\alpha\text{-GeO}_2$  ( $D_3$  point group) does not exhibit any center of symmetry. Furthermore, this crystalline structure is set as positive uniaxial trigonal crystal, having a space group P3121 or P3221, showing low symmetry (MICOULAUT, 2006; KAWAMURA, 2014).

For the sample GC-800C-18h, moreover the incident polarizations VV and VH, it was also performed a 90° counterclockwise sample rotation for the same sample area and finally, then, compared the obtained Raman mappings, as shown in Table 8. Even though VV and VH polarizations on flat surfaces, generally, do not have sensitive differences between them, on VH the returning signal from the sample to the detector is smaller since it is polarized horizontally. Therefore, along with a small signal intensity, this setting could give information about scatterings and also unmask possible bands, whereas the sample turning could give information about crystal orientations and symmetry. Overall, micro-Raman analysis is not showing clear changes comparing different incident linear polarization, but rather weaker signals for intensity as shown in Table 8 for GC-800C-18h. Furthermore, the profile mappings for VV-0 with VH-0 and VV-90 with VH90 for all GC-800C-18h Raman bands are matching. For this sample, only the peaks at around 120, 165 and 440  $\text{cm}^{-1}$  exhibit Raman-active crystalline distribution. Finally, turning the sample 90° leads to an arrangement change which shows no perfect match for VV-0 with VV-90 at the bands at 120 and 165  $\text{cm}^{-1}$  but rather indicates mapping mirroring. However, the same is not seem between VH-0 with VH-90. On the other hand, the modes at 440  $\text{cm}^{-1}$  seems to have similar profile with the turnings. This behavior could indicate that with sample rotating, the incident polarization may face different coordination axes on the trigonal  $\text{GeO}_2$ .

Likewise, for Raman mappings, micro SHG analyses showed similar results including the non-matching for VV-0° and VV-90° rotation. Although the mapping profiles VV-0 with VH-0 and VV-90 with VH-90 are matching, those with VH polarization gives weaker intense peaks bands which is expected once less signal due the cross polarization achieves the detector in this set. Furthermore, it is showing that SHG signals are only seen inside of the spherulites and they are matching with their corresponding Raman modes at 120, 165 and 440  $\text{cm}^{-1}$ . As for the GC-800C-72h (TABLE 9), similar results are seen as well. However, here, it is possible to see even more intense bands (TABLE 9, FIGURE 35) and in its spectrum the presence of the bands at 250 and 880  $\text{cm}^{-1}$ , which contributes for the appearance of different mapping profiles. Furthermore, the signal at 440  $\text{cm}^{-1}$  indicates summing of the bands 120, 165, 250 and 880  $\text{cm}^{-1}$ , and because of it, it may be the reason it is more intense and visible in the mappings. Finally, it is showing one more time that the SHG signal are restricted to regions inside of the spherulite, however, here, they only

match with the modes at 120 and 165  $\text{cm}^{-1}$  and partially at 440  $\text{cm}^{-1}$  and therefore the modes 250 and 850  $\text{cm}^{-1}$  do not contribute for SHG signals.

Finally, correlating key information highlighted in Tables 8 and 9, one could notice that that SHG signals are only generated from the spherulites while the surrounding areas are not SHG active as suspected earlier by the appearance of macro-SHG signals only after heat-treatment for at least 18h (TABLE 6). From Tables 8, 9 and Figure 35, one can also state that the SHG is nor clearly correlated with the incident-SHG polarization neither with sample rotation as should be expected for regularly oriented ONL crystals.

#### 4.2.7 Macroscopic SHG measurements

GNa3 macroscopic SHG investigations (FIGURE 36 and 37) were performed in two different settings. The first one includes Maker fringe measurements (VIGOUROUX, 2011; RODRIGUEZ, 2002; RODRIGUEZ, 2008), also called  $\theta$ -scans, having a linear incident SHG polarization (S or P) fixed and then the SHG intensity is recorded as a function of the incident angle on the sample (FIGURE 36a1, b1). The second performed measurement is known as  $\Psi$ -scans, in which the sample position is fixed and the SHG intensity is collected as a function of the incident polarization (linear, elliptical or circular) under fixed SHG polarization (S or P) detection (FIGURES 36a2, b2 and 37). These macro-SHG experiments were performed with a laser source at 1550 nm (10 ns OPO intracavity) at a repetition rate of 30 Hz. The sample SHG response was recorded in transmission mode with an unfocused (collimated) beam with a diameter of 3140  $\mu\text{m}$  which gives a large probed area compared to the spherulites size.

SHG profiles in Figure 35 are showing similar shapes with higher SHG intensities for longer heat-treatment times i.e. well-formed spherulites.  $\theta$ -scans in Figure 35a1, 8b1 are consistent with transmittance spectra as a function of sample rotation with a maximum SHG intensity around the orthogonal incident angle. Maker fringes measurements also identified higher SHG intensity of about 25% in both samples for parallel incident-harmonic polarizations PP and SS when compared to cross-polarizations PS and SP (representative PP and PS patterns in Figure 36a1, b1).

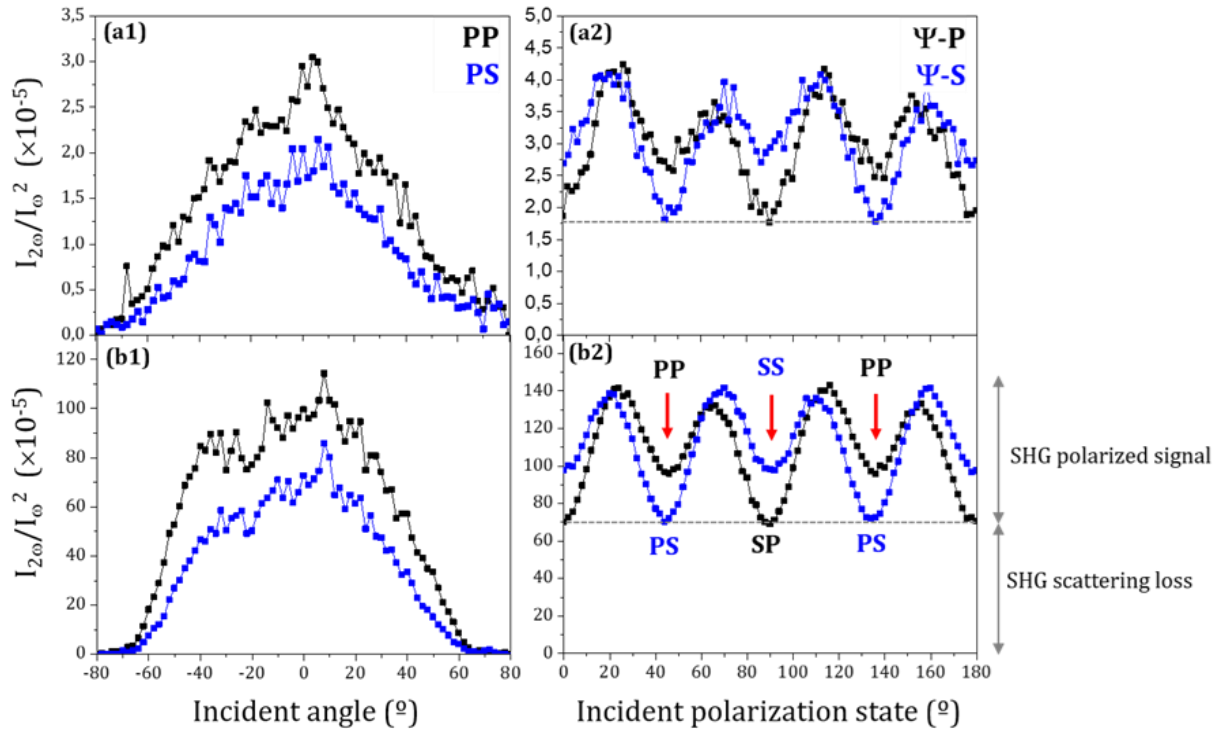


Figure 36 – SHG macro analyses for linear ( $\Theta$ -scan) and nonlinear ( $\Psi$ -scan) polarization for the samples (a) GC-800C-18h and (b) GC-800C-72h.

Reference: Author.

This dependency of the SHG signal with polarizations is a strong indication that the forward SH is not completely governed by Mie scattering from crystallites but also due to the transmitted harmonic signal. In fact, as better seen for polarization patterns ( $\Psi$ -scans) in figure 36a2 and 36b2, both samples exhibit a constant SHG background of about 50% of the total signal attributed to scattering loss, whereas the remaining signal is typical of polarized SHG responses. The intensity difference between  $\theta$ -scan patterns PP-SS and PS-SP also points out some preferential orientation of the crystallites inside the spherulites. In addition, polarization  $\Psi$ -scans exhibit identical SHG patterns under a  $45^\circ$  shift for linear S and P detections, suggesting an in-plane isotropic behavior for both samples along the glass-ceramic surface. In this case, maximum SHG signal is obtained for incident polarizations close to the circular configuration ( $22.5^\circ$  for our setup framework), even if a more detailed analysis gives this maximum in left-elliptical polarization ( $20^\circ$ ) for vertically S-polarized harmonic and right-elliptical polarization ( $24^\circ$ ) for the horizontally P-polarized one. On the other hand, minima SHG intensities are identified for linear

incident polarizations. In these polarization conditions, two distinct cases are also identified as better seen in Figure 36b2: parallel incident-harmonic polarizations (PP and SS) give rise to a medium SHG signal of about a half of the maximum intensity whereas cross-polarizations (PS and SP) do not produce any coherent polarized signal beyond the scattering loss background.

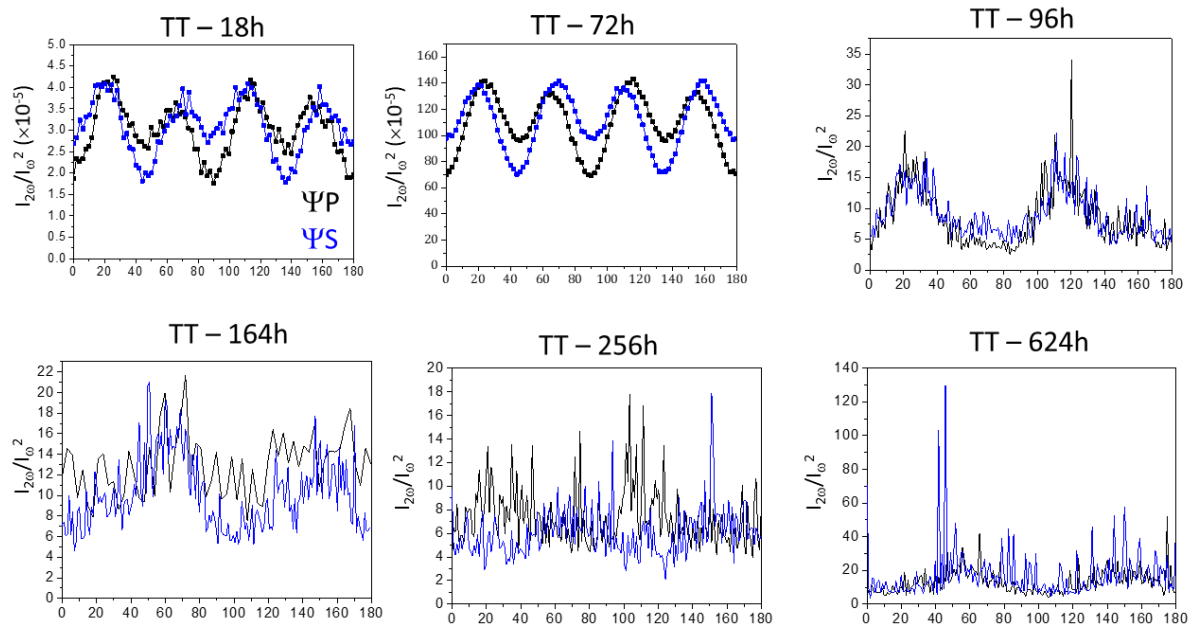


Figure 37 – SHG macro analyses for linear ( $\Theta$ -scan) and nonlinear ( $\psi$ -scan) polarization for the samples GC-800C-18h to 614h.

Reference: Author.

These data are still under complete analysis since the dependency of the incident polarization on the SHG intensity can be related with crystallite organization inside the spherulites as well as with the anisotropy along different crystallographic axes. However, these macro-SHG results point out the potential of these glass-ceramics as second order nonlinear media.

### 4.3 POTASSIUM AND RUBIDIUM TANTALUM GERMANATE GLASS CERAMICS

#### 4.3.1 General features

Finally, after all GCNa glass ceramics analyzes and discussions, it seems important to investigate the effect of alkaline substitution on the spherulite formation and related SHG signals. In fact, spherulite formation was not detected in potassium tantalum germanate glasses in previous works performed in the research group.

For XRD analysis, alkaline tantalum crystalline phases were synthesized in suitable molar proportions as an attempt to obtain isostructures of  $\text{Na}_2\text{Ta}_8\text{O}_{21}$  with substitution of sodium by potassium or rubidium. All of these compounds were prepared using the same conditions and parameters described earlier for  $\text{Na}_2\text{Ta}_8\text{O}_{21}$ . After weighting the respective precursor compounds  $\text{M}_2\text{CO}_3$  ( $\text{M}=\text{Na}, \text{K}, \text{Rb}$ ) and  $\text{Ta}_2\text{O}_5$ , the powder mixture was heated at 800 °C for 8h to eliminate any organic and water components. After that, they were pressed and then, submitted to higher temperature of 1200 °C for 2 h. Finally, their crystalline phases were characterized by XRD as shown in Figure 38.

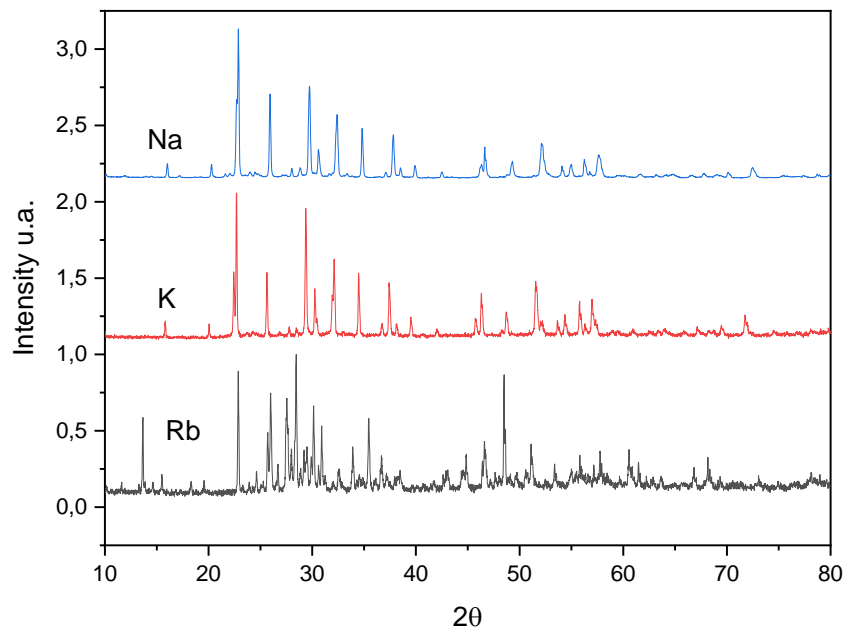


Figure 38 – Diffractograms for the pellets PNa, PK, PRb showing the phases  $\text{Na}_2\text{Ta}_8\text{O}_{21}$ ,  $\text{K}_2\text{Ta}_8\text{O}_{21}$  and  $\text{Rb}_2\text{Ta}_8\text{O}_{21}$ , respectively.

Reference: Author.

One can notice that the sodium and potassium-based compounds (PNa and PK) present similar X-ray patterns between them with a really good peak matching, while for rubidium-based compound exhibits a few extra peaks not matching with the other compounds. From this general analysis, it appears that a  $K_2Ta_8O_{21}$  crystalline phase which is isostructural to  $Na_2Ta_8O_{21}$  was obtained and it must be highlighted that such phase is not reported in the literature or XRD database. The crystalline phase related with Rb-based compound could not be identified using the JCPDS database.

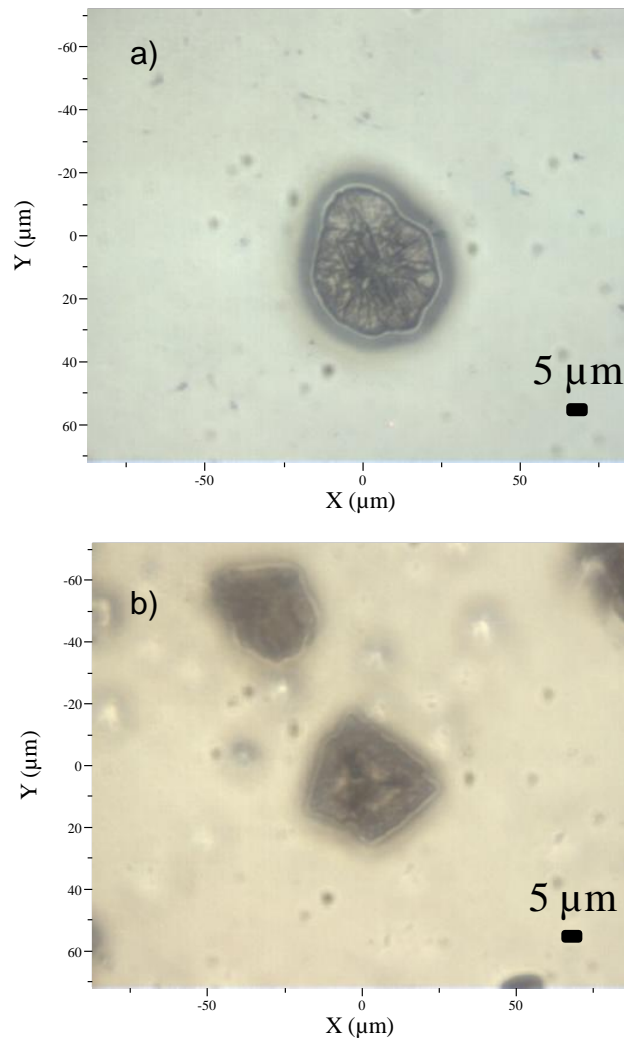


Figure 39 – Micrograph images from macro crystalline structures in different shapes a) spherulite and b) quadratics for the GCRb-800T-72h glass ceramic.

Reference: Author.



After heat treatment using the same parameters as for the obtention of GCNa3-800C-72h (800 °C for 72 h), only GCRb-800T-72h exhibited the presence of organized microstructures such as spherulites, shown in Figure 39a. However, for this glass ceramic, other non-spherical structures with different shapes were also observed as detailed in Figure 39b. Since both GNa and GK glasses promote the crystallization of similar  $M_2Ta_8O_{21}$  perovskite phases but the GCK glass-ceramic does not present surface spherulites, it appears that spherulites formation and correlated  $\alpha$ -GeO<sub>2</sub> formation inside the spherulites could not be directly related with the presence of these alkaline tantalate perovskite phases.

#### 4.3.2 Macroscopic SHG response

Macro-SHG measurements were performed on both GCK and GCRb glass ceramics. However, only GCRb exhibited SHG signals as shown in Figures 40 and 41. Micro-SHG investigations performed on a spherulite in the sample GCRb-800C-24 h allowed to determine that the SHG signal is once again produced inside the spherulites as shown in Figure 40.

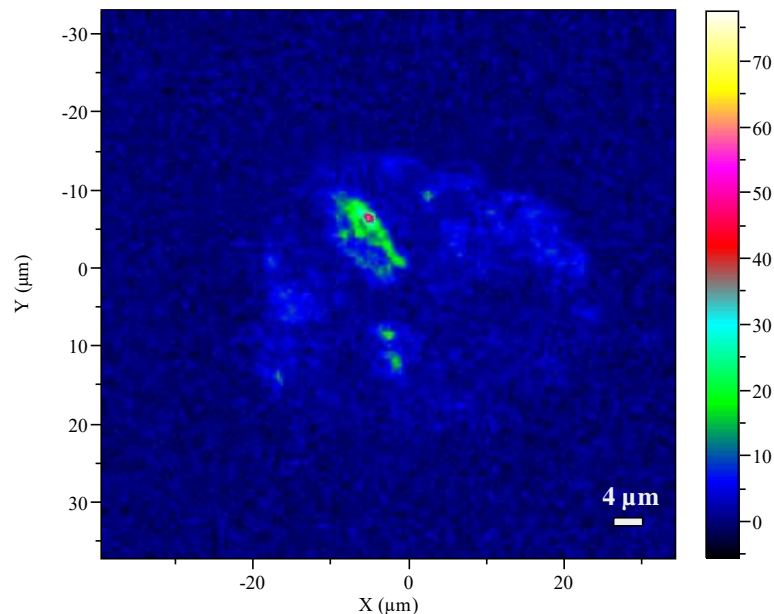


Figure 40 – Micro-SHG mapping for GCRb800C-72h.

Reference: Author.

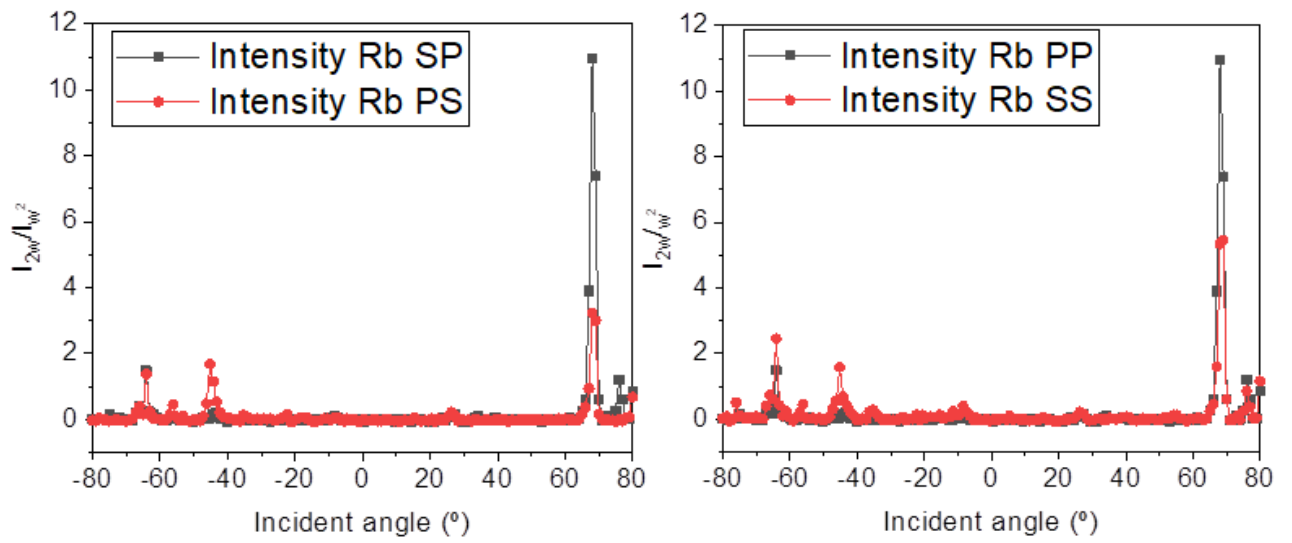


Figure 41 – GCRb-800C-72h SHG signals from  $\Theta$ -scan.

Reference: Author

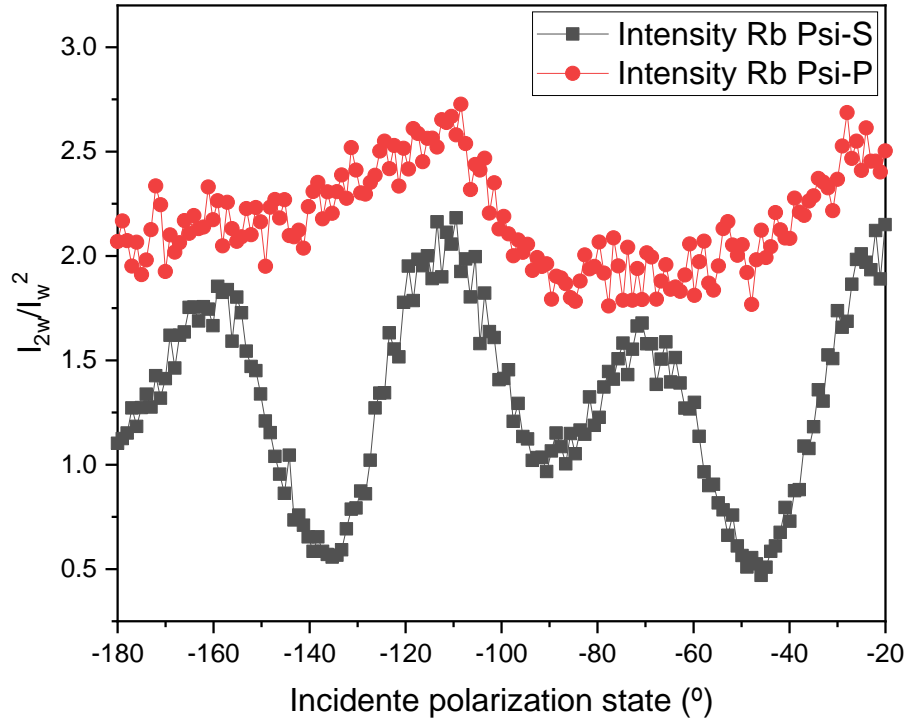


Figure 42 – GCRb-800C-72h SHG signals from  $\psi$ -scan

Reference: Author

For macro-SHG analysis, the glass ceramic GCRb-88C-72h showed an unusual profile of SHG intensity on linear polarization as presented in Figure 41. From a general point of view, the SHG intensity is not clearly correlated with the incident angle but rather due to an average scattering of the SHG signals inside the sample volume. Psi-scan in Figure 42 suggest once again a strong dependency of the SHG intensity with the incident polarization. The origin of the SHG signal is suggested to be due to  $\alpha$ -GeO<sub>2</sub> but future correlated Raman and SHG microscopies are needed in these sample to support this hypothesis.

## CONCLUSION

This work was devoted to a detailed study of the crystallization mechanisms in glasses of composition  $70\text{GeO}_2-10\text{Na}_2\text{O}-20\text{Ta}_2\text{O}_5$  and their related second order nonlinear properties. Under heat treatments at  $800\text{ }^\circ\text{C}$ , a perovskite sodium tantalate phase  $\text{Na}_2\text{Ta}_8\text{O}_{21}$  is precipitated within the first hour whereas longer heat treatments for at least 18 h result in the formation of surface spherical structures called spherulites. Glass ceramics presented higher density and lower refractive index, comparing to the glass, as a result of glass crystallization. Structurally, spherulites are less dense than the glass ceramic surroundings and present higher amount of Ta and O as well as lower Ge content. However, quartz-like  $\alpha\text{-GeO}_2$  was identified by  $\mu\text{-Raman}$  only inside the spherulites and seems to be at the origin of SHG signals also emitted only from these surface structures. In fact, although XRD data mainly identified the presence of  $\text{Na}_2\text{Ta}_8\text{O}_{21}$ , Raman microscopy detected active modes corresponding to the quartz  $\alpha\text{-GeO}_2$  which is an uniaxial trigonal crystalline structure with second order nonlinear properties. It is also suggested that a phase separation is promoted, mainly between Ta and Ge species, giving rise to the spherulite formation. Maximum SHG responses are coming from incident elliptical polarizations and according to macro and micro SHG analysis these signals are depending on the incident polarization. Therefore, those glass ceramic materials show a non-isotropic material response related to the symmetry of the point group  $D_3$  given by  $\text{GeO}_2$ . Finally, preliminary results demonstrated rubidium tantalum germanate glass-ceramics of the same composition are also SHG-active and the origin of this signal is once again associated with surface micrometric structures of different shapes.

## REFERENCES

- ABEYSINGHE, D. C.; et al. A novel MEMS pressure sensor fabricated on an optical fiber. **IEEE Photonics Technology Letters**, v. 13, n. 9, p. 993-995, 2001.
- ABEYSINGHE, D. C.; et al. Novel MEMS pressure and temperature sensors fabricated on optical fibers. **J. Micromech Microengineering**, v. 12, n. 3, p. 229-235, 2002.
- AKERMAN, M. **Natureza, estrutura e propriedades do vidro**, Centro Técnico de Elaboração do Vidro, São Paulo, p. 5-36, 2000.
- ALDERMAN, O.; et al. The germanate anomaly in alkaline earth germanate glasses. **The Journal of Physical Chemistry**, v. 121., p. 9462-9479, 2019.
- ALVES, L.O.; et al. **Vidros**. Cadernos temáticos, química nova na escola, edição especial, 2001.
- ANANTHANARAYANAN, A.; GOSWAMI, M.; KOTHIYAL, G. P. Glasses and glass-ceramics for vacuum and high-temperature applications. **Materials Under Extreme Conditions**, p. 195-233, 2017.
- ANANTHANARAYANAN, A; et al. Some properties of lithium aluminium silicate (LAS) glass-ceramics used in glass-ceramic to metal compressive seal for vacuum applications, **J. Phys. Conf. Ser.**, v. 114, 2008.
- AQUINO, F. T. **Desenvolvimento de materiais nanoestruturados à base de óxido de nióbio para aplicação em fotônica**. 2013. 208f. Tese (Doutorado em Química) - Faculdade de Filosofia, Ciências e Letras de Ribeirão Preto, Universidade de São Paulo, Ribeirão Preto, 2013
- ARAÚJO, E. B. Vidro: uma breve história, técnicas de caracterização e aplicações na tecnologia. **Revista Brasileira de Ensino de Física**, v. 19, n. 3, 1997.
- ARMSTRONG, J. A.; et al. Interactions between light waves in a nonlinear dielectric. **J. Physical Review**, v. 127 n. 6, p. 1918-1939, 1962.
- ATUCHIN, V. V.; et al. Low-temperature chemical synthesis and microstructure analysis of GeO<sub>2</sub> crystals with  $\alpha$ -quartz structure. **Cryst. Growth Design**, v. 9, n. 4, p. 1829-1832, 2009.
- BERTRAND, A.; et al. New transparent glass-ceramics based on the crystallization of "anti-glass" spherulites in the Bi<sub>2</sub>O<sub>3</sub>-Nb<sub>2</sub>O<sub>5</sub>-TeO<sub>2</sub> system. **Cryst. Growth Design**, v. 15, n. 10, p. 5086-5096, 2015.
- BOETTI, Nadia, et al. Highly doped phosphate glass fibers for compact lasers and amplifiers: a review. **Applied Sciences**, v. 7, n. 12, p. 1295-1313, 2017.

BOGOMOLOVA, L. D.; PAVLUSHKINA, T. K.; MOROZOVA, I. V. Formation of glass synthesized by sol-gel technology. **Glass and Ceramics**, v. 63, n. 7, p. 254-258, 2006.

BOYD, R. W. **Nonlinear optics - the nonlinear optical susceptibility**. 3. ed. New York: Academic Press, 2008, p. 1-67, 2008.

BRAZ, C.E. **Preparação e caracterização de vidros e vitrocerâmicas fluorofosfatos no sistema ternário  $\text{NaPO}_3\text{-WO}_3\text{-PbF}_2$** . 2014. 89f. Dissertação (Mestrado em Ciência dos Materiais) – UNIFAL, Poços de Caldas, 2014.

CALLISTER, W. D.; RETHWISCH, D. G., **Fundamentals of materials science and engineering**. 5. ed. USA: John Wiley & Sons, 2001.

CARPENTER, P.R.; CAMPBELL, M.; RAWLINGS, R.D. Spherulitic growth of apatite in a glass ceramic system. **J. Mat. Sci. Lett**, v. 5, n. 12, p. 1309-1312, 1986.

CARTER, C. B.; NORTON, M. G. **Ceramic Materials**. 1 ed. New York: Springer-Verlag New York, 2007.

CASASOLA, R.; RINCON, J.; ROMERO, M. Glass-ceramic glazes for ceramic tiles: a review. **J. Mater. Sci**, v. 47, p. 553-582, 2012.

CHAMINADE, J.P.; POUCHARD, M.; HAGENMULLER, P. Tantalates and oxyfluorotantalates of sodium. **Rev. Chem. Min**, v. 9, p. 381-402, 1972.

CHIASERA, A.; et al.  $\text{CO}_2$  laser irradiation of  $\text{GeO}_2$  planar waveguide fabricated by rf-sputtering. **Opt. Mater. Express**, v.3, n. 9, p. 1561-1570, 2013.

CHOWDARI, B. V. R.; RADHAKRISHNAN, K. Ionic conductivity of the vitreous  $\text{Li}_2\text{O:P}_2\text{O}_5\text{:Ta}_2\text{O}_5$  system. **Journal of Non-Crystalline Solids**, v. 108, p. 323-332, 1989.

CORBELLA, C. et al. Influence of the porosity of RF sputtered  $\text{Ta}_2\text{O}_5$  thin films on their optical properties for electrochromic applications. **Solid State Ionics**, v. 165, p. 15-22, 2003.

CUNHA, C. R. **Vidros e vitrocerâmicas luminescentes de germanato de tântalo**. 2018. 141f. Tese (Doutorado em Química Inorgânica) - UNIFAL, Alfenas, 2018.

CUNHA, C. R.; et al. Alkali metal tantalum germanate glasses and glass-ceramics formation. **Journal of Non-Crystalline Solids**, v. 499, p. 401-407, 2018.

DEUBENER, J.; et al. Updated definition of glass-ceramics. **Journal of Non-Crystalline Solids**, v. 501, p. 3-10, 2018.

DEUBENER, J. H.; et al. Viscosity, relaxation and elastic properties of photo-thermo-refractive glass. **Journal of Non-Crystalline Solids**, v. 355, p. 126-131, 2009.

DOREMUS R.H. **Glass Science**. 2 ed. New York: Wiley-Interscience, 1973.

CORNING. Glassmaking: one of the world's oldest products faces the digital future. **The Economist**, New York, 12 Oct. 2017. Available in: <https://www.economist.com/science-and-technology/2017/10/12/one-of-the-worlds-oldest-products-faces-the-digital-future>. Access: 21 May. 2019.

EVSTROPIEV, K.S.; IVANOV, A.O. **Advances in glass technology**. New York: Plenum, 1963. v. 2.

FOKIN, V.M.; et al. Homogeneous crystal nucleation in silicate glasses : A 40 years perspective. **Journal of Non-Crystalline Solids**, v. 352, n. 26-27, p. 2681-2714, 2006.

FRANKEN, P. A. A. E. ; Hill, PETERS C. W.; WEINREICH, G. Generation of optical harmonics. **Phys. Rev. Lett.**, v. 7, p. 118-119, 1961.

FREIMAN, S.W.; ONODA, G.Y.; PINCUS, A.G. Spherulitic crystallization in glasses. **Am. Cer. Soc. Bull.** v.50, n. 4, p. 91-112, 1971.

GIELIS, J. J. H.; et al. Optical second-harmonic generation in thin film systems. **Journal of Vacuum Science & Technology**, v. 26, n. 6, p. 1519–1537, 2008.

GIRI, P. K.; et al. Ultraviolet and blue photoluminescence from sputter deposited Ge nanocrystals embedded in SiO<sub>2</sub> matrix. **Journal of Applied Physics**, v. 103, n. 10, p. 103534-103544, 2008.

GIRI, P. K.; DHARA, S. Freestanding core-shell nanocrystals with varying sizes and shell thicknesses: microstructure and photoluminescence studies. **Journal of Nanomaterials**, v. 2012, p. 1-5, 2012.

GOOCH J. W. Cauchy's dispersion formula. **Encyclopedic Dictionary of Polymers**, New York: Springer, 2007.

GUEDES, L.; et al. Effect of alkaline modifiers on the structural, optical and crystallization properties of niobium germanate glasses and glass-ceramics. **Optical Materials**. v. 105, p. 109866-109874, 2020.

GUENTHER, B. D. **Modern Optics**. 2 ed. Oxford: Oxford University Press, 2015. p 664-711.

HARRIS, D. C. **Análise química quantitativa**. 8 ed. São Paulo: LTC, 2012.

HE, M.; et al. Glass-ceramic phosphors for solid state lighting: a review. **Ceramics International**, v. 46, n. 13, p 20623-20632, 2020.

HENDERSON, G. S.; FLEET, M. E. The structure of glasses along the Na<sub>2</sub>O-GeO<sub>2</sub> join. **J. Non-Cryst. Solids**, v. 134, p. 259-269, 1991.

HENDERSON, G. S.; SOLTAY, L. G.; WANG, H. M., Q speciation in alkali germanate glasses. **Journal of Non-Crystalline Solids**, v. 356, p. 2480-2485, 2010.

HOFSTETTER, W.; et al. Determination of the onset of crystallization of amorphous materials using different methods. **Materials Science and Engineering**, v. 228, p. 213-217, 1997.

HOLAND, W. **Glass-ceramic technology**. 2 ed. Hoboken: John Wiley & Sons, 2012. p. 1-4

HONGISTO, M.; et al. **Radiation-Induced defects and effects in germanate and tellurite glasses**. **Materials**, v. 13, n. 17, p. 3846-3867, 2020.

HUANG, L.; et al. Design of thermally poled twin-core fiber coupler with electrical tunability. **IEEE Photonics Technol**, v. 27, p. 919-922, 2015.

HUANG, P.Y., et al. Direct imaging of a two-dimensional silica glass on graphene. **Nano Lett.** V. 12, p. 1081-1086, 2012.

JIANG, B.; et al. High-efficiency second-order nonlinear processes in an optical microfiber assisted by few-layer GaSe. **Light Sci Appl**, v 9, n. 63. p. 1-8, 2020.

JIANG, X.; et al. Fluorogermanate glass with reduced content of OH-groups for infrared fiber optics. **J. Non-Cryst. Solids**, v. 355, p. 37-42, 2009.

JIANG, Z.; ZHANG, Q. The structure of glass: a phase equilibrium diagram approach, **Progress in Materials Science**, v. 61, p. 144-215, 2014.

JIUSTI, J.; et al. **Effect of network formers and modifiers on the crystallization resistance of oxide glasses**. *Journal of Non-Crystalline Solids*, v. 550, p. 20359-20370, 2020.

JUSTINO, C. **Vidros fosfatos de metais de transição**. 2014. 110f. Dissertação (Mestrado em Engenharia dos Materiais) - UNIFAL, Poços de Caldas, 2014.

JOSEPH, C.; BOURSON, P.; FONTANA, M. D., Amorphous to crystalline transformation in Ta<sub>2</sub>O<sub>5</sub> studied by Raman spectroscopy. **J. Raman Spectrosc**, v. 43, p. 1146–1150, 2012.

KARAMANOV, A.; PELINO, M. Evaluation of the degree of crystallization in glass-ceramics by density measurements. **Journal of the European Ceramic Society**, v. 19, n. 5, p. 649–654, 1990.

KARASAWA, T.; TAKETOMI, Y. Growth and structure of spherulites in polymer-dispersed liquid crystals fabricated by photopolymerization-induced phase separation. **Japanese Journal of Applied Physics**, v. 37, n. 8, p. 4448–4453, 1998.

KARPUKHINA, N.; HILL, R. G.; LAW, R. V. Crystallisation in oxide glasses – a tutorial review. **Chem. Soc. Rev.**, v. 43, n. 7, p. 2174-2186, 2014.



- KATO, N. Optical second harmonic generation microscopy: application to the sensitive detection of cell membrane damage. **Biophysical Reviews**, v. 11, n. 3, p. 399-408, 2019.
- KAWAMURA, I.; et al. Polarization-sensitive second harmonic generation microscopy of  $\alpha$ -quartz like  $\text{GeO}_2$  ( $\alpha\text{-GeO}_2$ ) polycrystal. **Journal of Physics D: Applied Physics**, v. 47, n. 45, p. 455305-455313, 2014.
- KOMATSU, T. Design and control of crystallization in oxide glasses. **Journal of Non-Crystalline Solids**, v. 428, p. 156-175, 2015.
- KOROLEVA, O. N.; et al. Vibrational spectroscopy and density of  $\text{K}_2\text{O-B}_2\text{O}_3\text{-GeO}_2$  glasses with variable B/Ge ratio. **Phys. Chem. Chem. Phys**, v. 21, p.12676–12684, 2019.
- KOTHIYAL G. P.; et al. **Functional Materials**. London: Elsevier, 2012, p. 323-386.
- LEPICARD, P. A. **Design of surface chemical reactivity and optical properties in glasses**. 2016. 288s. Thesis (doctorate in Physical chemistry of condensed matter) - L'université de Bordeaux, Bordeaux, 2016. p. 8-37.
- LEPICARD, A.; et al. Demonstration of dimensional control and stabilization of second harmonic electro-optical response in chalcogenide glasses. **Optical Materials Express**, v. 8, n. 6, p. 1613-1625, 2018.
- LEWIS, M. H., **Glasses and glass-ceramics**. New York: Chapman and Hall xii, 1989.
- LI, M. J.; HAYASHI, T. Advances in low-loss, large-area, and multicore fibers. **Optical Fiber Telecommunications**, v. 7, p. 3-50, 2020.
- LIMA, C. et al. Thermal, structural and crystallization study of niobium potassium phosphate glasses. **Mat. Res.**, v. 18, n. 2, p. 13-16, 2015.
- LIN, A.; et al.  $\text{Cu}^{2+}$ -doped germano-silicate glass fiber with high resonant nonlinearity. **Opt. Express**, v. 15, n. 7, p. 3665-3672, 2007.
- LIN, A.; RYASNYANSKIY, A.; TOULOUSE, J. Fabrication and characterization of a water-free mid-infrared fluorotellurite glass. **Opt. Lett.**, v. 36, n. 5, p. 740–742, 2011.
- LIN, L.; XIONG, K.; ROBERTSON, J. Atomic structure, electronic structure, and band offsets at  $\text{Ge:GeO:GeO}_2$  interfaces. **Applied Physics Letters**, v. 97, n. 24, p. 242902-242904, 2010.
- LIU, X.; ZHANG, M. Theoretical study for thermal/electric field poling of fused silica. **Jap. J. Appl. Phys.**, v. 40, p. 4069-4076, 2001.
- LOIKO, P. A.; et al. Crystallization and nonlinear optical properties of transparent glass-ceramics with  $\text{Co:Mg(Al,Ga)}_2\text{O}_4$  nanocrystals for saturable absorbers of lasers at 1.6-1.7  $\mu\text{m}$ . **J. Phys. Chem. Sol.**, v. 103, p. 132-141, 2017.

LUCAS, J.; et al. **Rare Earth: science, technology, production and use**. Elsevier, 2015. p. 319-332.

MADON, M.; et al. A vibrational study of phase transitions among the GeO<sub>2</sub> polymorph. **Physics and Chemistry of Minerals**, v. 18, p. 7-18, 1991.

MANZANI, D. **Vidros óxidos contendo átomos pesados para aplicações em óptica não linear e fotônica na região do infravermelho**. 2011. 227f. Tese (Doutorado em Química Inorgânica) - Unesp, Araraquara, 2011.

MARCH, A.; SUNY, S. **Frequency Doubling Using LBO in a Resonant External Enhancement Cavity**, 2001. Available in:  
< <https://laser.physics.sunysb.edu/~amarch/reports/SHG/cavity.html>>. Access in: 16 dec. 2020

MARCONDES, L.; et al. High niobium oxide content in germanate glasses: thermal, structural, and optical properties. **Journal of the American Ceramic Society**, v. 101, p. 220–230, 2018.

MARCONDES, L.; et al. Transparent glass and glass-ceramic in the binary system NaPO<sub>3</sub>-Ta<sub>2</sub>O<sub>5</sub>. **Journal of the American Ceramic Society**, v. 103, n. 3, p. 1647-1655, 2019.

MARGULIS, W.; TARASENKO, O.; MYRÉN, N. Who needs a cathode? creating a second-order nonlinearity by charging glass fiber with two anodes. **Optics Express**, v. 17, p. 15534-15540, 2009.

MCMILLAN, P.W., **Glass-ceramics**. New York: Academic Press viii, 1964.

MERNAGH, T. P.; LIU, L. G. Temperature dependence of Raman spectra of the quartz- and rutile-types of GeO<sub>2</sub>. **Phys. Chem. Miner**, v. 24, n.1, p. 7-16, 1997.

MICOULAUT, M.; CORMIER, L.; HENDERSON, G. The structure of amorphous, crystalline and liquid GeO<sub>2</sub>. **Journal of Physics Condensed Matter**, v. 18, p. 53-84, 2006.

MOATTAR F. Ingenuities and innovations of Rhazes in alchemy. **Journal of Islamic and Iranian Traditional Medicine**, v. 1, n. 1; p. 33-38, 2010.

MONTEIRO, G.; et al. Optical and spectroscopic properties of germanotellurite glasses. **Journal of Non-Crystalline Solids**, v. 357, p. 2695–2701, 2011.

MURTHY, M.K.; IP, J. Some physical properties of alkali germanate glasses. **Nature**, v. 201, p. 285-286, 1964.

MURUGASEN, P.; SURESH, S.; SHAJAN, D. Preparation, techniques and tools used for investigating glasses: an overview. **International Journal of Chemical Sciences**, v. 13, p. 693-713, 2015

MUSGRAVES, J. D.; HU, J.; CALVEZ, L. **Springer Handbook of Glass**. 1 ed. Springer International Publishing, 2019. p. 194-219.

NAGANO, N.; SAITO, M.; MIYAGI, M. Refractive-indexes of SiO<sub>2</sub>-based and GeO<sub>2</sub>-based glasses near the infrared-absorption peaks. **Journal of Non-Crystalline Solids**, v. 135, p. 114-121, 1991.

NEWMAN, W. What have we learned from the recent historiography of alchemy?. **Isis**, v. 102, n. 2, p. 313-321, 2011.

NIKOLENKO, V.; NEMET, B.; YUSTE, R. A two-photon and second-harmonic microscope. **Methods**, v. 30, p. 3-15, 2003.

PANTAZIS, P.; et al. Second harmonic generating (SHG) nanoprobe for in vivo imaging. **Proceedings of the National Academy of Sciences**, v. 107, n. 33, p. 14535-14540, 2010.

PIETRO, G. M.; et al. Thermal, structural, and crystallization properties of new tantalum alkali-germanate glasses. **Journal of the American Ceramic Society**, v. 98, n. 7, p. 2086-2093, 2015.

POIRIER, G.; et al. Second harmonic generation in sodium tantalum germanate glasses by thermal poling. **Journal Physic Chemistry**, v. 123, n. 43, p. 26528-26535, 2019.

POLUKHIN, V. N.; BURDINA, V. A. **Optical glass**. V. N. Polukhin, V. A. Byrdina, and N. A. Filippov, USSR Inventor's Certificate No. 583104. Byull Izobret, No. 45, 1977.

POLUKHIN, V. N.; MODESTOV, O. V. **Inorganic Materials**. v. 10, p. 757, 1974.

POLUKHIN, V. N.; URUSOVSKAYA, L. N.; Galant, V. E. **An optical glass**. V. N. Polukhin, L. N. Urusovskaya and V. E. Galant, USSR Inventor's Certificate No. 545599. Byull Izobret, No. 5, 1977.

PRAMOD, R. W.; SEONGMIN, J.; WON, T. H. Optical properties of Ho-doped alumino-germano-silica glass optical fiber. **Journal of Non-Crystalline Solids**, v. 354, n. 14, p.1453-1459, 2008.

PRUNERI, V.; et al. Greater than 20%-efficient frequency doubling of 1532-nm nanosecond pulses in quasi-phase-matched germanosilicate. **Optical Fibers**, v. 24, p. 208-210, 1999.

RAIMO, M. Growth of spherulites: foundation of the DSC analysis of solidification. **ChemTexts**, v. 1, n. 13, p. 1-21, 2015.

RAJARAMAKRISHNA, R.; KAEWKHAO, J. Glass material and their advanced applications. **KnE Social Sciences**, v. 3, n.18, p. 796–807, 2019.

RAWLINGS, R.D.; WU, J.P.; BOCCACCINI, A.R. Glass-ceramics: their production from wastes, a review. **J. Mater. Sci**, v. 41, p. 733-761, 2006.

RODRIGUEZ V.; SOURISSEAU, C. General maker-fringe ellipsometric analyses in multilayer nonlinear and linear anisotropic optical media. **J. Opt. Soc. Am. B**, v. 19, n. 11, p. 2650-2664, 2002.

RODRIGUEZ, V. Quantitative determination of linear and second-harmonic generation optical effective responses of achiral or chiral materials in planar structures: Theory and materials. **The Journal of Chemical Physics**, v. 128, n.6, p. 064707(1)-064707(10), 2008.

RONG, Q. J. et al. Infrared and Raman spectra of binary tellurite glasses containing boron and indium oxides, **Journal of Materials Science**, v. 27, n. 14, p. 3793-3798, 1992.

ROSS, J. R. H. **Contemporary Catalysis**. 1 ed. Elsevier, 2019. p. 121–132.

RUIZ, J.C.; et al. Tantalum-based electrocatalysts prepared by a microemulsion method for the oxygen reduction and evolution reactions. **Electrochimica Acta**, v. 317, p. 261-271, 2019.

RUPP, J. L. M.; et al. Time-temperature-transformation (TTT) diagrams for crystallization of metal oxide thin films. **Advanced Functional Materials**, v. 20, n. 17, p. 2807–2814, 2010.

SAKKA S. Sol–gel formation of bulk glasses. In: Klein L., Aparicio M., Jitianu A. (eds) **Handbook of Sol-Gel Science and Technology**. Springer, 2017.

SANDITOV, B. D.; SANGADIEV, S. S.; SANDITOV, D. S. Relaxation time and cooling rate of a liquid in the glass transition range. **Glass Physics and Chemistry**, v. 33, n. 5, p. 445–454, 2007.

SCHNEIDER, T. **Nonlinear Optics in Telecommunications**. 1 ed. Springer-Verlag Berlin Heidelberg, 2014. p. 9-40.

SEBASTIÁN, D.; et al. Facile synthesis of Zr- and Ta-based catalysts for the oxygen reduction reaction. **Chinese Journal of Catalysis**, v. 36, n. 4, p. 484-489, 2015.

SHELBY, J. E. **Introduction to Glass Science and Technology**. 2 ed. New York: The Royal Society of Chemistry, 2005.

SHEVCHENKO, V.Y. From ancient inorganic chemistry and alchemy of ceramics to modern nanotechnology. **Glass Phys Chem**, v. 31, p. 11-26, 2005.

SHRIVER, D. F.; ATKINS, P. W. **Química inorgânica**. 4. ed. Porto Alegre: Bookman, 2008.

SIMMONS, J. H.; POTTER, K. S. **Optical Materials**. 1 ed. Academic Press, 2000.

SIMON, F.; et al. Relevance of the second harmonic generation to characterize crystalline samples. **Chemical Engineering & Technology**, v. 38, n. 6, p. 971–983, 2015.

STAVROULA F.; PANOIU, N. Feature issue introduction: beyond thin films: photonics with ultrathin and atomically thin materials. **Opt. Mater. Express**, v. 9, p. 2427-2436, 2019.

STRNAD, Z. **Glass-ceramic materials**. 2 ed. Amsterdam: Elsevier, 1986.

SUN, S.; ZENG, H. Size-controlled synthesis of magnetite nanoparticles. **Journal of the American Chemical Society**, v. 124, n. 28, p. 8204–8205, 2002.

SUTHERLAND, R. L. **Handbook of nonlinear optics**. 2 ed. CRC Press, 2003.

TAUC, J.; GRIGOROVICI, R.; VANCU, A. Optical properties and electronic structure of amorphous germanium. **Physica Status Solidi (b)**, v. 15, n. 2, p. 627-637, 1966.

THIEME, K.; RUSSEL, C. Nucleation and growth kinetics and phase analysis in zirconia-containing lithium disilicate glass, **J. Mater. Sci.**, v. 50, p. 1488-1499, 2014.

TRAN, R. J.; SLY, K. L.; CONBOY, J. C. Applications of surface second harmonic generation in biological sensing. **Annual Review of Analytical Chemistry**, v. 10, n. 1, p. 387-414, 2017.

TRUKHIN A.; CAPOEN B. Raman and optical reflection spectra of germanate and silicate glasses. **J. NonCryst. Solids**, v. 351, p. 3640-3643, 2005.

TSUTOMU S.; JUN S. L. Lattice dynamics and temperature dependence of the linewidth of the first-order Raman spectra for sintered hexagonal GeO<sub>2</sub> crystalline. **Journal of the Physical Society of Japan**, v. 67, n. 11, p. 3809–3815, 1998.

TUMMALA, R. R. Ceramic and glass-ceramic packaging in the 1990s, **J. Am. Ceram. Soc.**, v. 74, n. 5, p. 895-908, 1991.

VARGA, J. Supermolecular structure of isotactic polypropylene. **J. Mat. Sci.**, v. 27, p. 2557-2579, 1992.

VARSHNEYA A.; MAURO J. C. **Fundamentals of Inorganic Glasses**. 3 ed. Elsevier, 2019.

VIGOUROUX, H.; et al. Crystallization and second harmonic generation of lithium niobium silicate glass ceramics. **Journal of the American Ceramic Society**, v. 94, p. 2080-2086, 2011.

WALKER, J.; HALLIDAY, D., **Fundamentals of physics**. 10 ed. John Wiley & Sons, 2014.

WALLIS, G.; POMERANTZ, D. I. Field assisted glass-metal sealing. **J. Appl. Phys.**, v. 40, p. 3946-3949, 1969.

WANG, Y.; et al. Second harmonic generation spectroscopy on two-dimensional materials. **Opt. Mater. Express**, v. 9, p. 1136-1149, 2019.

- XIE, M.; et al. Reaction of GeO<sub>2</sub> with Ge and crystallization of GeO<sub>2</sub> on Ge. **Journal of Applied Physics**, v. 127, n. 2, p. 024101(1)-024101(7), 2020.
- YANG Y. M.; YANG, L. W.; CHU, P. K. Polarized Raman scattering of Ge nanocrystals embedded in a-SiO<sub>2</sub>. **Journal of Applied Physics**, v. 90, p. 081909(1)-081909(3), 2007.
- YANG, L.; et al. Semiconductor photocatalysts for water oxidation: current status and challenges. **Phys. Chem. Chem. Phys.**, v.16, p. 6810-6826, 2014.
- YOU, J. W.; et al. Nonlinear optical properties and applications of 2D materials: theoretical and experimental aspects. **Nanophotonics**, v. 8, n. 1, p. 63-97, 2019.
- ZACHARIASEN, W. H. The atomic arrangement in glass. **Journal of the American Chemical Society**, v. 54, n. 10, p. 3841–3851, 1932.
- ZANOTO, E. D.; COUTINHO, F.A.B. How many non-crystalline solids can be made from all the elements of the periodic table? **J. Non-crys. Sol.**, v. 347, 285-288, 2004.
- ZANOTTO, E. D.; MAURO, J. C. The glassy state of matter: Its definition and ultimate fate. **Journal of Non-Crystalline Solids**, v. 471, p. 490-495, 2017.
- ZERLIM, A. **Estudo da dissolução de vidros niobofosfato em água e em solução simuladora de fluido fisiológico**. 2008. 91f. Dissertação (Mestrado em Ciência na Área de Tecnologia Nuclear-Materiais) - USP, São Paulo, 2008.
- ZHANG, W. J.; et al. **New insights into the structure and physical properties of sodium and potassium germanate glass via the phase diagram approach**. *J. Non Cryst. Solids*, 475, 108–115, 2017.
- ZHAO, J.; YANG, L., et al. Reduced GeO<sub>2</sub> nanoparticles: electronic structure of a nominal GeO<sub>x</sub> Complex and Its stability under H<sub>2</sub> annealing. **Sci Rep**, v. 5, p. 17779, 2015.